UC San Diego

UC San Diego Electronic Theses and Dissertations

Title
On the distribution of oceanic chlorophyll

Permalink
https://escholarship.org/uc/item/3vt8v9pc

Author
Hodges, Benjamin A.

Publication Date
2006

Peer reviewed|Thesis/dissertation

UNIVERSITY OF CALIFORNIA, SAN DIEGO

On the Distribution of Oceanic Chlorophyll

A dissertation submitted in partial satisfaction of the
requirements for the degree
Doctor of Philosophy

in

Oceanography

by

Benjamin A. Hodges

Committee in charge:

      Professor Daniel L. Rudnick, Chair
      Professor Peter J. S. Franks
      Professor Robert Pinkel
      Professor Sutanu Sarkar
      Professor William R. Young

2006

The dissertation of Benjamin A. Hodges is approved, and it is acceptable in quality and form for publication on microfilm:

_____

_____

_____

_____

_____
Chair

University of California, San Diego

2006

DEDICATION

In memory of my grandfather,

Joseph Lawson Hodges Jr.

TABLE OF CONTENTS

LIST OF FIGURES AND TABLES

ACKNOWLEDGEMENTS

I would like to thank Dan Rudnick for being a great advisor. He was always available, and never failed to drop what he'd been doing to provide advice and encouragement when I went to see him. He was consistently upbeat, both during my productive periods, and during the inevitable lapses in my rate of progress. At the same time he allowed me the space to develop my own ideas and follow my own path through the process of learning to be a scientist.

The other members of my committee—Peter Franks, Bill Young, Rob Pinkel, and Sutanu Sarkar—all taught excellent classes which I was lucky enough to take. Jeff Sherman patiently taught me the ins and outs of the Spray glider, and the rest of the IDG group provided support in glider preparation and operation. Glenn Ierley provided advice on numerical calculations. Thanks are due to the California Cooperative Oceanic Fisheries Investigations program for making the historical data I have used in Chapter 4 freely available.

Joe Martin was my office mate for 4 years, and remains a good friend. His unwavering focus and dogged pursuit of his scientific goals was an inspiration. His willingness, early on, to answer my Matlab questions also came in handy. Other friends among the SIO student body who made my graduate school experience a memorable one were Eric Giddens, Dave Drazen, Steve Grimes, and Ana Sirovic.

For the last 28 years (or at least the 25 that I can remember) my family has been my ultimate source of support and stability. I got my start in science from my mom, who taught me at home for five of my elementary school years. From my

father I acquired an interest in and an affinity for things mechanical, which have served me well in the lab and at sea.

2000	B.A., Physics, University of California at Berkeley
2000-2006	Graduate Student Researcher, Scripps Institution of Oceanography, University of California, San Diego
2006	Ph.D., Oceanography Scripps Institution of Oceanography, University of California, San Diego

PUBLICATIONS

Hodges, B.A. and D.L. Rudnick, Horizontal variability in chlorophyll fluorescence and potential temperature, Deep-Sea Research I, in press, July 2006.

Hodges, B.A. and D.L. Rudnick, Simple models of steady deep maxima in chlorophyll and biomass, Deep-Sea Research I, 51, 999-1015, 2004.

FIELDS OF STUDY

Major Field: Physical Oceanography

Studies in Descriptive Physical Oceanography
Professors M.C. Hendershott, D.H. Roemmich, and L.D. Talley

Studies in Data Analysis
Professors S. Gille, R. Pinkel, and D.L. Rudnick

Studies in Fluid Dyamics and Turbulence
Professors S. Sarkar and C.D. Winant

Studies in Geophysical Fluid Dynamics
Professors P. Cessi and W.R. Young

Studies in Linear and Nonlinear Waves
Professors R.T. Guza, M.C. Hendershott, and W.K. Melville

Studies in Applied Mathematics
Professors G.R. Ierley, S.G. Llewellyn Smith, and R. Salmon

Studies in Biological Oceanography and Biological-Physical Interactions
Professor P.J.S. Franks

Studies in Atmospheric Physics
Professor R.C. Somerville

ABSTRACT OF THE DISSERTATION

On the Distribution of Oceanic Chlorophyll

by

Benjamin A. Hodges

Doctor of Philosophy in Oceanography

University of California San Diego, 2006

Professor Daniel L. Rudnick, Chair

The deep chlorophyll maximum (DCM) is a ubiquitous but poorly understood feature of the ocean ecosystem. Chapter 2 explores possible explanations for the existence of the DCM with simple, one-dimensional, steady-state mathematical models. Sinking of plankton or detritus is shown to be critical in the formation of a deep maximum in phytoplankton biomass. A model with species-dependent chlorophyll-to-biomass ratios and growth rate characteristics demonstrates the formation of a DCM which does not represent a maximum in biomass.

During the Spice cruise of 1997, SeaSoar measurements were made with 4-m horizontal resolution on two isopycnals and two isobars along a 1000-km transect in the northeastern Pacific. Chapter 3 is an investigation, based on these data, of the relationship between the distribution of chlorophyll and that of temperature.

Fluctuations in the two tracers tend to align with each other, either in phase or out of phase, at scales above 10 km. Enhancement of gradients by stirring is shown to be a likely explanation for this behavior, and models suggest that turbulent diffusion or rapid phytoplankton growth could be responsible for destroying alignment at small scales.

Chapter 4 presents results from recent glider measurements along CalCOFI Line 93. Three glider missions were carried out along the 700-km transect, and chlorophyll and salinity measurements are compared with historical CalCOFI data. Sharp, density-compensated salinity fronts are found to be common, often with corresponding features in the chlorophyll field. The deep chlorophyll maximum tends to track vertical fluctuations in the depth of nearby isopycnals, but on average the depth of the DCM does not move as far as that of the isopycnals.

Chapter 1

Introduction

This dissertation examines the distribution of chlorophyll in the ocean, both vertically and horizontally, and from both a modeling and an observational perspective. Chapter 2 is an attempt to understand the vertical structure of the oceanic chlorophyll distribution through a series of simple ecological models. Chapter 3 makes use of hydrographic and chlorophyll data from long horizontal instrument tows in the northern Pacific to investigate the horizontal distribution of chlorophyll and its relationship to water temperature, and develops horizontal stirring models to suggest explanations for the observed behavior. The fourth and final chapter describes the use of an autonomous underwater glider to elucidate physical and biological features of the waters off the coast of southern California by measuring chlorophyll concentration, temperature, and salinity along a 700-km transect.

Phytoplankton are by far the dominant primary producers of the ocean, forming the base of the oceanic food web, and providing the energy which fuels the entire ocean ecosystem. The role they play in uptake of atmospheric carbon

dioxide, and subsequent export of carbon to the ocean floor, make them an important influence on global climate change, as the burning of fossil fuels pumps greenhouse gasses into the atmosphere. Understanding phytoplankton and the factors effecting their abundance and distribution is thus an important goal.

Phytoplankton contain chlorophyll *a*, a molecule which allows them to convert light absorbed from the sun into chemical energy which fuels life functions like growth and reproduction. Measuring chlorophyll concentration does not accurately determine the local abundance of phytoplankton—the ratio of the amount of chlorophyll contained in a cell to the mass of the cell varies greatly—but chlorophyll nonetheless provides a useful way of studying the phytoplankton community. Chlorophyll fluoresces: a fraction of the light it absorbs is re-emitted at a lower frequency. This property makes chlorophyll concentration a very easily, cheaply, and quickly measured variable related to phytoplankton biomass, allowing the collection of information about ecosystem structure over a wide range of spatial and temporal scales.

Aside from the CalCOFI bottle data used in Chapter 4, all the chlorophyll data used in the observational portions of this work are obtained from in situ fluorescence measurements. A fluorometer towed behind a ship for a total of over 5000 kilometers provided the chlorophyll data analyzed in Chapter 3. Another fluorometer, carried a total distance of almost 4000 kilometers by an underwater glider, produced the chlorophyll data presented in Chapter 4.

Throughout much of the world's oceans, chlorophyll concentration increases markedly from the surface downward, reaching a peak, often quite sharp, before

decaying toward zero in the deep dark waters below the euphotic zone. The so-called deep chlorophyll maximum (DCM), despite its ubiquity, is poorly understood. Some often-cited qualitative explanations for the creation of the DCM do not produce a subsurface maximum when implemented in simple mathematical models. Determining mechanisms which could lead to the formation of a DCM, and eliminating others which cannot is the task undertaken in Chapter 2. Simple, one-dimensional, steady-state phytoplankton models are used to test a variety of mechanisms, and to investigate the influence of parameters such as phytoplankton growth rate and sinking velocity.

Many observers have described the horizontal distribution of plankton as 'patchy'. The goal of Chapter 3 is to characterize this patchiness, as expressed in the chlorophyll field, and explain its origin. Regarding chlorophyll as a passive, reactive tracer, two mechanisms which could lead to small- and meso-scale structure in its horizontal distribution are: 1) reaction—chlorophyll sources or sinks, e.g. spatially varying growth/death rates of phytoplankton; and 2) advection—stirring of large-scale chlorophyll gradients by ocean currents. If the latter is the dominant mechanism chlorophyll would be expected to display a distribution statistically similar to that of a passive conservative tracer. By comparing the distributions of chlorophyll and temperature, it is possible to estimate to what extent the two tracers are influenced by the same processes.

CalCOFI cruises have been measuring physical and biological properties of the water off the southern California coast several times per year for decades, making this region of the ocean one of the most well-sampled anywhere in the

world. The large-scale (~100-1000 km) physical and biological structure and dynamics of the area are thus well known. This knowledge base provides a context for interpretation of smaller-scale observations in the region; such observations can illuminate small-scale processes not resolved by CalCOFI cruises, providing a more complete understanding of the dynamics of the ecosystem as a whole. Chapter 4 takes a step in this direction, comparing high resolution (~3 km in the horizontal, and ~1 m in the vertical) glider data from CalCOFI Line 93 with coarser-resolution measurements made in the same location over the preceding quarter-century.

Chapter 2

Simple Models of Steady Deep Maxima in Chlorophyll and Biomass

Abstract of Chapter 2

Possible mechanisms behind the observed deep maxima in chlorophyll and phytoplankton biomass in the open ocean are investigated with simple, one-dimensional ecosystem models. Sinking of organic matter is shown to be critical to the formation of a deep maximum in biomass in these models. However, the form of the sinking material is not of primary importance to the system: in models with sinking of detritus, sinking of one phytoplankton species, and sinking of all phytoplankton, the effect is qualitatively the same. In the two-compartment nutrient-phytoplankton model, the magnitude of the deep biomass maximum depends more strongly on sinking rate and diffusivity than on growth and death rates, while the depth of the maximum is influenced by all four parameters. A model with two phytoplankton groups that exhibit distinct growth rate characteristics and chlorophyll contents shows how a deep chlorophyll maximum could form in the absence of sinking. In this model, when separate compartments are included for nitrate and ammonia, it is possible to distinguish between new and regenerated

5

production, and the phytoplankton group which makes up the deep chlorophyll maximum is found to carry out almost all of the new production. Variation of eddy diffusivity with depth is also investigated, and is found not to fundamentally alter results from models with constant diffusivity.

2.1 Overview

The deep chlorophyll maximum (DCM) is a ubiquitous feature of many regions of the world's oceans (Venrick et al., 1973; Cullen, 1982). As fluorescence is perhaps the most easily measured biological oceanic variable, the DCM is the most widely known feature of the ocean ecosystem. A permanent characteristic throughout much of the tropics, deep chlorophyll maxima are also familiar features in temperate regions, although usually subject there to strong seasonal variability (Venrick, 1993; Winn et al., 1995).

Deep maxima in phytoplankton biomass are also common. Such a deep biomass maximum (DBM) is evident in the tropical eastern Pacific at 5.5° N (Fig. 2.1). Shown here are typical profiles of in vivo fluorescence of chlorophyll a, an approximate measure of chlorophyll concentration (Lorenzen, 1966), and beam attenuation coefficient, an approximate measure of particulate organic carbon (POC) (Bishop, 1999). Prominent deep maxima are evident in both. A DCM often occurs without an accompanying DBM, however (Winn et al., 1995). This is due to variation in the chlorophyll-to-biomass ratio, which may vary by as much as a factor of 10 (Cullen and Lewis, 1988). The effect is exemplified in typical profiles of fluorescence and beam attenuation coefficient from the tropical Pacific near Hawaii

(Fig. 2.2). While a strong DCM is present, there is no significant deep maximum apparent in POC. A DBM is not implied by the existence of a DCM, and when both are present they often differ in vertical structure (Kitchen and Zaneveld, 1990; Fennel and Boss, 2003), so it is important to distinguish between the two signatures. On the other hand, since the chlorophyll-to-biomass ratio generally increases with depth in the euphotic zone, the presence of a DBM does typically imply a DCM, and any mechanism which causes the former also causes the latter.

A number of mechanisms have been proposed for the formation of deep maxima, and indeed it seems likely that a variety of effects are involved. In a recent paper, Fennel and Boss (2003) investigate the separation of the DCM and DBM, and possible causes of each. Efforts to model the DCM date back to 1949, when Riley, Stommel, and Bumpus tackled the problem in their seminal paper. Several fairly complex models of the planktonic ecosystem exist (e.g. Jamart et al., 1977; Varela et al., 1992), which are able to accurately match observations. Rather than striving to reproduce precisely the features of a specific set of observations, the aim of this paper is to use simple, one-dimensional ecosystem models to examine the feasibility of a few basic mechanisms which might give rise to deep maxima in chlorophyll and biomass.

The models presented here are closed, in the sense that there is no exchange of material across the model domain boundaries. Since there are essentially no live phytoplankton deeper than a few hundred meters, most models have been limited to this region. However, nutrient profiles have typically not reached their asymptotic, deep-ocean values at the bottom of this layer, so these models include an upward

diffusive flux of nutrients through the bottom boundary of their domain. The magnitude of this flux depends on the position of the bottom boundary, and on the boundary conditions. As our goal is to understand how vertical distributions of phytoplankton and variables relevant to their ecosystem arise, we extend our models to a depth great enough to ensure that all model variables attain their asymptotic values.

The models are kept as simple as possible, allowing isolation of the most fundamental processes underlying the complex ecological system. We subscribe to Occam's razor, which suggests that the simplest explanation of a phenomenon is intrinsically best. In addition, a sufficiently simple model allows a full search of parameter space, permitting a more complete understanding of the mathematical system than would be possible in models of higher complexity.

2.2 Basic Assumptions

It is convenient and sensible to deal in some currency when modeling the plankton ecosystem. The most common choice, and the one we make here, is nitrogen (e.g. Steele, 1974) because it is assumed to be the limiting nutrient of photosynthetic growth. Thus, $P(z)$ represents the concentration of phytoplankton as a function of depth in terms of the nitrogen it contains. Minimizing the number of other forms (compartments) in which the currency can exist is essential if one hopes to form a simple model. So we begin, in our simplest models, without a zooplankton compartment; rather than being modeled explicitly, the effects of grazing are included in the net phytoplankton growth rate. Similarly, we begin with the

assumption that all phytoplankton exhibit the same environment-dependent rates of biological activity, and none of our models include more than two such phytoplankton groups.

There are several other significant simplifications in our models. Each variable is treated as a continuum, whereas, of course, real plankton are discrete (see, e.g. Young, 2001). Only one spatial dimension is modeled (the vertical). Thus, such phenomena as horizontal patchiness in the distribution of phytoplankton (see Denman et al., 1977 for a discussion) and the horizontal transport of plankton and nutrients are not considered. Though the ocean is a time-dependent environment, we consider only the steady-state solutions to the models. As the DCM is a permanent feature of large regions of the ocean, it seems reasonable to regard the changes it undergoes as fluctuations about a steady-state distribution. The models' intrinsic time scales, determined by the rates of biological activity and by diffusion and sinking, coupled with the attenuation length of light, are all of the order of tens of days for the parameter ranges considered. The steady solution applies if it has been at least this long since a major perturbation in the system. Modeled light intensity depends only on depth (i.e. there is no self-shading) and no other properties (except, sometimes, turbulent diffusivity) are explicit functions of depth. The only process which is directly affected by light is photosynthetic growth, so depth dependence of chlorophyll-to-nitrogen ratio, remineralization rate, zooplankton grazing rate, etc. is not included. The reasoning behind this choice is that allowing explicit vertical variation in more processes would introduce additional degrees of freedom to the modeling problem, clouding understanding of the mechanisms at work.

2.3 How Simple is Too Simple?

One popular explanation of the deep maxima is outlined by Mann and Lazier (1996) in their recent textbook: "…a certain amount of nitrate is transported upward through the nutricline by turbulent diffusion. This process leads to more rapid growth of the phytoplankton population and the formation of a zone of maximum phytoplankton biomass, the 'chlorophyll maximum', just above the nutricline. The upper boundary of this zone is set by the supply of nutrients from below, and the lower boundary is set by the availability of light from above". A simple model simulating the process described in the above explanation would have two compartments: phytoplankton P and nutrients N. The net rate at which nitrogen flows from N to P may be represented by $\mu(N,P,z)$, where z, the vertical coordinate, is zero at the surface and increases upward.[1] $\mu(N,P,z)$ is the rate of total phytoplankton growth minus all losses, including those due to death. If we denote the turbulent diffusivity by $\kappa(z)$, we obtain the model equations

$$\frac{\partial N}{\partial t} = -\mu(N,P,z) + \frac{\partial}{\partial z}\left(\kappa \frac{\partial N}{\partial z}\right), \tag{2.1}$$

$$\frac{\partial P}{\partial t} = \mu(N,P,z) + \frac{\partial}{\partial z}\left(\kappa \frac{\partial P}{\partial z}\right), \tag{2.2}$$

---

[1] Our convention, throughout this chapter, will be to use italic capital Roman letters for nitrogen compartments, italic lower- case Roman letters for independent variables, Greek letters for parameters which may be functions of independent variables or compartments, and normal-text capital Roman letters for other (constant) parameters.

with the boundary conditions

$$\frac{\partial N}{\partial z} = \frac{\partial P}{\partial z} = 0 \quad \text{at} \quad z = 0,$$

$$N = 1, \quad P = 0 \quad \text{at} \quad z = -\infty$$

The bottom boundary conditions reflect the normalization of N and P such that the deep nutrient concentration is 1. That is, the dimensional concentrations of nutrients and phytoplankton have been divided by the concentration of nitrogen at great depth, which we take to be 10 mmol l^{-1} (Edwards et al., 2000), so that N and P are unitless. The surface boundary conditions are chosen so as to make the diffusive flux of N and P through the surface zero.

In this model, growth of plankton uses up nutrients, and when plankton die they are immediately converted back into dissolved nutrients. As we are interested in the steady-state solution, we set the time derivatives of N and P equal to zero and solve the system numerically using Newton's method. In seeking the steady solution, we are assuming that such a solution exists and is stable. The assumption of existence is justified once a solution is found, and stability is proven in the Appendix to this chapter. Although we do not prove explicitly that the models presented in later sections have stable solutions, stability is favored by the diffusive nature of the models. Stability of models of this type has been examined by a number of authors (Criminale and Winter, 1974; Lima et al., 2002; Edwards et al., 2000).

The system described above appears reasonable, and certainly it is simple, but it can be shown that this system cannot yield a realistic deep maximum in P. In

order to show this, we first define $S = N + P$ to be the total concentration of nitrogen in any form. It is easy to solve for S: by adding Eqs. (2.1) and (2.2), we obtain

$$\frac{\partial}{\partial z}\left(\kappa\frac{\partial S}{\partial z}\right) = 0. \tag{2.3}$$

Transforming the boundary conditions gives $\partial S / \partial z = 0$ at $z = 0$ and $S = 1$ at $z = -\infty$; the solution is $S(z) = 1$. Thus $N + P = 1$ and any deep maximum in P must accompany a deep minimum in N; that is, a deep phytoplankton maximum and a nutricline cannot coexist. This result is neither dependent on the form of the growth rate term nor on the behavior of diffusivity with depth. In order to understand the mechanisms behind a steady DBM, it is necessary to look beyond this simple model and the explanation it represents.

However, solutions to this over-simplified model provide a useful reference against which to compare results from more realistic models. To obtain these solutions we must choose functional forms for the growth and diffusivity terms. Since nutrients and light are both necessary for photosynthetic growth, the rate at which P grows should be an increasing function of N, and an increasing function of light intensity, $PAR(z)$ (photosynthetically active radiation). If we take these functions to be as simple as possible, i.e. assume linear proportionality, we arrive at $\tilde{G} N[PAR(z)]$ as the growth rate, where $\tilde{G}$ is a constant. Assuming K, the attenuation coefficient of $PAR(z)$, is constant with depth, $PAR(z) = e^{Kz} PAR(0)$. Defining $G \equiv \tilde{G} / PAR(0)$, our growth rate is GNe^{Kz}.

Note that the values assigned to G, sometimes as large as 100 day⁻¹, may appear at first to be unrealistically high, but that to get a growth rate of G, nutrient concentration and light level would both have to reach their maximum values (1 in both the cases) at the same location. As light level is maximum at the surface and nutrient concentration is maximum at great depth, this never happens, and the actual phytoplankton growth rate is always much less than G.

Following the Michaelis–Menten equation, a growth rate with a half-saturation dependence on nutrient or light levels is perhaps more traditional in this kind of model (Jamart et al., 1977; Franks et al., 1986; Fasham et al., 1990). However, the euphotic ocean operates mostly at low N, where saturation is irrelevant, and we have found that such elaborations change the solutions only slightly. We have therefore opted for simplicity. Adding a constant specific death rate, D (which includes respiration as well as grazing and other modes of physiological death), and taking diffusivity to be constant with depth, we obtain the system

$$\frac{\partial N}{\partial t} = -GNPe^{Kz} + DP + \kappa\frac{\partial^2 N}{\partial z^2}\,, \tag{2.4}$$

$$\frac{\partial P}{\partial t} = GNPe^{Kz} - DP + \kappa\frac{\partial^2 P}{\partial z^2}\,, \tag{2.5}$$

with the same boundary conditions as before.

A steady deep phytoplankton maximum is not consistent with this system, because any such maximum would have to occur in a location darker and poorer in nutrients, and therefore with a slower growth rate, than the surface. A typical solution is shown in Fig. 2.3. The parameter values are G = 20 day⁻¹, D = 0.1 day⁻¹,

and $\kappa = 10^{-4}$ m^{2}s^{-1}. The phytoplankton maximum is, as it must be, at the surface. In the model equations above, the bottom boundary condition is applied at $z = -\infty$, but for computational purposes, we apply this condition at a finite depth deep enough that change with depth has ceased; in this case the bottom boundary is at 800 m. Note that in Fig. 2.3 and subsequent figures, only the surface region of this model domain is depicted, so that near-surface behavior may be more clearly seen.

2.4 Sinking of Phytoplankton

Deep biomass maxima do exist in many areas, particularly in the tropics. In order to simulate the DBM with our model, the total amount of nitrogen in the surface layer must be depleted. The simplest mechanism that can maintain a depletion against the homogenizing effect of diffusion is the sinking of nitrogen. Accordingly, we introduce a constant phytoplankton sinking rate. The modified system is

$$\frac{\partial N}{\partial t} = -GNP\mathrm{e}^{\mathrm{K}z} + \mathrm{D}P + \kappa \frac{\partial^2 N}{\partial z^2}, \tag{2.6}$$

$$\frac{\partial P}{\partial t} = GNP\mathrm{e}^{\mathrm{K}z} - \mathrm{D}P + \kappa \frac{\partial^2 P}{\partial z^2} - \mathrm{W}\frac{\partial P}{\partial z}, \tag{2.7}$$

with the boundary conditions

$$\kappa \frac{\partial N}{\partial z} = \mathrm{W}P - \kappa \frac{\partial P}{\partial z} = 0 \quad \text{at} \quad z = 0,$$

$$N = 1, \quad P = 0 \quad \text{at} \quad z = -\infty.$$

W is the sinking rate, and the surface boundary condition on *P* has been changed so that the total flux of phytoplankton (diffusive plus sinking) through the surface is zero. The solution has a marked increase in phytoplankton concentration from the surface to the deep maximum, due to the nitrogen depletion of the surface caused by sinking of phytoplankton (Fig. 2.4). As long as the chlorophyll-to-biomass ratio is constant or increasing with depth, this DBM is also a DCM. Of the four terms in the *P* equation above (Eq. (2.7)), the dominant balance throughout the euphotic zone is between growth and death (Fig. 2.5(a)). However, as growth and death only move nitrogen from one compartment to the other, they do not directly affect the profile of total nitrogen (*N*+*P*). It is a balance between sinking and diffusion that determines this profile. The flux of total nitrogen must be zero everywhere, so the downward flux of nitrogen due to the sinking of *P* is balanced by an upward diffusive flux of total nitrogen

$$-\kappa\frac{\partial N}{\partial z} - \kappa\frac{\partial P}{\partial z} + \mathrm{W}P = 0\,. \tag{2.8}$$

This flux balance is illustrated in Fig. 2.5(b), which shows as functions of depth the vertical diffusive flux of nutrients (the first term in Eq. (2.8)) and phytoplankton (the second term), and the vertical flux of phytoplankton due to sinking (the third term). Sinking of phytoplankton rains nitrogen out of the surface layer, and diffusion works to replenish it.

The model, in the form above, includes five variable parameters: G, D, κ, K, and W. We now nondimensionalize the system by scaling the vertical coordinate, *z*, by the attenuation length, K^{-1}, and dividing Eqs. (2.6) and (2.7) by D, the death rate.

(Note that the variables N and P are already nondimensional, having been scaled by the limiting nutrient value at depth.) After making the following substitutions:

$$z^* \leftarrow Kz,$$
$$t^* \leftarrow tD,$$
$$G^* \leftarrow G/D,$$
$$W^* \leftarrow \kappa K^2/D$$

and dropping the asterisks, the nondimensional system obtained looks exactly like the dimensional system above, except that K and D are equal to unity. The full parameter space of this model therefore has only three dimensions, and is investigated rather easily.

Numerical solutions were obtained for the region of parameter space defined by the (dimensional) values in Table 1. A DBM is a feature in solutions to the system throughout this entire region. For particularly small sinking velocity and large diffusivity, the surface concentration of phytoplankton approaches that at the deep maximum. In these cases, diffusion dominates, and the sinking is not able to deplete the total nitrogen in the surface layer. In the limit as the ratio $W/K\kappa$ approaches zero, the model reduces to the trial system of Section 2.3, and the plankton maximum is at the surface.

Phytoplankton concentration and the depth of the deep maximum vary considerably across the explored block of G–κ–W parameter space. Each contour plot in Fig. 2.6 represents a two-dimensional slice through the three-dimensional parameter space. Because small diffusivities and fast sinking rates deplete the surface layer of nitrogen, they lead to small phytoplankton concentrations which

peak well below the surface; larger diffusivities and slower sinking rates yield larger phytoplankton concentrations with shallower maxima (Fig. 2.6, top row).

At the surface, phytoplankton concentration is determined by the extent of the surface nitrogen depletion. The depletion is most complete, and hence the surface value of P is smallest, when W is large and κ is small (Fig. 2.6, right-hand column). Though the dependence is weak, P at the surface decreases with increasing growth rate (G), because faster-growing phytoplankton are more efficient at depleting surface nitrogen.

The phytoplankton concentration at the deep maximum is not a function of G (note the vertical contour lines in the lower two panels of the middle row in Fig. 2.6). The axes in Fig. 2.6 are scaled logarithmically. As indicated by the even spacing in the G direction of the contours in the lower two panels of the left-hand column in Fig. 2.6, the depth of the deep maximum is proportional to the logarithm of G. Any vertical line drawn from top to bottom across either of these panels represents a range of G from 2.5 to 62.5 day^{-1} and spans about 64 m (3.2/K) of depth contours.

If the sinking flux of phytoplankton is sufficient to deplete the surface layer of nitrogen, as it is throughout most of our parameter space, $P(z = 0)$ will be small. Using this fact, we can infer the effect of varying the value of G, and understand the behavior observed in Fig. 2.6. Consider the NP system with sinking (Eqs. (2.6) and (2.7)) after nondimensionalizing and making the substitutions $z \rightarrow z'+H$ and $G \rightarrow G'e^{-H}$:

$$\frac{\partial N}{\partial t} = -\mathrm{G}'NP\mathrm{e}^{z'} + P + \kappa\frac{\partial^2 N}{\partial z'^2}, \tag{2.9}$$

$$\frac{\partial P}{\partial t} = \mathrm{G}'NP\mathrm{e}^{z'} - P + \kappa\frac{\partial^2 P}{\partial z'^2} - \mathrm{W}\frac{\partial P}{\partial z'}, \tag{2.10}$$

with the boundary conditions

$$\kappa\frac{\partial N}{\partial z'} = \mathrm{W}P - \kappa\frac{\partial P}{\partial z'} = 0 \quad \text{at} \quad z' = -\mathrm{H},$$

$$N = 1, \quad P = 0 \quad \text{at} \quad z' = -\infty.$$

This system looks very similar to the original one. The only thing stopping us from concluding that changing G just amounts to shifting the vertical coordinate is that the surface boundary condition is applied at $z' = -\mathrm{H}$, rather than $z' = 0$. Now, under the assumption that P is small near the surface, (9) and (10) may be approximated in the surface region by

$$\kappa\frac{\partial^2 N}{\partial z'^2} \approx 0,$$
$$\kappa\frac{\partial^2 P}{\partial z'^2} \approx \mathrm{W}\frac{\partial P}{\partial z'}.$$

Integrating these from $z' = -\mathrm{H}$ to 0, and applying the BC's for $z' = -\mathrm{H}$, we find

$$\kappa\frac{\partial N}{\partial z'} \approx \mathrm{W}P - \kappa\frac{\partial P}{\partial z'} \approx 0 \quad \text{at} \quad z' = 0,$$

which suggests that applying the boundary conditions at $z' = 0$ provides a reasonable approximation. Thus if $P(z = 0)$ is small, the approximate solution for $\mathrm{G} = \mathrm{XG}_0$, where X is an arbitrary constant, may be obtained from the solution for $\mathrm{G} = \mathrm{G}_0$ by shifting it upward by the amount $\Delta z = -\ln(\mathrm{X})$. This explains why the magnitude of the maximum is not a function of G, and why the depth of the

maximum changes by about 3.2 attenuation lengths when the value of G changes by a factor of 25: $\ln(25) \approx 3.2$.

Though we have scaled the parameter D out of our model equations by nondimensionalization, and hence it is not varied in our study of parameter space, we can still consider the effect of varying the death rate in the original, dimensional NP model with sinking. Referring back to that system, Eqs. (2.6) and (2.7), we can see that the solution for the parameter set $\{G, W, \kappa, D\}$, where $D = XD_0$, is the same as the solution for the parameter set $\{G/X, W/X, \kappa/X, D_0\}$. Since we have a solution set for a single death rate, D_0, we can see the result of increasing (decreasing) the death rate by a given factor by decreasing (increasing) the other parameters by that same factor. So, for example, since we know that the phytoplankton concentration at the DBM does not depend on G, we can infer the dependence of this magnitude on death rate from Fig. 2.6, middle panel, top row. Changing D corresponds to moving along lines which run across this figure from lower left to upper right at an angle of 45°. As the contours themselves are nearly parallel to these lines, the phytoplankton concentration at the maximum is only weakly affected by the value of the death rate.

In the NP model with sinking, the magnitude of the phytoplankton concentration is largely a function of the physical variables κ and W and not of the biological variables G and D (although the sinking rate, W, is certainly influenced by biology, we classify it as a physical variable because it depends directly on particle size and density). The biological variables are important, however, in

determining the depth of the DBM. As the contours in the lower two panels of the left-hand column of Fig. 2.6 are more nearly horizontal than vertical, the depth of the maximum depends more strongly on G than on either of the physical variables.

2.5 The Effects of Variable Diffusivity

The eddy diffusivity, κ, is much larger within the mixed layer than beneath. It has occasionally been suggested that this transition could be important in the formation of a deep phytoplankton maximum. In this section, we explore the consequences of introducing a step-function diffusivity profile into the NP model with sinking from the previous section. The diffusive terms in the model equations are rewritten as $\partial/\partial z(\kappa \partial N/\partial z)$ and $\partial/\partial z(\kappa \partial P/\partial z)$, which are the valid forms when κ is a function of z.

The effect of introducing a 60-m-deep mixed layer to the model is shown in Fig. 2.7(a). The value of κ is increased by a factor of 10 in this mixed layer, but otherwise all parameter values are retained from Fig. 2.4. For comparison, the nutrient and plankton profiles for the constant-κ case are shown as dashed lines. The deep maximum is at a depth of approximately 85 m, and so is beneath the base of the mixed layer. While there are noticeable changes in the profile of phytoplankton within the mixed layer itself, in the deeper water the profile is essentially unaffected.

Next, consider the less typical case of a mixed layer whose base lies beneath the deep maximum. Fig. 2.7(b) shows the same 'reference' profiles as before together with the profiles obtained for the case of a 120-m mixed layer. Here, the

diffusivity is left unchanged within the mixed layer, but it is decreased by a factor of 10 below the mixed layer base. Maintaining the value of κ at the deep maximum at 10^{-4} m^2 s^{-1} in both cases allows the resulting profiles to be compared directly with the reference profile. Once again, the changes induced by the introduction of the mixed layer are relatively minor. Thus, in our simple models, the characteristics of the deep maximum depend in large part on the value of κ in the vicinity of the maximum, and only weakly on the behavior of the profile of κ at other depths.

2.6 A Third Compartment

We have emphasized that sinking is a crucial process in the formation of the DBM as represented in our simple model with only nutrient and phytoplankton compartments. The question remains, however, whether a deep phytoplankton maximum may result from a model without the surface-depleting effect of sinking, but with additional, nonphytoplankton nitrogen compartments. With this in mind, we introduce a third compartment, T, here a detrital pool. The new free parameter is a remineralization rate, R, which governs the transformation of detritus back into dissolved nutrients, parameterizing nutrient recycling via the microbial loop. The model equations are

$$\frac{\partial N}{\partial t} = -\text{G}NP\text{e}^{\text{K}z} + \text{R}T + \kappa\frac{\partial^2 N}{\partial z^2}, \tag{2.11}$$

$$\frac{\partial P}{\partial t} = \text{G}NP\text{e}^{\text{K}z} - \text{D}P + \kappa\frac{\partial^2 P}{\partial z^2}, \tag{2.12}$$

$$\frac{\partial T}{\partial t} = \mathrm{D}P - \mathrm{R}T + \kappa \frac{\partial^2 T}{\partial z^2}, \tag{2.13}$$

subject to the boundary conditions

$$\frac{\partial N}{\partial z} = \frac{\partial P}{\partial z} = \frac{\partial T}{\partial z} = 0 \quad \text{at} \quad z = 0,$$

$$N = 1, \quad P = T = 0 \quad \text{at} \quad z = -\infty.$$

Numerical simulations were carried out scanning a large physically and biologically reasonable region of parameter space similar to the one described for the two-compartment model in Section 2.4; κ varied from 10^{-5} to 10^{-2} m^2 s^{-1}, G varied from 1 to 100 day^{-1}, and the remineralization rate, R, took on values from 0.001 to 1.25 day^{-1}. While there is a region of this parameter space in which deep maxima do occur, the increase in phytoplankton concentration from the surface to the deep maximum is never as much as 3% of the deep nitrogen concentration. The strongest such maximum (i.e. the one with the greatest increase in phytoplankton concentration from the surface to the maximum) occurs when $G = 100 \, \text{day}^{-1}$, $R = 0.0135 \, \text{day}^{-1}$, and $\kappa = 0.00082 \, \text{m}^2 \, \text{s}^{-1}$, and is shown in Fig. 2.8.

The third compartment, T, could also be regarded as a zooplankton pool. In that case, D represents a constant (independent of T) grazing rate, and R a zooplankton loss rate, including death and excretion. Similar results are found when the grazing rate is linear in T (when the DP terms in the system above are replaced by DPT) unless the grazing rate is so large that no stable nontrivial solution exists. This suggests that, provided they have no explicit depth dependence, no number of

additional compartments is likely to lead to the formation of a large and robust DBM in a simple one-dimensional ecosystem model without sinking.

When sinking of detritus is included in the model above, its behavior is qualitatively very similar to that displayed by the two-compartment model with sinking from Section 2.4. Fig. 2.9 shows the solution for this case when the value of R is 0.2 day^{-1} and the rest of the parameter values are retained from Fig. 2.4. The phytoplankton and nutrient profiles are quite similar to those shown in Fig. 2.4; the biggest difference is that depletion of nitrogen in the surface layer is less effective in the three-compartment model. The sinking flux is smaller because only detritus sinks in this case and the concentration of detritus is smaller than is the concentration of phytoplankton in the NP model. The result is a higher concentration of phytoplankton at the surface. This slight difference is not due to any distinct effects of detrital sinking versus sinking of live phytoplankton. Of primary importance to the model ecosystem is only the magnitude of the sinking flux of organic matter, not the form that matter takes.

2.7 Multiple Phytoplankton Species

Though sinking is a prerequisite for the formation of a steady DBM in our NP model, variation with depth in the chlorophyll-to-biomass ratio can lead to a deep chlorophyll maximum. If photoadaptation is a dominant process in determining the distribution of chlorophyll—that is, if phytoplankton in deeper water develop significantly higher chlorophyll-to-biomass ratios in response to the low light intensity than do those near the surface—a strong DCM may form without a

phytoplankton maximum. In fact, a DCM may form even in the absence of photoadaptation if multiple species of phytoplankton are considered, each with its own chlorophyll-to-biomass ratio and its own response to light level. Consider the simple NP system from Section 2.3 with constant κ and no sinking, but with phytoplankton split into two groups, P and Q. These groups will henceforth be referred to as 'species', with the understanding that each may actually represent an aggregate of many species with similar biological characteristics. The new system is

$$\frac{\partial N}{\partial t} = -\mathrm{G}_P NP\mathrm{e}^{\mathrm{K}z} + \mathrm{D}_P P - \mathrm{G}_Q NQ\mathrm{e}^{2\mathrm{K}z} + \mathrm{D}_Q Q + \kappa\frac{\partial^2 N}{\partial z^2}, \qquad (2.14)$$

$$\frac{\partial P}{\partial t} = \mathrm{G}_P NP\mathrm{e}^{\mathrm{K}z} - \mathrm{D}_P P + \kappa\frac{\partial^2 P}{\partial z^2}, \qquad (2.15)$$

$$\frac{\partial Q}{\partial t} = \mathrm{G}_Q NQ\mathrm{e}^{2\mathrm{K}z} - \mathrm{D}_Q Q + \kappa\frac{\partial^2 Q}{\partial z^2}, \qquad (2.16)$$

with the boundary conditions

$$\frac{\partial N}{\partial z} = \frac{\partial P}{\partial z} = \frac{\partial Q}{\partial z} = 0 \quad \text{at} \quad z = 0,$$

$$N = 1, \quad P = Q = 0 \quad \text{at} \quad z = -\infty.$$

The specific growth rates of P and Q, $\mathrm{G}_P N\mathrm{e}^{\mathrm{K}z}$ and $\mathrm{G}_Q N\mathrm{e}^{2\mathrm{K}z}$, respectively, differ both in their surface values and in the way they decay with depth. The growth rate of P retains its linear dependence on light, and so has an e-folding length of K^{-1}. The growth rate of Q, on the other hand, is quadratic in light, and so has an e-folding length of $\frac{1}{2}\mathrm{K}^{-1}$; that is, Q's growth rate decays with depth twice as fast as that of P. The surface growth rate of Q, G_Q, is chosen to be larger than G_P. The result is that phytoplankton P is better adapted for high-nutrient, low-light

environments, while Q is better adapted for low-nutrient, high-light ones. The quadratic form of the growth rate of Q is chosen as a simple way to achieve this adaptive difference between P and Q. One factor which could contribute to differences in rates of decay of growth rates with depth is that the attenuation coefficient of light in sea water is frequency dependent, and the absorption spectrum of phytoplankton varies from species to species (Yentsch and Yentsch, 1979; Bricaud et al., 1983; Falkowski and Kiefer, 1985). This effect is relatively minor, however, and here, the dominant factor in the foreshortening of the growth rate profile is that phytoplankton Q functions less efficiently in lower-light conditions.

The system develops a pronounced deep maximum in P, the species that is better equipped to survive in dimmer light. The maximum concentration of Q occurs at the surface. Such vertical separations between different phytoplankton communities are consistent with observations (e.g. Venrick, 1993). Although the model still produces no DBM, a DCM may exist if the deeper species has a higher chlorophyll-to-biomass ratio, a reasonable assumption since a species which lives mainly in a low-light environment would need more chlorophyll. This effect is demonstrated in Fig. 2.10, in which plankton P has a chlorophyll-to-biomass ratio which is larger than that of plankton Q by a reasonable (Bricaud et al., 1983) factor of four. Biomass has been assumed, here, to be proportional to nitrogen content via its Redfield ratio to the other major elemental constituents of phytoplankton (Redfield et al., 1982). Photoadaptation within each species, if included in the model, would enhance this DCM. Thus the 'NPQ' model presented in this section

provides a possible explanation of deep chlorophyll maxima which, like that shown in Fig. 2.2, exist in the absence of a DBM.

It may seem that a DCM formed by the mechanism simulated in this model would not be of major ecological significance, since it is due to changes in chlorophyll content and not to phytoplankton abundance. However, this DCM represents a maximum in a species which dominates at depth, and so monopolizes the new nutrients diffusing up from below. Thus, the organisms that comprise this DCM are likely to be responsible for the bulk of the new production (see, e.g., Jenkins and Goldman, 1985).

To investigate this aspect of the model system further, we split the nutrient compartment into new nutrients, N, and recycled or 'old' nutrients, O. The N compartment thus represents nitrate, while O is made up largely of ammonium. When phytoplankton die, they become O nutrients. The parameter R is a remineralization rate—the rate at which recycled nutrients are broken down by bacteria and transformed back into nitrate. In this model, both types of nutrients are taken up indiscriminately by both types of phytoplankton, so that, for a given set of parameters, the division of nutrients into two separate compartments has no effect on the profiles of plankton or of total nutrients. Thus the phytoplankton dynamics of the model are unchanged, and the division allows a distinction to be made between new and regenerated production (Fasham et al., 1990). The 'NOPQ' system is

$$\frac{\partial N}{\partial t} = -G_P N P e^{K z_P} - G_Q N Q e^{K z_Q} + R O + \kappa \frac{\partial^2 N}{\partial z^2}, \qquad (2.17)$$

$$\frac{\partial O}{\partial t} = -G_P O P e^{K z_P} + D_P P - G_Q O Q e^{K z_Q} + D_Q Q - R O + \kappa \frac{\partial^2 O}{\partial z^2}, \qquad (2.18)$$

$$\frac{\partial P}{\partial t} = G_P(N+O)Pe^{K_{z_P}} - D_P P + \kappa \frac{\partial^2 P}{\partial z^2}, \tag{2.19}$$

$$\frac{\partial Q}{\partial t} = G_Q(N+O)Qe^{K_{z_Q}} - D_Q Q + \kappa \frac{\partial^2 Q}{\partial z^2}, \tag{2.20}$$

with the boundary conditions

$$\frac{\partial N}{\partial z} = \frac{\partial O}{\partial z} = \frac{\partial P}{\partial z} = \frac{\partial Q}{\partial z} = 0 \quad \text{at} \quad z = 0,$$

$$N = 1, \quad O = P = Q = 0 \quad \text{at} \quad z = -\infty.$$

In Fig. 2.11(a), the solution to this system is plotted for the parameter values from Fig. 2.10 and with $R = 0.1\,\text{day}^{-1}$. The phytoplankton profiles are the same as in Fig. 2.10, and the sum of the two types of nutrients yields the total nutrient profile from Fig. 2.10. The rates of primary production based on new and recycled nutrients by each phytoplankton species are shown in Fig. 2.11(b). New production is shown as thick lines, recycled production as thin lines, solid lines refer to phytoplankton P, and dashed lines to Q. So, for example, the thick solid line is new production by P, which is just $G_P NPe^{K_{z_P}}$. As expected, the new production is dominated by P.

The remineralization rate, R, has been found to increase with decreasing light intensity (Olson, 1981), but we take it to be constant here. In addition, a portion of the nitrate which is taken up near the surface has been remineralized within the euphotic zone, and growth based on this portion may not constitute new production in the strictest sense. The likely result of both these simplifications is that we will overestimate the concentration of nitrate in the surface layer, and thus also the proportion of new production carried out by phytoplankton Q. When the

'false' new production is eliminated by allowing remineralization only below the euphotic zone, the main effect is to decrease the rate of new production by phytoplankton Q even further. Much of the nitrate driving new production in the euphotic zone is diffused up from beneath, and so must be balanced by export of nitrogen, in some form, from the euphotic zone. This export is generally attributed to sinking of organic matter, but in the present model, as there is no sinking, the export is carried out by diffusion.

Including sinking in the above model allows for a perhaps more realistic export flux mechanism, and also illustrates the combined effects of surface nitrogen depletion and variation in chlorophyll-to-biomass ratio. With sinking of phytoplankton P, the system becomes

$$\frac{\partial N}{\partial t} = -\mathrm{G}_P NP\mathrm{e}^{\mathrm{K}z_P} - \mathrm{G}_Q NQ\mathrm{e}^{\mathrm{K}z_Q} + \mathrm{R}O + \kappa\frac{\partial^2 N}{\partial z^2}, \tag{2.21}$$

$$\frac{\partial O}{\partial t} = -\mathrm{G}_P OP\mathrm{e}^{\mathrm{K}z_P} + \mathrm{D}_P P - \mathrm{G}_Q OQ\mathrm{e}^{\mathrm{K}z_Q} + \mathrm{D}_Q Q - \mathrm{R}O + \kappa\frac{\partial^2 O}{\partial z^2}, \tag{2.22}$$

$$\frac{\partial P}{\partial t} = \mathrm{G}_P (N+O)P\mathrm{e}^{\mathrm{K}z_P} - \mathrm{D}_P P + \kappa\frac{\partial^2 P}{\partial z^2} - \mathrm{W}_P\frac{\partial P}{\partial z}, \tag{2.23}$$

$$\frac{\partial Q}{\partial t} = \mathrm{G}_Q (N+O)Q\mathrm{e}^{\mathrm{K}z_Q} - \mathrm{D}_Q Q + \kappa\frac{\partial^2 Q}{\partial z^2}. \tag{2.24}$$

The boundary conditions are

$$\frac{\partial N}{\partial z} = \frac{\partial O}{\partial z} = \mathrm{W}_P P - \kappa\frac{\partial P}{\partial z} = \frac{\partial Q}{\partial z} = 0 \quad \text{at} \quad z = 0,$$

$$N = 1, \quad O = P = Q = 0 \quad \text{at} \quad z = -\infty.$$

Only phytoplankton P sinks, but the resulting surface depletion has an approximately equal impact on both species. Fig. 2.12 shows the solution for P, Q, and total nutrients ($N+O$) when the sinking rate, W_P, is 1 m day^{-1}, and all other parameter values are preserved from Fig. 2.10. The maximum concentration of P is reduced to 48% of its former value when sinking is included, while the maximum concentration of Q is reduced to 39% of its former value. The chlorophyll maximum in Fig. 2.12 is the result of two distinct mechanisms; in addition to the stratification of species with different chlorophyll contents, discussed above, sinking of P gives rise to a DBM, shown in Fig. 2.12 as the thin solid line, which contributes to the prominence of the DCM.

Because it enhances exchange between different depths, one would expect sinking of phytoplankton to increase the *f*-ratio, that is, the relative amount of new production. Fig. 2.13 shows the solution to the NOPQ model with sinking of phytoplankton P, and the rates of new and regenerated production. The parameter values are the same as those in Figs. 2.11 and 2.12. Comparing Fig. 2.13(b) with Fig. 2.11(b), one can see that while the introduction of sinking has caused a reduction in the level of absolute primary production, new production makes up approximately twice as large a fraction of the total—the *f*-ratio has doubled.

2.8 Discussion

Our approach to plankton modeling is to regard nitrogen conservation as an explicit constraint. As primary production in most areas of the oligotrophic ocean is generally considered to be nitrogen limited, biological activity there can be regarded

as a competition among species for available nitrogen. Nitrogen may flow between compartments, or from one location to another, but it is not created or destroyed.

The depletion of nitrogen from the upper regions of the euphotic zone caused by sinking of organic matter provides a mechanism for the formation of a DBM in phytoplankton. In a one-dimensional, steady-state, nitrogen-conserving model of nonmotile phytoplankton, sinking may provide the only reasonable such mechanism. Many authors, dating back to Riley et al. (1949) have included sinking of phytoplankton in their models. However, we suspect that the importance of sinking in determining the distribution of nitrogen with depth has often been under-appreciated. Our models with sinking of nitrogen in various forms demonstrate that the important factor in depleting the euphotic zone of nitrogen (and therefore in forming a DBM) is just that nitrogen sinks. The form of the sinking material, whether phytoplankton, detritus, or any other form, is far less important in determining the vertical structure of the ecosystem. Several authors, notably Steele and Yentsch (1960), have pointed out that a depth-dependent sinking rate can lead to vertical structure in the phytoplankton profile. While one would expect an accumulation of phytoplankton where there is a convergence in sinking rate, we emphasize that the primary importance of sinking in the formation of a deep phytoplankton maximum lies not in its changes with depth, but in its nitrogen-depleting effect on the surface layer.

Models that fail to satisfy the fundamental constraint of nitrogen conservation can produce misleading results. As an example, the model of Varela et al. (1992, 1994), patterned after that of Jamart et al. (1977), does not conserve

nitrogen. Though their model does not have an explicit zooplankton compartment, they do include terms representing zooplankton grazing, which removes phytoplankton from the system, and zooplankton excretion, which adds ammonia. As grazing is very much larger than excretion, there is a net removal of nitrogen. At steady state, this loss is balanced by upward diffusion of nitrate from an infinite reservoir at the bottom of the model domain. It is unlikely that Varela et al. (1994) would have written that "sinking [was] not needed to reproduce the main DCM features" had they not achieved surface nitrogen depletion by allowing nitrogen to vanish from the euphotic zone.

A parameter study of our NP model with sinking provides information about how parameter values influence the size, shape, and depth of the deep maximum. Perhaps counterintuitively, the value of the phytoplankton growth rate, G, has no influence on the magnitude or shape of the deep maximum, but only on its depth. The depth of the maximum is determined by the growth rate, the sinking rate, and diffusivity, but the dependence is strongest on growth rate. Thus, the magnitude of the maximum is a function of diffusivity and sinking rate, while its depth is largely determined by the growth rate.

Changes in diffusivity with depth, whether these changes occur shallower or deeper than the DBM, do not have a strong effect on its location or magnitude in our NP model. Thus the model does not support the hypothesis, suggested, e.g., by Mann and Lazier (1996), that vertical variation in diffusivity is instrumental in determining the depth of the DBM.

In our models, some factors were found to be of secondary importance in determining the form of the phytoplankton profile. The basic behavior of this profile is captured in a two-compartment model subject to removal of surface nitrogen by sinking. Including additional compartments, such as detritus and zooplankton, does not profoundly affect phytoplankton concentration. The growth rate terms in the models presented here are simple functions of nutrient concentration and light intensity because more complicated forms, when included, were found to introduce only slight changes to the solutions obtained with the simpler forms.

As chlorophyll-to-biomass ratio may change with depth for a number of reasons, a DCM may be caused by a wider variety of mechanisms than a DBM. One such reason is that chlorophyll content varies between species, and species composition is a function of depth. Even though it is not a DBM, a DCM formed in this way may be of ecological interest as the dominant region of new production. That the deep-living species making up the DCM may carry out most of the new production has been suggested before (Venrick, 1993); our NOPQ model illustrates one way this pattern could come about. When sinking of phytoplankton is included in the NOPQ model, a DBM forms, and the f-ratio increases.

The processes highlighted in our models suggest measurements which could test the validity of the models. If, for example, a DBM arises due to surface nitrogen depletion caused by sinking of phytoplankton or detritus, then a census of total nitrogen, including all the particulate forms and dissolved organic and inorganic nitrogen, should reveal this depletion. The sinking flux of nitrogen in organic materials, which could possibly be measured with sediment traps, should be

sufficient to maintain a surface depletion against the upward eddy diffusion of nitrate, which could be inferred from the nitrate profile coupled with eddy diffusivity estimates from dissipation measurements. If a DCM is observed, but measurements determine that surface nitrogen is not depleted, the sinking mechanism is ruled out, and the DCM is likely caused by variation in the chlorophyll-to-nitrogen ratio. In that case, if the 'NPQ' process is important in determining this ratio, the differences between species in chlorophyll content and in the variation of growth rates with light level should be verifiable.

Appendix (Chapter 2)

We prove that a stable solution to our first model (Eqs. (2.1) and (2.2)) exists.

$$\frac{\partial N}{\partial t} = -\mu(N, P, z) + \frac{\partial}{\partial z}\left(\kappa \frac{\partial N}{\partial z}\right), \tag{1}$$

$$\frac{\partial P}{\partial t} = \mu(N, P, z) + \frac{\partial}{\partial z}\left(\kappa \frac{\partial P}{\partial z}\right), \tag{2}$$

Boundary conditions:

$$\frac{\partial N}{\partial z} = \frac{\partial P}{\partial z} = 0 \quad \text{at} \quad z = 0,$$

$$N = 1, \quad P = 0 \quad \text{at} \quad z = -\infty.$$

We know that $N + P = 1$, so we can eliminate P from the system:

$$P = 1 - N \Rightarrow \frac{\partial N}{\partial t} = -\mu(N, z) + \frac{\partial}{\partial z}\left(\kappa \frac{\partial N}{\partial z}\right),$$

$$\frac{\partial V}{\partial N} \equiv \mu(N, z) \Rightarrow \frac{\partial N}{\partial t} = -\frac{\partial V}{\partial N} + \frac{\partial}{\partial z}\left(\kappa \frac{\partial N}{\partial z}\right).$$

V is determined by μ up to an arbitrary constant. Note that once this constant is chosen, since $N \in [1, 0]$, V is bounded for finite μ. Multiplying by $-\partial N / \partial t$ and integrating over z,

$$-\int_{-\infty}^{0}\left(\frac{\partial N}{\partial t}\right)^2 dz = \int_{-\infty}^{0}\left[\frac{\partial V}{\partial t} - \frac{\partial}{\partial z}\left(\kappa \frac{\partial N}{\partial z}\right)\frac{\partial N}{\partial t}\right]dz.$$

Integrating the second term on the right-hand side by parts and applying the BC's, this becomes

$$-\int_{-\infty}^{0}\left(\frac{\partial N}{\partial t}\right)^{2}dz = \frac{d}{dt}\int_{-\infty}^{0}\left[V+\frac{1}{2}\kappa\left(\frac{\partial N}{\partial z}\right)^{2}\right]dz.$$

As long as N is changing with time, the left-hand side is negative, and the integral on the right-hand side is decreasing. The second term in the integrand is positive, and V is bounded, so the integral on the right-hand side has a minimum value. N can only change until this minimum value has been reached, at which point a stable solution will have been attained.
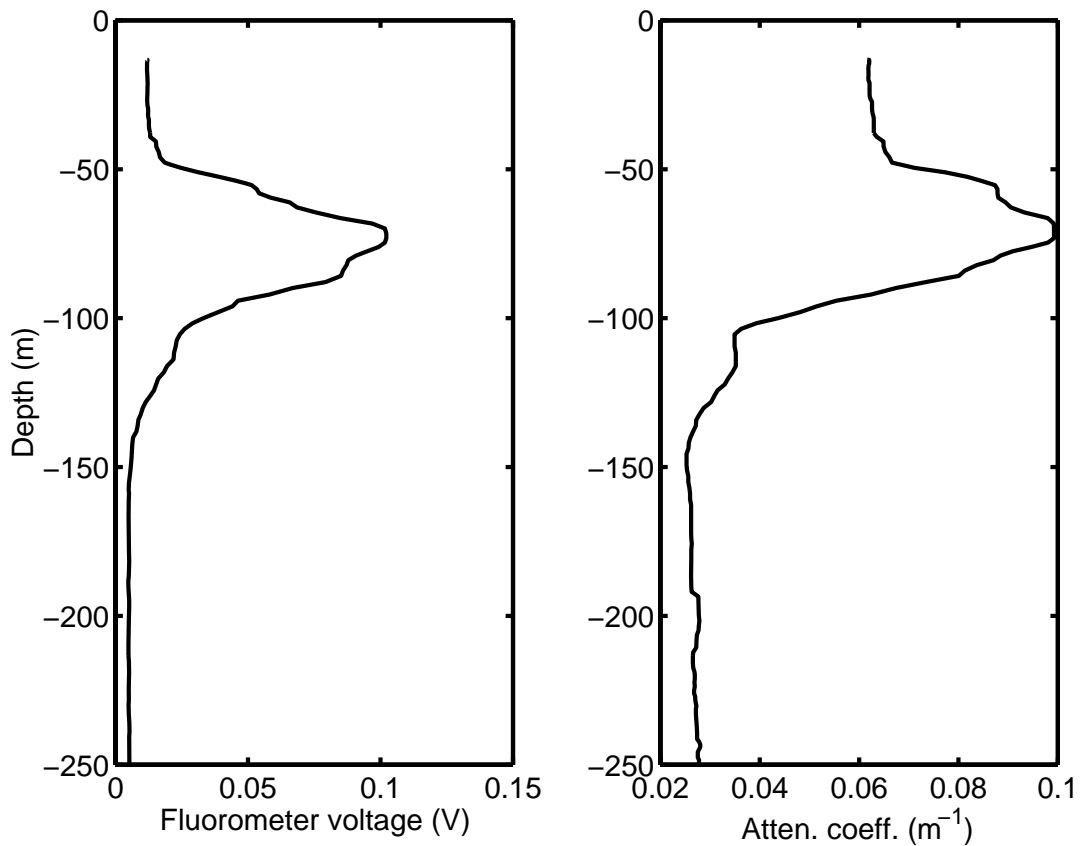
Figure 2.1. Vertical profiles of chlorophyll a fluorescence and beam attenuation coefficient of 660 nm light, a rough measure of POC. The component of attenuation due to absorption by water has been removed. The measurements were made on October 4, 2001, at 5.5° N, 95.4° W, as part of EPIC-2001.
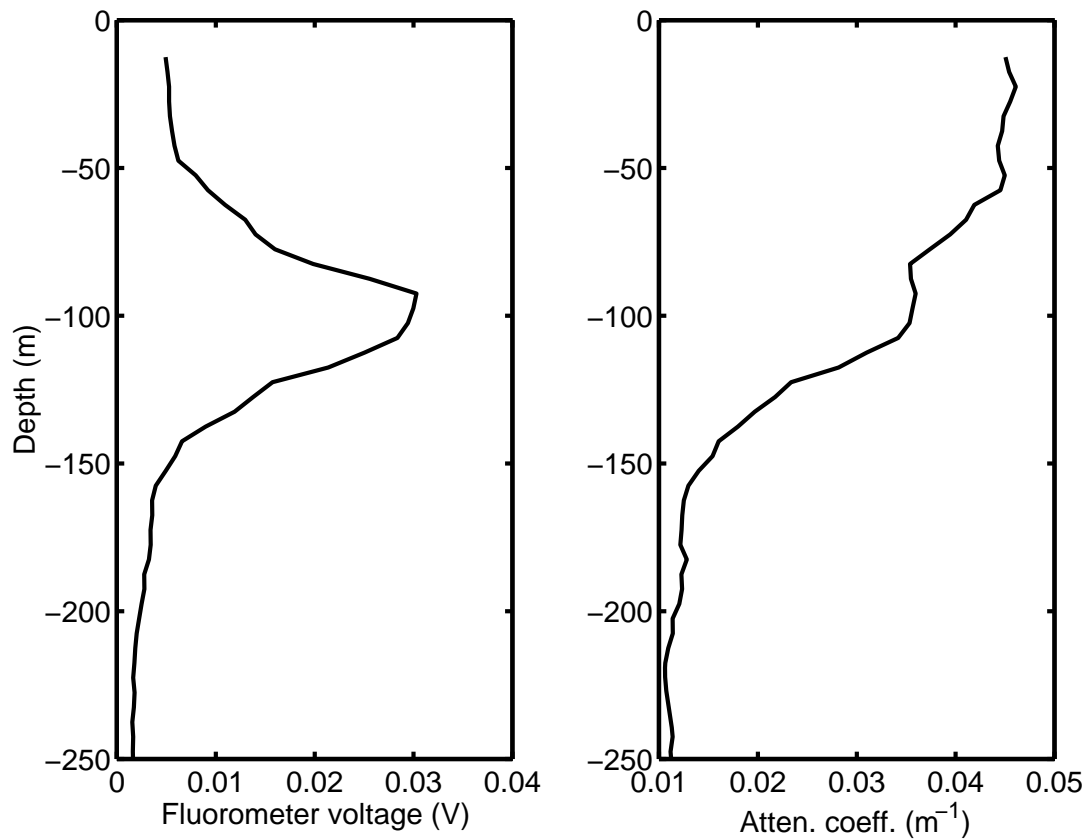
Figure 2.2. Vertical profiles of chlorophyll a fluorescence and beam attenuation coefficient. The data were obtained during the HOME 2002 experiment on October 15, 2002, at latitude 21° N, longitude 159° W.
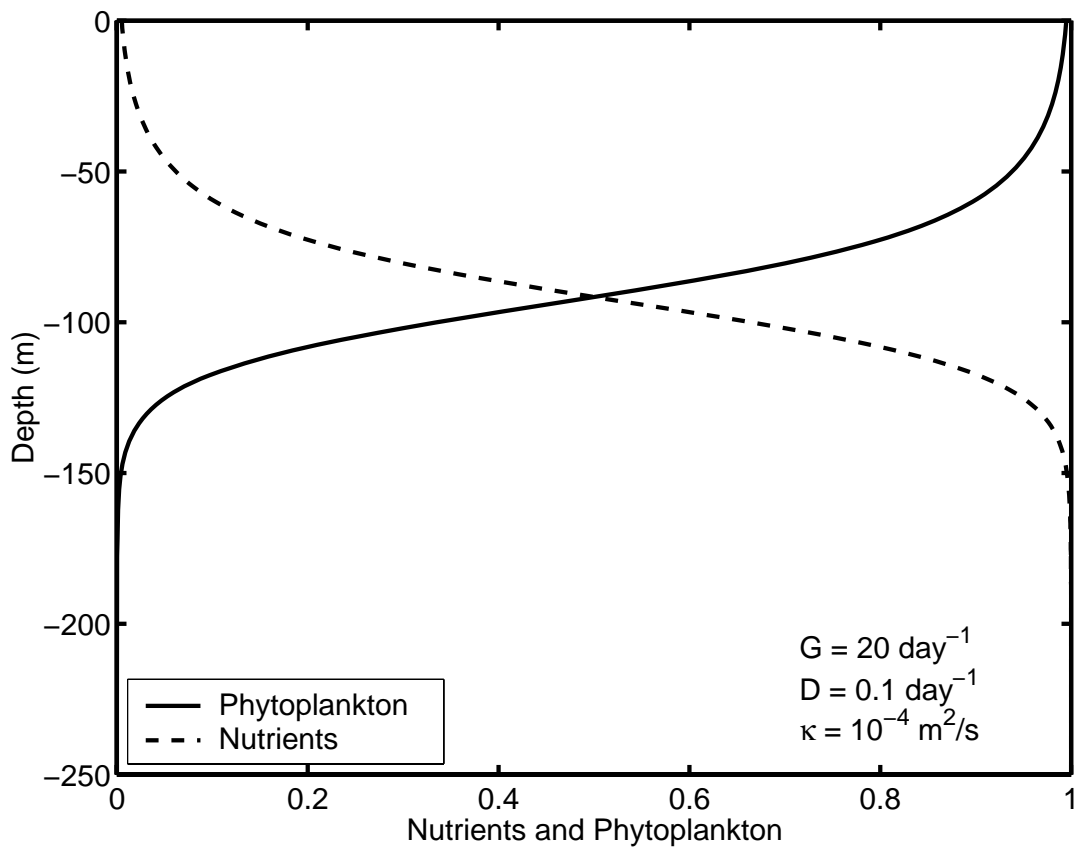
Figure 2.3. Solution to the NP model without sinking, Eqs. (2.4) and (2.5), for the parameter values shown. The profiles of nutrients (dashed) and phytoplankton are mirror images of each other.
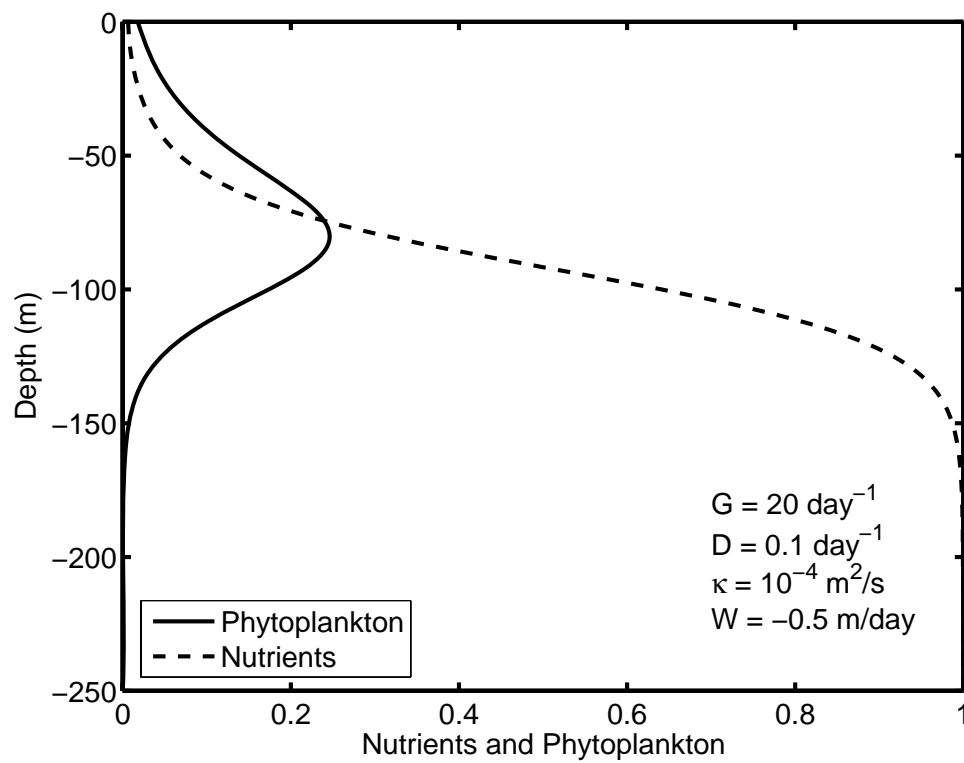
Figure 2.4. Solution to the NP model with sinking, Eqs. (2.6) and (2.7). Note the pronounced deep maximum in phytoplankton.
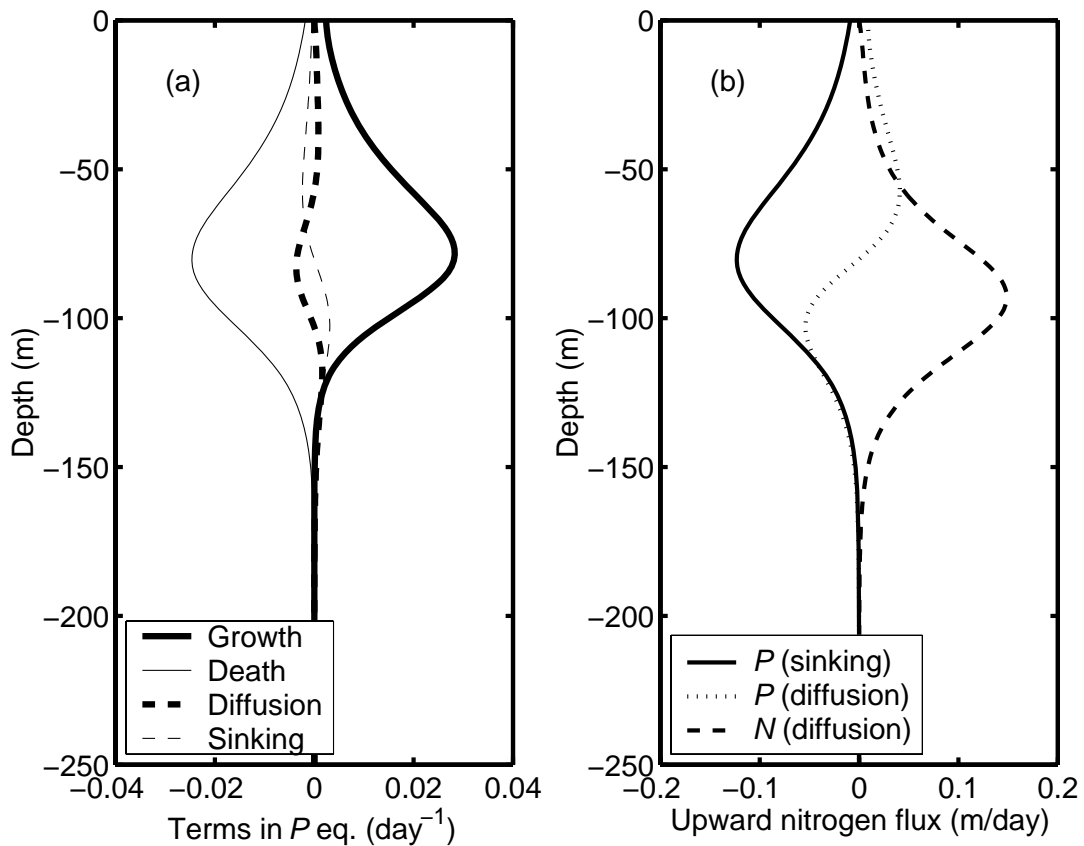
Figure 2.5. (a) The terms in Eq. (2.7) plotted versus depth for the model solution in Fig. 2.4. The four terms sum to zero, and the dominant balance in the euphotic zone is between growth and death. (b) Vertical flux balance for the same solution. Units on the horizontal axes reflect the fact that nitrogen concentration has been nondimensionalized.
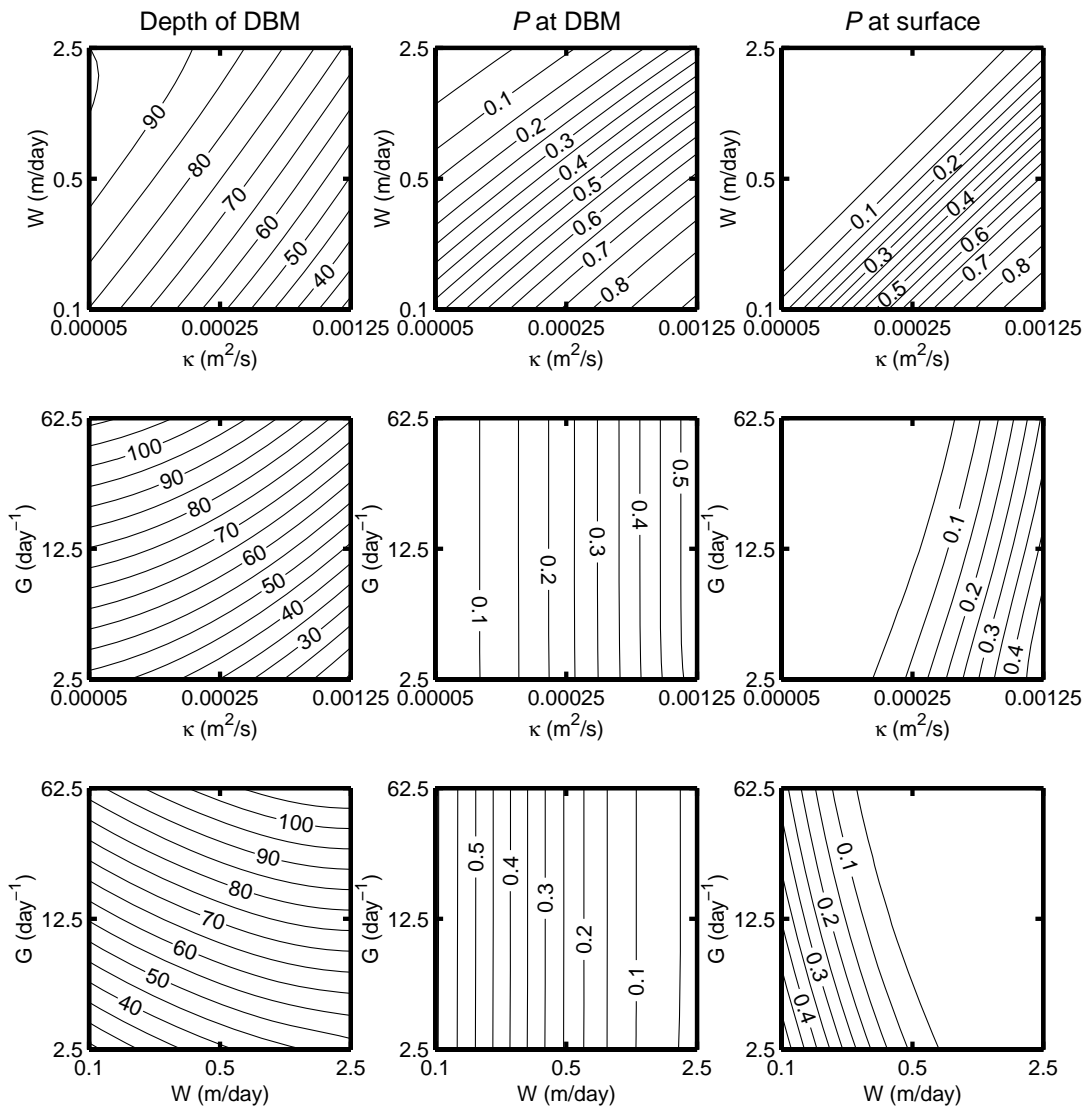
Figure 2.6. Behavior of the phytoplankton profile produced by the NP model with sinking (Eqs. (2.6) and (2.7)) as a function of position in G–κ–W parameter space. Depth of the DBM in meters is plotted in the left-hand column, phytoplankton concentration P at the maximum in the middle column, and phytoplankton concentration at the surface in the right-hand column. The dimensional parameter values corresponding to these figures are D = 0.1 day^{-1} and K = 0.05 m^{-1}. In the upper panels G is constant at 27 day^{-1}; in the middle panels W is constant at -1 m day^{-1}; and in the bottom panels, κ is constant at 10^{-4} m^2 s^{-1}. Note the logarithmic scaling of the axes.
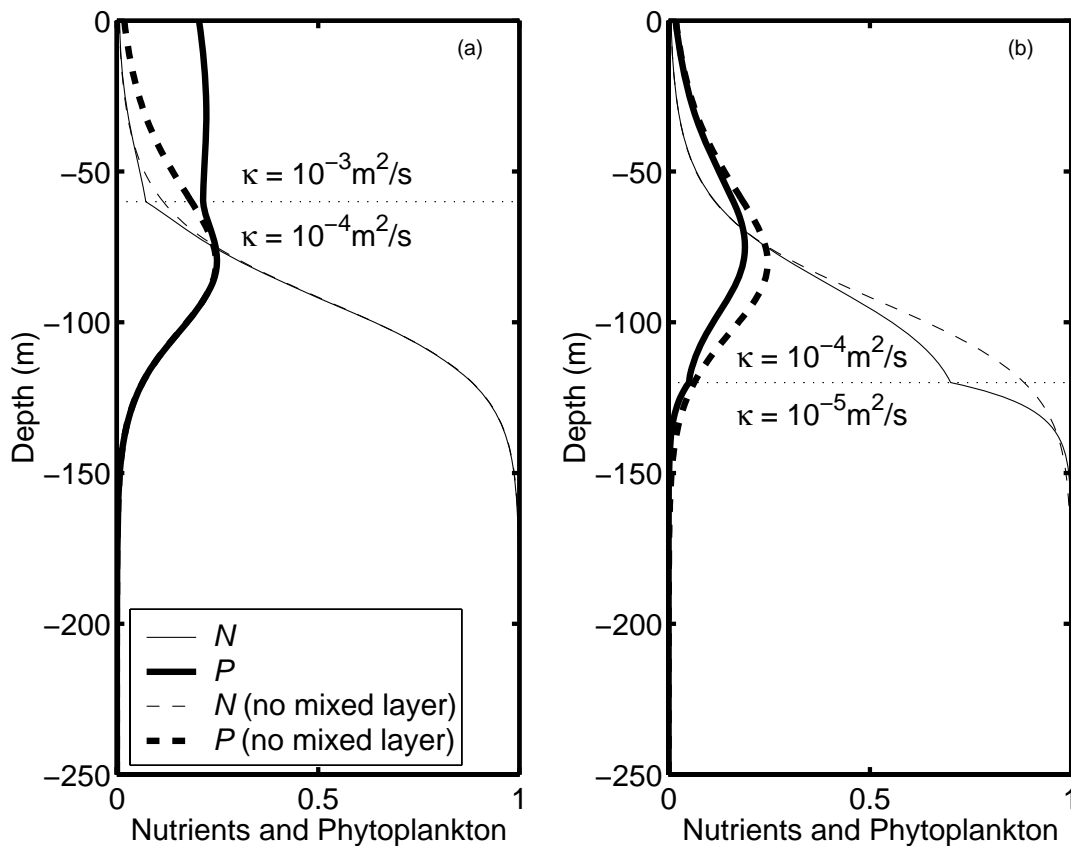
Figure 2.7. Solutions to the NP model with sinking (Eqs. (2.6) and (2.7)) with mixed layers in the form of step-function diffusivity profiles. The thick lines are phytoplankton and the thin lines are nutrients. In (a), κ decreases from 10^{-3} to 10^{-4} m^2 s^{-1} at a depth of 60 m; in (b), κ decreases from 10^{-4} to 10^{-5} m^2 s^{-1} at a depth of 120 m. The other parameters retain their values from Fig. 2.4, from which the solutions are re-plotted (dashed lines) for comparison.
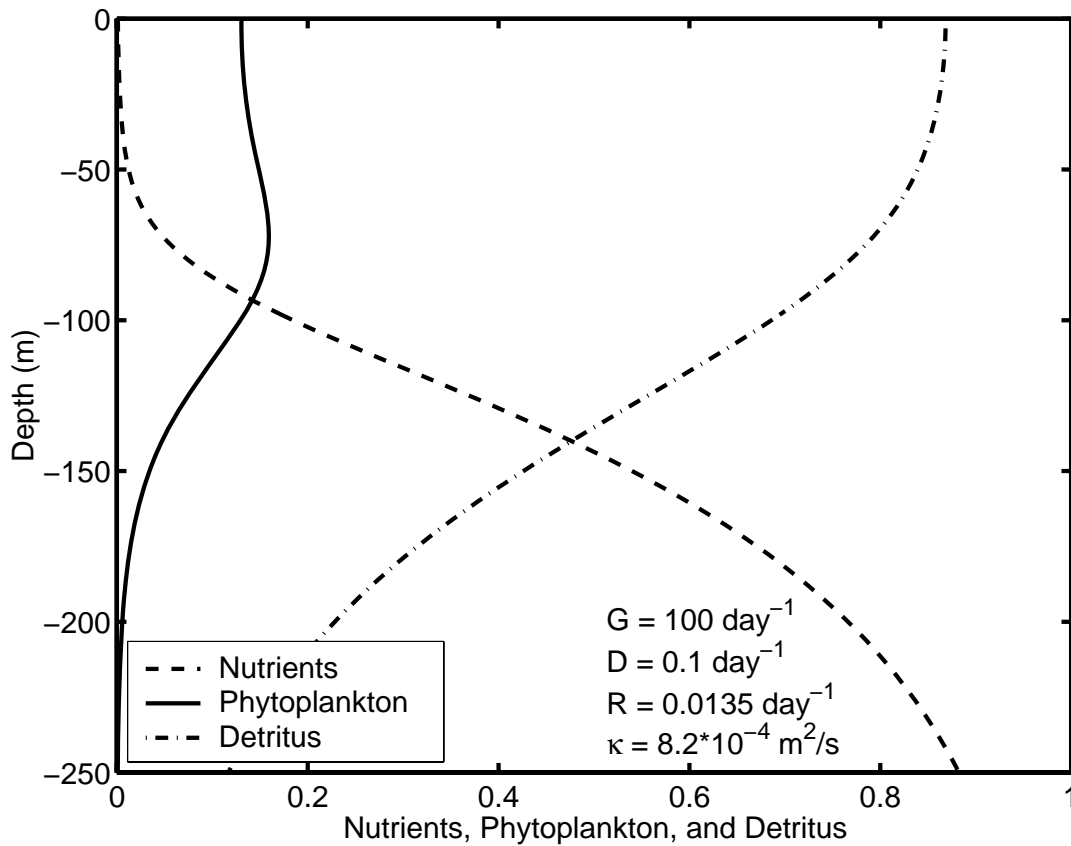
Figure 2.8. Solution to the NPT model, which includes a detrital compartment but no sinking (Eqs. (2.11), (2.12), and (2.13)). In terms of increase in phytoplankton concentration relative to the surface, this deep maximum is the largest in the region of parameter space described in the text.
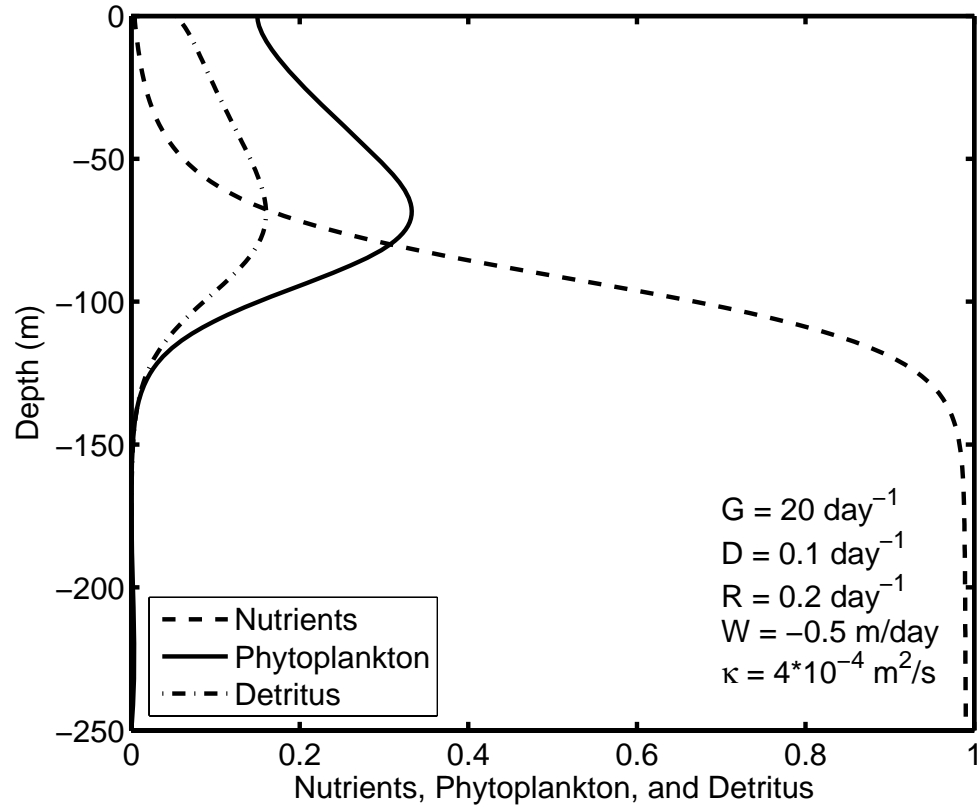
Figure 2.9. Solution to the three-compartment NPT model with sinking of detritus. The remineralization rate, R, is 0.2 day^{-1}, and the other parameters are the same as in Fig. 2.4, to which this figure may be compared.
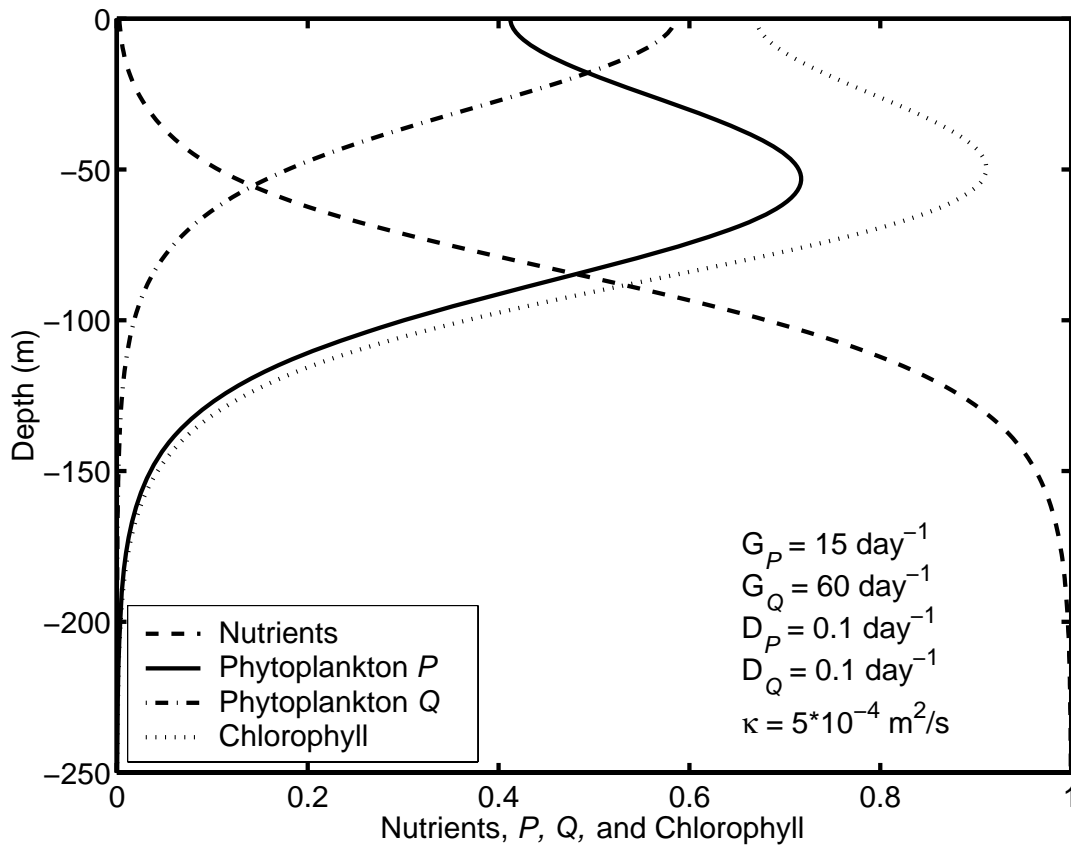
Figure 2.10. Solution to the two-phytoplankton NPQ model, Eqs. (2.14), (2.15), and (2.16). The length scale of decay of the growth rate of plankton P is twice that of plankton Q, and P has a chlorophyll-to-biomass ratio four times as large as that of Q. Chlorophyll concentration is plotted with arbitrary units.
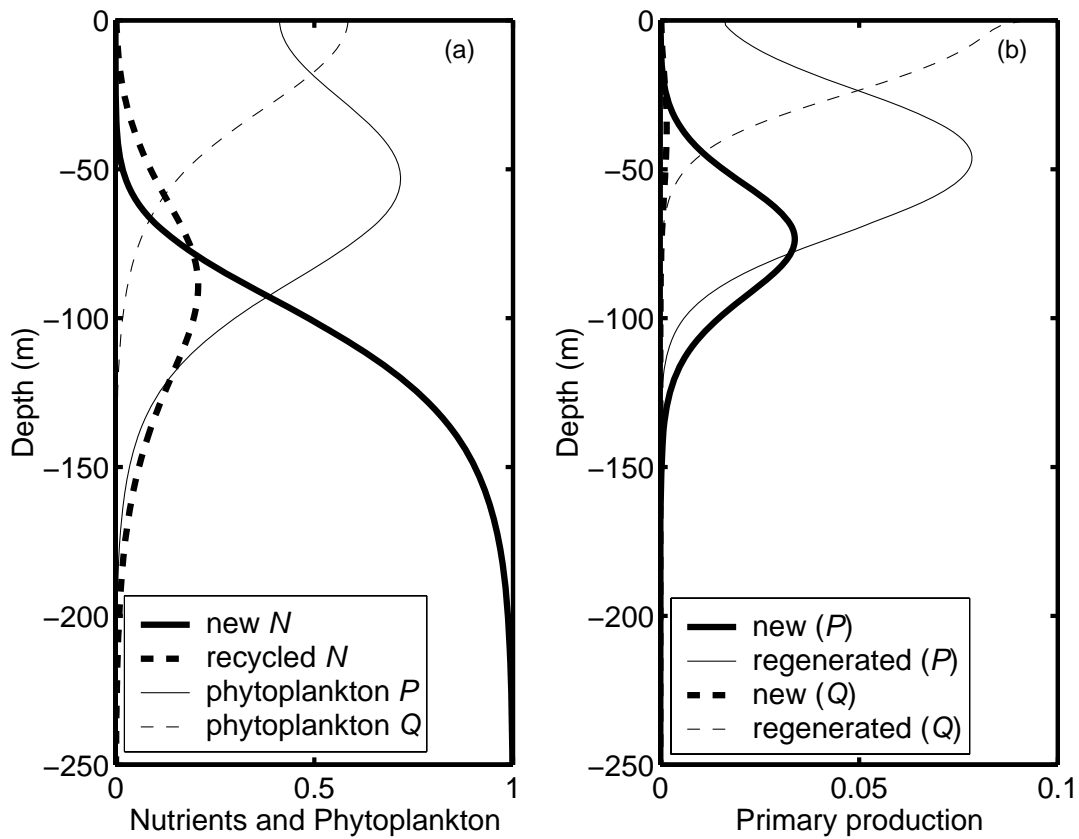
Figure 2.11. Results from the NOPQ model, Eqs. (2.17)–(2.20). The remineralization rate, R, is 0.1 day^{-1}, and all other parameter values are retained from Fig. 2.10. (a) Solutions to the model equations; thin lines: phytoplankton P (solid) and Q (dashed), thick lines: new (solid) and recycled (dashed) nutrients. (b) Primary production rates; thin lines: regenerated production by P (solid) and Q (dashed), thick lines: new production by P (solid) and Q (dashed). Units of primary production are nitrogen taken up per day as a fraction of the limiting nitrogen concentration at depth.
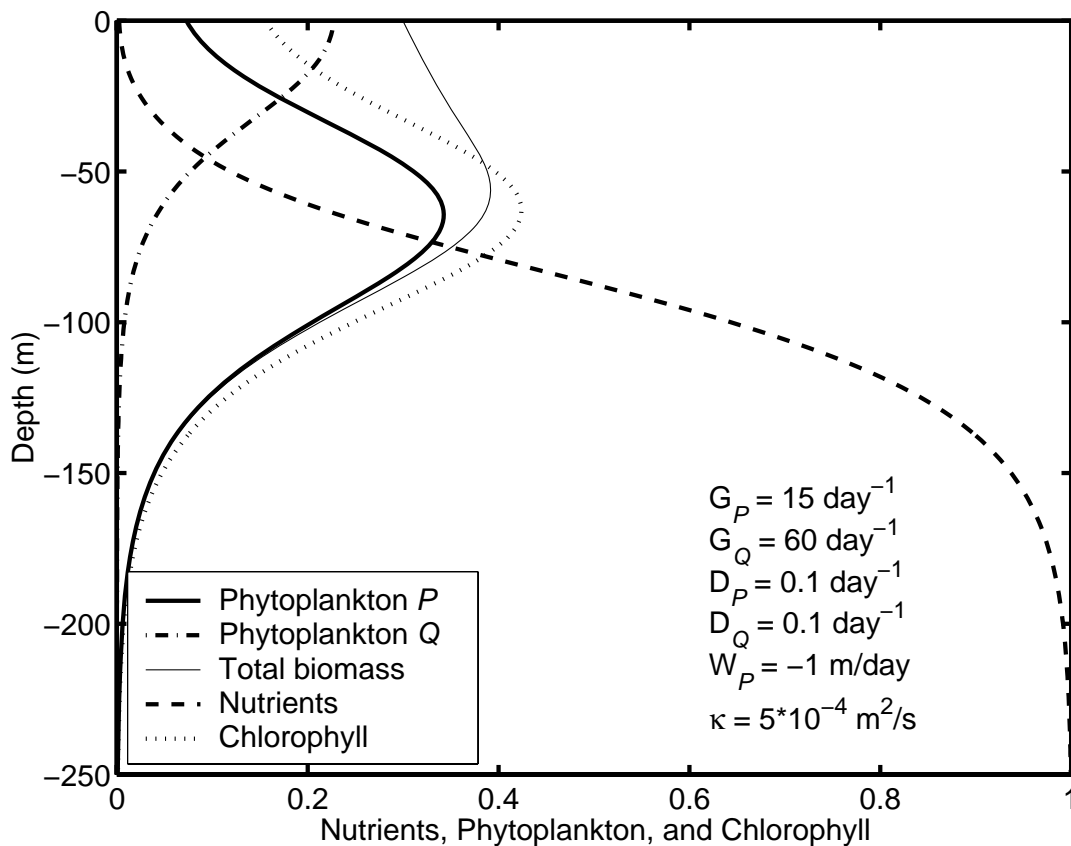
Figure 2.12. Solution to the NPQ model with sinking of phytoplankton P (Eqs. (2.21)–(2.24)). The total phytoplankton biomass, $P + Q$, is shown as the thin solid line, and total nutrient concentration is the thick dashed line. As in Fig. 2.10, phytoplankton P has four times the chlorophyll content of phytoplankton Q, and chlorophyll is plotted with arbitrary units.
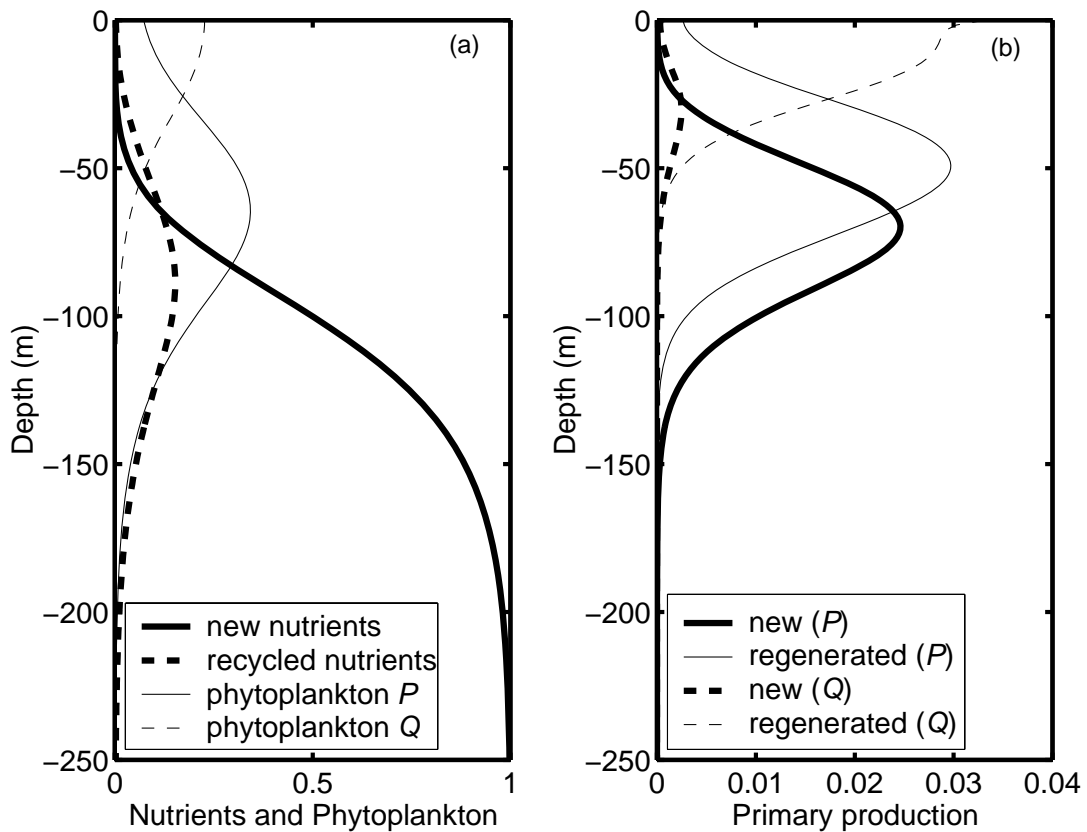
Figure 2.13. As in Fig. 2.11, but with phytoplankton P sinking at 1 m day^{-1}. Note the increase in the ratio of new to regenerated production as compared with Fig. 2.11.

Table 2.1. The region of parameter space for which numerical solutions to the NP model with sinking (Eqs. (2.6) and (2.7)) were obtained.

Parameter	Symbol	Value range	Unit
Attenuation coefficient	K	0.05	m
Death rate	D	0.1	day^{-1}
Growth rate	G	2.5 to 62.5	day^{-1}
Diffusivity	κ	$(5 \text{ to } 125) \times 10^{-5}$	$m^2 s^{-1}$
Sinking velocity	W	-2.5 to -0.1	$m\ day^{-1}$

Chapter 3

Horizontal Variability in Chlorophyll Fluorescence and Potential Temperature

Abstract of Chapter 3

Chlorophyll fluorescence and temperature were measured with a horizontal resolution of 4 meters on two isopycnals and two isobars along a 1000 km meridional transect in the eastern North Pacific. Probability density functions (PDFs) of the magnitude of fluctuations in temperature and fluorescence are compared at each of a large range of length scales. While they are nearly identical at larger scales, the shapes of the PDFs of fluorescence and temperature differ significantly at small scales (~1 km and less). This difference may indicate that at these scales, temperature and fluorescence distributions are controlled by distinct mechanisms. By comparing the phase of wavelet transforms of each of these two tracers, the tendency for temperature and fluorescence gradients to line up is investigated over a large range of spatial scales. At horizontal length scales of order 10 km and larger, the wavelet phase difference between temperature and fluorescence tends to be close to 0 or 180 degrees--that is, the gradients tend to align, either in phase or 180 degrees out of phase. At smaller scales, the distribution

of phase difference on isopycnals is uniform--there is no tendency for gradients to coincide. Simple stirring models demonstrate that the locations of enhanced gradients in all tracers would be expected to coincide where the strain has been greatest. However, the directions of enhanced gradients formed in this way may be either parallel or antiparallel, depending on initial conditions and on the direction of the strain. These analyses suggest the horizontal distributions of temperature and fluorescence at large scales were both governed by advective processes. At intermediate scales, of order 1-10 km, a renovating wave model suggests that gradient alignment could be destroyed by turbulent diffusion or by rapid local phytoplankton growth.

3.1 Introduction

The study of tracers in the ocean has a long history. Any seawater property that is advected with the flow is a tracer: temperature and salinity characteristics are useful for distinguishing large-scale water masses (e.g. Iselin, 1939), and on smaller scales as indicators of local flow patterns (Rudnick and Luyten, 1996). On basin scales, chlorofluorocarbons are measured to reveal ventilation pathways (e.g. Smethie and Fine, 2001); on smaller scales, dyes are added to the water to study dynamics (Ledwell et al., 1993). These tracers may all be described as conservative—away from formation regions where the tracer properties are set, there is minimal addition or removal of the tracer. Temperature and salinity are active, in the sense that they can affect the flow itself through their effect on density. The other tracers, having no such effect, are referred to as passive.

Chlorophyll may also be treated as a passive tracer, but in contrast to the conservative examples listed above, it is reactive: as phytoplankton grow and die, chlorophyll is continually created and destroyed. In the ocean interior where mixing to the surface is not occurring, no heat is transferred into or out of the water, so potential temperature is a conservative quantity. A comparison of the concurrent horizontal potential temperature and chlorophyll fields beneath the region of active surface mixing is then a comparison of conservative and reactive oceanic tracers. Differences in the statistics of the distributions of these tracers can offer insight into the different processes determining the structure of their fields (e.g. Martin 2003, Denman, 1976).

As phytoplankton are the primary producers of the ocean, their spatial distributions are of fundamental biological importance. Knowledge of these distributions is also important in the context of climate change, because of the role of phytoplankton in the global carbon cycle. For these reasons, an understanding of the mechanisms controlling the distribution of phytoplankton is an important goal. Plankton 'patchiness' has been observed by generations of oceanographers (Hardy, 1936; Cushing, 1961; Denman & Platt, 1976), and is thought to be an important factor in ecosystem stability (Steele, 1974). However, the causes of this patchiness are not well understood, and quantitative descriptions of phytoplankton distributions have often proven elusive, especially at very large and very small scales.

One difficulty lies simply in gathering information that simultaneously spans this entire range of scales. Such a large dynamic range requires continuous, high-resolution measurements over long distances. Satellite measurements of ocean color

provide information on chlorophyll concentration down to scales of order 1 kilometer, and satellite microwave measurements do the same for sea surface temperature. However, these measurements only capture variability in the surface layer of the ocean. To obtain information over a large dynamic range of scales from deeper layers, it is necessary to tow instruments that measure properties of the ocean interior in situ.

Perhaps the most easily (and therefore most often) measured biological property of this sort is chlorophyll fluorescence. When chlorophyll *a* molecules absorb visible light, they re-emit some of the energy as light in a wavelength band near 680 nm. Measurements of the intensity of the fluoresced light are widely used to estimate chlorophyll concentration, though the relationship between the two depends somewhat on the particular organisms involved, the extent of quenching, which depends on their light exposure history, and the degree of 'packaging'—essentially self-shading of chlorophyll molecules within an organism (Falkowski and Kiefer, 1985). As the chlorophyll-to-biomass ratio is highly variable (Pak et al., 1988; Cullen and Lewis, 1988), chlorophyll concentration alone is not an ideal indicator of phytoplankton biomass. However, much of the variation in this ratio may be explained by its dependence on light level and nutrient concentration (MacIntyre el al., 2002), both of which vary rapidly with depth but weakly with horizontal distance throughout most of the upper ocean. It is likely, then, that fluorescence is a better indicator of horizontal than of vertical structure in the phytoplankton concentration field.

When measuring small- to meso-scale horizontal structure of water properties in the ocean interior, large vertical gradients give rise to a subtler complication. When an instrument is towed at a constant depth, much of the variability it records may be due to vertical displacements of the vertical structure by internal waves. Vertical gradients in temperature and fluorescence are large in the thermocline and near the deep chlorophyll maximum, respectively, so internal waves contribute most strongly to the horizontal variability near these locations. In addition to this 'horizontal profiling of vertical structure,' changes occur along isopycnals, and when interpreting constant-depth measurements, it is difficult to distinguish between these two sources of horizontal variability. The along-isopycnal tows described in the following section avoid this difficulty. In addition, temperature and salinity cancel in their effects on density along isopycnals, and so lose their distinction as active tracers on these surfaces.

3.2 Spice Cruise

The primary objective of the 1997 Spice experiment (Rudnick and Ferrari, 1999) was to investigate the relationship between seawater temperature and salinity as a function of depth and horizontal length scale. However, the experiment also provided an excellent dataset for the study of horizontal variability in chlorophyll concentration, and of its relationship to physical properties of the water.

The instrumental platform used during the Spice cruise was a SeaSoar, which is a towed instrument whose depth is controlled by variable-pitch wings. Instruments on board included a Sea-Bird CTD and a WET Labs WetStar flow-

through fluorometer. Fluorometer excitation was centered at a wavelength of 455 nm, and emission measurements were centered at 685 nm. Though the relationship between fluorometer voltage and chlorophyll concentration is linear ($R^2 = 0.9987$ in a 14-sample laboratory calibration), we report fluorescence data as volts rather than converting to chlorophyll concentration because of poorly known species composition and flow rate in the field, both of which are important for an accurate calibration. A rough calibration for chlorophyll concentration in mg/m^3 in terms of fluorometer output in volts is $chl = 16(V - 0.13)$. Some of the fluorescence measurements discussed here were made at depths of 200 meters and deeper. The proportion of the fluorescence signal comprising live phytoplankton cells is unknown, but regardless of this proportion, the measurements provide information on the horizontal structure of the ecosystem.

The cruise track followed the 140°W meridian back and forth between 25° and 35°N in the eastern Pacific. The section was repeated five times altogether between January 24 and February 20, 1997. First, SeaSoar was towed southward along a sawtooth profile between 5 and 320 dbar, completing one dive approximately every 3 km. Then, using an automatic dynamic control system, it followed the 50-dbar isobar northward, and returned southward along the 200-dbar isobar. The last two tows tracked isopycnals by computing potential density in real time. The 24.8-kg/m^3 isopycnal[2] was followed northward until it outcropped near 32°N. The final southward tow tracked the 25.5 kg/m^3 isopycnal. The tracks of the

---

[2] Throughout this work, we refer to potential density in terms of its excess over 1000 kg/m^3.

four horizontal tows are plotted in white in Fig. 3.1, over a section of chlorophyll fluorescence from the sawtooth tow. The black lines are contours of potential density, also from the sawtooth tow. The isopycnals moved during the time interval between the sawtooth and isopycnal tows, so the heavy black lines do not exactly coincide with the jagged white lines. The horizontal resolution on the horizontal tows is 4 m, and the RMS deviations from the target surfaces were in the range of 0.4 dbar on the isobars, and 0.02 kg/m^3 on the isopycnals.

Along-isopycnal measurements are particularly well-suited to the present investigation because the short-term influence of internal waves is eliminated. Transport in the ocean occurs much more readily along isopycnals than across them, so in the context of mixing, a surface of constant potential density may be regarded as a single layer, whereas a surface of constant pressure (depth) slices through multiple layers. Changes observed along isobars are the result of a combination of isopycnal and diapycnal variability. Interpretation of these isobaric measurements is therefore less straightforward than that of the isopycnal measurements.

At the southern end of the transect (Fig. 3.1), the deep chlorophyll maximum lies just beneath the base of the mixed layer, while to the north, it is located within the mixed layer. Such a transition is a common wintertime feature in this region (see, e.g., Shulenberger and Reid, 1981). Summertime deep chlorophyll maxima typically lie well deeper than the mixed layer base. Various processes can contribute to the formation of the deep chlorophyll maximum, including increase with depth of mean pigment concentration within cells (Pak et al., 1988), and

nitrogen depletion of surface waters by sinking particles (Hodges and Rudnick, 2004).

The location of the deep chlorophyll maximum is important to the interpretation of the relationship between temperature and fluorescence on an isobar. Potential temperature typically decreases and potential density increases with depth throughout the water column, but the vertical gradient of chlorophyll concentration changes sign at the deep chlorophyll maximum. Thus, on isobars beneath the deep chlorophyll maximum, vertical movement brings cold, dense, low-chlorophyll water from below, and warm, light, high-chlorophyll water from above. On these surfaces, then, vertical displacements will create chlorophyll fluctuations that are in phase with fluctuations in temperature and out of phase with those in density. The chlorophyll fluctuations so produced on isobars shallower than the deep chlorophyll maximum will be out of phase with temperature and in phase with density. On isobars that cross the deep chlorophyll maximum, both relationships may be seen at a single depth. Such phase switching has been reported in the past by, for example, Denman (1976). Changes in growth rate and photoacclimation associated with vertical motions may act to cancel the alignment of chlorophyll and temperature fluctuations in some cases and to reinforce it in others.

Fig. 3.2 shows 500-meter averages of data from the 200-dbar isobar tow, including pressure as well as potential temperature, potential density, and chlorophyll fluorescence. The strong coherence of the latter three variables over most of the tow is easily explained—the dominant source of variance in each is local vertical displacement.

The 50-dbar tow stays within the mixed layer, so vertical gradients in physical properties are small throughout, and much of the measured variability comprises along-isopycnal fluctuations, in contrast to the deeper (200-dbar) isobar, on which the variability is predominantly diapycnal. The vertical gradient of temperature within the mixed layer, though small, is almost universally negative (decreasing with depth). The deep chlorophyll maximum lies deeper than 50 meters (Fig. 3.1), so along the 50-dbar tow, chlorophyll generally increases with depth. Slight changes due to vertical displacement of water would thus induce a negative correlation between temperature and chlorophyll. However, the strong correlation north of 32° N is positive (Fig. 3.3), and so cannot be attributed directly to vertical motions. The observed behavior can thus only be caused by a process that produces along-isopycnal changes.

Phase switching between potential temperature and chlorophyll fluorescence is evident along the 25.5 kg/m^3 isopycnal (Fig. 3.4). Throughout the southern three-fourths of the tow, the two variables vary in phase with each other, while in the northern fourth (approximately the same region where temperature and fluorescence were *in phase* on the shallower 50-dbar isobar), they are negatively correlated (out of phase).

On isopycnals, vertical motions cannot directly produce correlation between tracers, much less phase-switching behavior, because, unlike isobars, isopycnals move vertically with the water as it is displaced by internal waves. Within the euphotic zone, vertical motions can have an indirect effect on chlorophyll concentration via the biological response to the resulting changes in irradiance. This

mechanism is the probable cause of the correlation between pressure and fluorescence in the southern half of the 24.8 kg/m^3 isopycnal tow (Fig. 3.5): as the isopycnal is displaced toward the surface, the increased light stimulates phytoplankton growth. Apparently the timescale of this growth is shorter than that associated with the heaving of the isopycnal. Note that physical-biological interactions of this sort are an example of the influence of the non-conservative nature of chlorophyll on its distribution, whereas the structure observed on, e.g., the 200 dbar isobar can be understood by treating chlorophyll as if it were conservative.

For most of the length of the 25.5 kg/m^3 isopycnal tow (Fig. 3.4), the isopycnal depth was near 200 m, where little phytoplankton growth would be expected. It is not surprising, then, that the pressure and fluorescence records bear little resemblance. At the northern end of the tow, the isopycnal shoals, and there is some tendency for higher fluorescence values to coincide with shallower depths, suggesting that, as on the 24.8 kg/m^3 isopycnal, uplift has stimulated growth.

However, on the 25.5 kg/m^3 isopycnal the relationship between temperature and fluorescence is stronger, even in the shallow northern region, than that between pressure and fluorescence. South of 32° 42′ N, the isopycnal lies deeper than 160 meters, while to the north of this point, the isopycnal is shallower than 160 meters. Taking only the data from this latter segment of the tow, both pressure and temperature vary approximately linearly with fluorescence. The linear relationship is tighter for temperature, which has a coefficient of determination of $R^2 = 0.76$, compared to $R^2 = 0.57$ in the case of pressure. The implication is that the process producing correlation between temperature and fluorescence may be more important

on this isopycnal than the biological response to isopycnal uplift, even in the shallow segment of the tow. The immunity of along-isopycnal measurements to 'contamination' by vertical structure necessitates an alternate explanation for the observed correlation between temperature and fluorescence on the isopycnal.

Stirring of large-scale gradients provides a likely explanation for both the behavior observed on the isopycnal and the occurrence of temperature-fluorescence correlation of the 'wrong' sign on the isobars. As a tracer is advected by flow, filaments form. A blob of tracer is drawn out in a long tendril, stretching along one dimension as it contracts along another. Any initial gradient in tracer concentration in the direction of this contraction is amplified as the fluid particles move closer together. When two initially distant fluid particles in a smooth tracer field approach each other, a strong concentration gradient typically develops along the line connecting them. The sign of this gradient (that is, increasing or decreasing) depends on the initial field. Where the signs of the gradients of two tracers in the direction of contraction are the same, in-phase behavior develops. Where the signs of the gradients are opposite, the result is out-of-phase behavior. Thus two initially unrelated tracers, when advected by a flow, would be expected over time to develop enhanced gradients in the same locations and along the same directions, but not necessarily of the same signs. This stirring-induced gradient alignment provides an attractive explanation of the correlation, positive in some locations and negative in others, between potential temperature and fluorescence on the 25.5 kg/m^3 isopycnal (Fig. 3.4). It is likely also the mechanism behind the in-phase relationship observed at 50 dbar (Fig. 3.3).

The strong front north of 29° N is clearly visible in both temperature and fluorescence from the 24.8 kg/m^3 isopycnal tow (Fig. 3.5). This feature, like the structure on the deeper isopycnal, is probably the result of a high degree of strain, though interpretation is complicated because in the region of the front the isopycnal is crossing the mixed layer base.

We examine the distribution of potential temperature and chlorophyll fluorescence on the four horizontal tows in Section 3.3. The range of length scales on which gradient alignment between these two tracers was observed is the subject of Section 3.4. In Section 3.5 we use simple stirring models to demonstrate gradient alignment and investigate the scales on which it occurs.

3.3 Scales of Variability

A basic property of any scalar function of position is the way in which the variance is distributed among spatial scales. This information is presented (Fig. 3.6) in spectra of the measurements of potential temperature (blue lines) and fluorescence (black lines) along each of the isobar and isopycnal tows. At scales greater than a kilometer, both potential temperature and fluorescence have spectral slopes of approximately –2 on all four tows. Given the tow speed of about eight knots, the diurnal frequency corresponds roughly to 3×10^{-6} cycles per meter; the lack of peaks at this scale in the fluorescence spectra indicates that the light cycle had a minimal impact on fluorescence measurements. However, on the isopycnal

tows, there are large spectral peaks in potential temperature at scales of a few hundred meters. These are artifacts of the flight path.

The SeaSoar cannot follow isobars or isopycnals perfectly, and the deviation distance from the desired depth is greater on isopycnals than on isobars. During the 25.5 kg/m^3 isopycnal tow, the RMS deviation in density was 0.015 kg/m^3, corresponding to a little over a meter in depth. The RMS depth deviation during the 200-dbar isobar tow was 35 cm, only one third as much. During the isopycnal tows, the SeaSoar tended to fluctuate around the target density surface on horizontal scales of 100 to 400 meters (Fig. 3.6, green lines), and this broad spectral peak in density variability is reflected strongly in the spectra of potential temperature (Fig. 3.6, dashed blue lines). We can get closer to the true temperature on the isopycnal by using the observed difference between the desired density and the measured density ($\Delta\sigma_\theta$) and the local rate of change of potential temperature with potential density ($\partial\theta/\partial\sigma_\theta$) to correct the measured temperatures. The 24 Hz raw data is averaged in time to 1 Hz and the record is broken into 100-second (400-meter) overlapping intervals. $\partial\theta/\partial\sigma_\theta$ is computed for each interval by a least-squares fit to the temperature and density data. The corrected potential temperature is then given by $\theta_{true} = \theta - \Delta\sigma_\theta(\partial\theta/\partial\sigma_\theta)$. The spectra of the corrected potential temperature (solid blue lines in Fig. 3.6) show the influence of the density variability much less strongly. The correction changes the spectra of fluorescence more subtly (Fig. 3.6, middle panel). On the isobars, where excursions from the target depth were smaller, the corrections to temperature and fluorescence make

little difference (Fig. 3.6, bottom panel); however, for uniformity we henceforth use the corrected potential temperature and fluorescence in all analyses.

The spectra of fluorescence all whiten at a similar level (Fig. 3.6). This level represents an electronic noise floor inherent in the fluorometer as it was configured, and the spectral whitening is an indication of a low signal-to-noise ratio. We cannot obtain trustworthy information about the distribution of fluorescence on a scale shorter than that where spectral whitening first appears. On the shallower tows, this cutoff scale is on the order of 100 meters; on the deep tows, where chlorophyll is less abundant, making the signal weaker, it is on the order of a kilometer.

The biological and physical dynamics are more complicated on the shallower tows. While the chlorophyll encountered on the 200-dbar and 25.5 kg/m^3 tows, both within the thermocline and below the euphotic zone, was presumably contained in organisms that were dead, dying, or dormant, the remaining two tows were made through a biologically active region. For much of its length, the 24.8 kg/m^3 isopycnal lies near both the mixed layer base and the deep chlorophyll maximum, so vertical gradients in both physical properties and chlorophyll are at their most variable. Figure 3.7 shows the section of the 24.8 kg/m^3 isopycnal tow between latitudes 29° 18′ and 29° 36′ N, where the tuning of the flight control algorithm was improperly matched to the local stratification, causing especially large (see Fig. 3.2) unintentional oscillations about the isopycnal. The oscillations spanned the deep chlorophyll maximum, revealing that, even over small ranges of density, the density-fluorescence relationship can be strongly nonlinear. Small deviations from the isopycnal therefore may lead to large and unpredictable changes

in the measured seawater properties, making the correction for deviation from the isopycnal less reliable. On scales of a few kilometers and larger, however, these fluctuations, like those due to instrumental noise, average out and are not a concern. At smaller scales than these, caution must be used in interpreting results from the 24.8 kg/m^3 isopycnal tow, particularly those involving fluorescence.

The spectra in Fig. 3.6 provide a description of the total amount of variance in potential temperature and fluorescence as a function of spatial scale, but no information on how that variance is distributed in space. The variability at a given scale might be relatively evenly distributed throughout the entire record, or it might consist of a few intermittent, highly energetic events, or something in between. In order to distinguish among these possible distributions, we use a wavelet transform. Like the coefficients of the Fourier transform from which the spectra above are computed, the coefficients of a wavelet transform reveal how variance is distributed among the various spatial scales, but unlike the Fourier transform, each coefficient is associated with a particular spatial location, and depends only on the portion of the record in the vicinity of that location. Whereas the sines and cosines of the Fourier transform have well defined wavenumbers but extend forever in space, the analyzing functions of a wavelet transform are compact in both wavenumber and space. The wavelet transform, then, is defined as:

$$w(s, x_0) = \int_{-\infty}^{\infty} d(x)\psi_{s,x_0}^{*}(x)dx.$$

Here, location is represented by the coordinate x, and the data by $d(x)$; the analyzing function ψ is called a wavelet, and the wavelet transform, w, is just the convolution

of the data with the wavelet (see, e.g., Daubechies, 1992). We use a Morlet wavelet, which varies sinusoidally inside a Gaussian envelope. The "mother" Morlet wavelet is $\psi(x) = e^{2\pi i m x - x^2/2}$, where m controls the number of oscillations inside the envelope. A common choice is $m=1$, and we use this value for all our wavelet calculations. The family of wavelets is derived from this mother wavelet by translation and dilation. The wavelet for a general location and wavenumber is

$$\psi_{s,x_0}(x) = |s|^{-\frac{1}{2}} \psi\left(\frac{x - x_0}{s}\right).$$

Changing s dilates and contracts the wavelet, thus specifying the wavenumber, and x_0 sets the spatial location of the center of the wavelet. The factor $|s|^{-\frac{1}{2}}$ ensures that all wavelets have identical energy. The coefficient $w(s, x_0)$ computed from the wavelet $\psi_{s,x_0}(x)$ indicates the amount of variability at scales near s and locations near x_0.

For each of the four horizontal SeaSoar tows, we form probability density functions (PDFs) of the magnitude of fluctuations in potential temperature and fluorescence (Figs. 3.8-3.11). Each PDF is a normalized histogram of the real parts of all the wavelet coefficients w corresponding to a single scale s. The choice of whether to use the real or imaginary part of the wavelet coefficients to form the PDFs is arbitrary, as the same information is contained in both. However, the wavelet phase, which is computed from both real and imaginary parts, will be useful in the following section where we investigate gradient alignment. Each pair of PDFs corresponds to a different wavelength of variability, ranging from 10 meters,

which is approaching the Nyquist wavelength (twice the distance between sampling points, and thus the shortest resolvable wavelength), to 10 kilometers, above which there are too few independent realizations to yield a PDF with smooth, well-defined tails. The shape of a PDF at a given spatial scale indicates the frequency with which fluctuations of various magnitudes occur on that scale. The abscissa is standard deviations of the real parts of all the wavelet coefficients that form each PDF, so that the PDFs of fluctuations on small and large scales have equal apparent widths despite the larger fluctuations that occur on larger scales.

Many studies have attempted to determine the scales at which the horizontal distribution of chlorophyll is controlled by physical mechanisms by a comparison of the spectral slope of chlorophyll fluorescence with that of conservative tracers. Similar spectral slopes are cited as evidence of control by similar mechanisms. Martin (2003) provides a recent review of such studies. PDF shape, in combination with spectral information, provides a more stringent test of statistical equivalence of distinct tracers than does spectral slope alone, and this is our motivation for examining the scale-specific PDFs of fluctuations in temperature and fluorescence.

At the smallest scales, the PDFs of fluorescence fluctuations are drawn in dashed lines because their Gaussian shape is the result of instrumental noise. The temperature PDFs at these small scales have a stretched exponential shape, familiar from distributions of small-scale scalar difference of a passive scalar in a turbulent field (e.g. Warhaft, 2000). On the largest scales, the PDFs of potential temperature and fluorescence fluctuations appear to be converging toward a common exponential shape.

The potential temperature PDFs for the 200-dbar isobar tow (Fig. 3.8) have a more rounded central peak than those for the 25.5 kg/m^3 isopycnal (Fig. 3.10), indicating less intermittency for small-magnitude events on the isobar. The difference, though present at all scales, is most noticeable in a length scale range near 1 kilometer (see the 1280-meter PDFs). The roundness of the temperature PDFs on the isobar is consistent with variability driven largely by internal waves having a Gaussian-like distribution (see Briscoe (1977) for a discussion of the Gaussianity of internal wave vertical displacement). Note also that both the potential temperature and the fluorescence PDFs on the shallower tows (the 50-dbar isobar and the 24.8 kg/m^3 isopycnal—Figs. 9 and 11 respectively) tend to be more peaked than those on the deep tows, pointing to a high degree of intermittency (i.e. a relatively small number of isolated fronts) within the mixed layer.

Of the four horizontal tows, the 50-dbar isobar tow provides the least contaminated view of small-scale variability in fluorescence. On the deep tows, instrumental noise competes with the weak fluorescence signal and obscures the true shape of the small-scale fluorescence PDFs. On the 24.8 kg/m^3 isopycnal tow, the measured small-scale variability in fluorescence is due partly to small deviations from the target isopycnal in regions where the vertical gradient of chlorophyll concentration is strong. On the 50-dbar tow, which is comparatively free of both these complications, the PDFs of fluorescence on scales below a kilometer but above 100 meters (where the effects of instrumental noise become important), are rounder than those of temperature (Fig. 3.9). Temperature appears to be more intermittent than fluorescence on the 50 dbar tow.

To summarize, then, at large scales the PDFs of fluctuations in temperature and fluorescence are similar: by a scale of 10 km (the bottom pair of PDFs in Figs. 3.8-3.11) the temperature and fluorescence PDFs are essentially identical. At the smallest scales, the true shape of the fluorescence PDFs is obscured by instrumental noise, but at intermediate scales, there appear to be meaningful differences between the shapes of temperature and fluorescence PDFs, particularly within the mixed layer. At these scales, then, different processes may be important in setting the temperature and fluorescence distributions.

One possible reason for the enhanced intermittency of temperature relative to fluorescence observed in the PDFs from the 50 dbar isobar is vertical mixing coupled with gravity-driven slumping of horizontal density gradients in the mixed layer (e.g. Ferrari and Rudnick, 2000). In a hypothetical mixed layer with initially random horizontal distributions of temperature and salinity, many of the small-scale horizontal fluctuations in temperature would be smoothed by vertical mixing as warm water from one side of a front flowed over cool, denser water from the other. Only those horizontal temperature fluctuations that were density-compensated by corresponding salinity fluctuations would persist. The horizontal distribution of temperature could in this way become more intermittent while that of chlorophyll fluorescence, a passive tracer, would be less strongly affected.

A second possible explanation of the relative peakiness of the temperature PDFs is that biological processes are important in determining the small-scale properties of the horizontal distribution of chlorophyll. For example, it is possible that unusually large fluctuations in phytoplankton concentration attract grazers,

which could then act to eliminate these large fluctuations, reducing the intermittency of the phytoplankton distribution.

3.4 Temperature-Fluorescence Relationship

To which length scales does the gradient alignment mechanism of Section 3.2 apply? At the smallest scales, the alignment is wiped out by molecular diffusion, which erases the 'memory' of the initial tracer field. As significant contraction can occur only on scales small relative to the size of the basin, the range of scales on which alignment might occur is bounded above and below. But the alignment we actually observe occurs over a narrower range than that. It is difficult to distinguish on which scales gradients are aligned by simply looking at the records (see Figs. 3.2-3.5). The wavelet coefficients from Section 3.3 can help resolve this issue. Associated with each wavelet coefficient w is a phase

$$\phi = \tan^{-1}\left(\frac{\text{Im}(w)}{\text{Re}(w)}\right).$$

At a given scale and location we can define the temperature-fluorescence phase difference as $\Delta\phi(x,s) = \phi_\theta(x,s) - \phi_f(x,s)$, where ϕ_θ and ϕ_f refer to potential temperature and fluorescence respectively. Fluorescence-temperature gradient alignment is indicated by values of $\Delta\phi$ near zero (in phase) and $\pm\pi$ (out of phase). Peaks at zero and $\pm\pi$ in the PDF of $\Delta\phi$ at a given length scale s are thus an indication of a tendency for temperature and fluorescence gradients to align on that scale.

Figure 3.12 shows the distribution of wavelet phase difference for the 200-dbar isobar tow. PDFs of $\Delta\phi$ for scales ranging from 1 km to 100 km are stacked together from front to back. The alignment is almost exclusively in-phase because the variability along that surface is dominated by vertical displacements, and the vertical gradients are of unchanging sign (see Fig. 3.1). The relationship weakens at smaller scales, but remains evident all the way down to a kilometer.

On scales of 10 km and above, the alignment between temperature and fluorescence on the 50-dbar tow is predominantly in-phase (Fig. 3.13). This large-scale alignment is confined mainly to the northern end of the tow, and is directly visible in Fig. 3.3. As discussed in Section 3.2, the alignment is probably caused by stirring. At scales smaller than 10 km, temperature and fluorescence are aligned out-of-phase, a relationship which holds throughout the tow, but is strongest in the southern part. At these scales, both temperature and fluorescence are strongly correlated with measured density, suggesting that the small-scale alignment is the result of diapycnal profiling. The correlation between pressure and both temperature and fluorescence is very weak, however. Thus, the diapycnal profiling is caused not by deviations in SeaSoar's flight path, but by vertical displacement of water by internal waves.

On the 25.5 kg/m^3 isopycnal tow, in-phase gradient alignment is evident at scales of 10 km and above (Fig. 3.14). Out-of-phase alignment is evident on the largest scales as well, though less strongly because only a quarter of the section (Fig. 3.4) was aligned out of phase. Like the large-scale alignment at 50 dbar, this relationship is well explained by stirring-enhanced gradients.

Alignment is not obvious at the larger scales on the 24.8 kg/m^3 isopycnal tow (Fig. 3.15), but some alignment, mainly in-phase, is evident at scales of 1 km and smaller. At these scales, fluctuations in density are aligned with those in both temperature and fluorescence. This suggests that the observed small-scale alignment between temperature and fluorescence is the result of unintentional diapycnal profiling, demonstrating that the corrections made for deviation from the isopycnal are not perfect.

To summarize, then, the alignment that we attribute to gradient enhancement by stirring (namely, that on the 25.5 kg/m^3 isopycnal and the in-phase alignment at 50 dbar), disappears below a scale of 10 km. Smaller-scale alignment, observed most strongly on the 50 dbar tow but also on the 200 dbar and 24.8 kg/m^3 isopycnal tows, is likely the result of diapycnal profiling.

3.5 Renovating Wave Model

Plankton ecosystem models with simple representations of turbulent stirring can reproduce the power-law spectra typical of oceanic fluorescence measurements (e.g. Abraham, 1998). We explore the effect of such stirring on tracer gradient alignment with a simple Lagrangian advection model, which has been dubbed (William Young, pers. commun.) the 'renovating wave' (hereafter RW) model. This model was originally used in dynamo theory (see e.g. Childress and Gilbert, 1995), and similar formulations have found use in the study of turbulence (Pierrehumbert, 1994) and plankton patchiness (Young et al., 2001). The model consists of sinusoidal shear flows, which are periodically renovated by the choice of

new random values for phase and orientation. During each iteration, the flow is steady and unidirectional, so particle trajectories can be computed exactly. This freedom from numerical diffusion is the main advantage the RW model has over other possible formulations, such as a quasi-geostrophic velocity model.

In a two-dimensional rectangular coordinate system, we can describe the RW velocity as follows: the x' axis is rotated by the angle α relative to the x-axis. The x' and y' components of the velocity are, respectively, $u' = 0$, and $v' = V \sin(ky' + \beta)$. V is the amplitude of the velocity 'wave', β is its phase, and k is the wavenumber. After time τ, new values for α and β are chosen at random from a uniform distribution between 0 and 2π. This process is repeated N times. Thus the flow is independent of time (t) except at $t = n\tau$ (where $n = 1,2,...,N$) at which times the velocity field is abruptly 'renovated'. Nondimensionalizing distance by k^{-1} and time by $(Vk)^{-1}$, we are left with just the dimensionless parameter $\gamma = \tau k V$. This parameter may be thought of as a ratio of length scales: a typical particle displacement during a single iteration of the RW flow divided by the wavelength of the renovating wave. Figure 3.16 is a schematic representation of the flow during a single iteration, labeled in dimensionless units. A complete description of the model flow requires only two parameters: γ and N.

As the flow is incompressible and there is no diffusion, tracer concentration is conserved following a fluid particle. So we track fluid particles from their initial locations in a field of smoothly varying tracer concentration to their final locations on our model grid, yielding tracer concentration after RW stirring. In order to

avoid the necessity of interpolating particle positions onto a grid and the associated imprecision, we employ the following trick: the final particle positions are chosen to coincide exactly with a grid, and the model is run backward in time to obtain the initial particle positions. We specify tracer concentration as a function of these initial positions. Perhaps the simplest non-constant function possible is a planar initial concentration field (uniform initial concentration gradient), and all the simulations included in the present study use this choice.

When two tracer fields, initially uncorrelated, are stirred by the same RW flow, similar features develop in both fields (Fig. 3.17). In this example, the initial tracer concentration gradient was uniform and of equal magnitude in each case, but initial gradient direction differed by 90 degrees. The number of iterations, N, is 70, and γ is 0.8. The size of the domain pictured, in units of k^{-1}, is 2π; that is, one complete RW wave would fit along each side of the box. In some locations, high-concentration features in one field correspond to low-concentration features in the other (out-of-phase gradient alignment), while in others, corresponding features in the two fields are either both high- or both low-concentration (in-phase gradient alignment). In the Appendix to this chapter we show that, for the case just described, the alignment of tracer gradients is inevitable. This mechanism is likely responsible for the alignment observed on the 25.5 kg/m^3 isopycnal.

PDFs of wavelet phase differences for two tracers stirred by the RW process that produced the fields in Fig. 3.17 are sharply peaked around $\theta = 0$ and $\theta = \pi$ (Fig. 3.18). Thus, the stirred fields exhibit both in-phase and out-of-phase alignment at all scales. Potential temperature and chlorophyll on the 25.5 kg/m^3

isopycnal (Fig. 3.14) and the 50-dbar isobar (Fig. 3.13) were aligned on large scales, but in both cases, the alignment faded out at a length-scale of ~10 km (as discussed in Section 3.4, the small-scale, out-of-phase alignment on the 50-dbar tow was caused by internal waves). If stirring caused the alignment we observed, we would like to understand what prevented alignment on scales smaller than 10 km.

One possibility is that small-scale gradient alignment is destroyed by mixing. In the irreversible process of turbulent diffusion, memory of the initial field is lost— narrow tracer filaments that would be aligned are simply mixed out of existence. Turbulent diffusion may be included in the RW model by introducing independent random displacements along with the RW advection velocity at each time-step. These diffusive displacements are meant to reflect the combined effect of all the turbulent motions on scales smaller than the grid scale (the large-scale motion being our prescribed RW flow), so there is no correlation between the displacements experienced by neighboring particles. We use normally distributed, isotropic diffusive displacements, with a RMS magnitude of D. In the absence of advection, this corresponds to a diffusion coefficient, κ, of $\frac{1}{2}D^2\tau^{-1}$. Defining $\delta = kD$, the model now contains two nondimensional parameters: γ describes the nondimensional distance moved at each iteration due to advection, and δ the nondimensional distance moved due to turbulent motions. The ratio of diffusive to advective timescales is the Peclet number, $\mathrm{Pe} = \gamma/\delta^2$.

A single realization of the RW process with diffusive displacements causes local scattering of fluid particles and so produces a 'speckled' field (Fig. 3.19, left

panel). Here the initial concentration field and RW stirring sequence are identical to those in Fig. 3.17, left panel, but we have included diffusive displacements, with $\delta = 0.024$. If the grid is regarded as a pixelation of the fluid, then the concentrations we thus obtain represent the concentration at the initial location of one infinitesimal point in each pixel. Another tiny fluid particle in the same pixel would in general have a different initial location and concentration. Rather than the concentration at a single particle, we would like a representative concentration for the entire pixel. Accordingly, we run the model a large number of times (here, 100) with identical RW stirring but independent diffusive displacements. The concentration assigned to a pixel is then the mean concentration at that pixel over the ensemble, which we can think of as the average concentration over the 'box' of fluid represented by the pixel. The assumption is that the RW wavelength is large compared to the grid scale, so that the advecting velocity is essentially constant over each pixel, and that the grid scale is large compared to the diffusion velocity decorrelation length scale, so that the diffusive displacements of the particles which end up scattered throughout that pixel are unrelated. The ensemble average concentration field after RW advection with diffusion is shown in Fig. 3.19, right panel.

In order to investigate the effect of diffusion on gradient alignment in the RW model, we follow the procedure described above to stir and mix two tracer fields with distinct initial conditions. As in Fig. 3.18, the two tracers are stirred by the same RW flow, but now each of the tracers is subject to its own set of random diffusive displacements. This is tantamount to choosing, for each tracer, a unique,

random set of 100 fluid particles within each pixel from which to form the ensemble average. Using the identical set of diffusive displacements for each tracer (that is, using the same set of fluid particles) would introduce artificial correlations between the two fields—any inhomogeneity in the distribution of diffusive displacements in a pixel would cause a similar bias in each of the two fields.

Our two stirred tracer fields still show gradient alignment at scales above 0.1 (nondimensional distance), but the peaks in the wavelet phase difference PDFs vanish at smaller scales (Fig. 3.20). The parameters are the ones used in Fig. 3.19: $N=70$, $\gamma=0.8$, and $\delta=0.024$. As an example of the level of horizontal mixing required in the ocean to erase small-scale gradient alignment, we can choose values for dimensional model parameters. Setting $k = 10^{-4}\,\mathrm{m}^{-1}$ (so that the RW wavelength or typical 'eddy' size is ~60 km), the model cutoff length scale of approximately 0.1 corresponds to the observed cutoff length scale of approximately 10 km. Choosing a maximum current velocity V of 0.1 m/s, the time between renovations, τ, is $8\times10^{4}\,\mathrm{s}$, or roughly one day, and D, the typical diffusive displacement per renovation, is 240 m. The diffusion coefficient, κ, is then 0.36 m^2/s, roughly comparable with measurements of open-ocean horizontal eddy diffusivity on 1-10 km scales (Ledwell et al., 1998).

The result of small-scale turbulence (the 'diffusive displacements' in our model) and mixing (the averaging of an ensemble of particles in each pixel) is thus to suppress gradient alignment at small scales. Turbulent mixing, then, is one possible explanation for the deterioration of gradient alignment observed at small scales on isopycnals.

A second possible influence on the alignment of fluorescence and temperature gradients is spatial variability in the net phytoplankton growth rate. The models discussed above address the alignment of gradients in two stirred conservative tracers. We now investigate the relationship when one of the tracers is reactive.

We represent phytoplankton growth in the RW model by allowing one of the tracers (P) to evolve according to the logistic equation: $\dfrac{\partial P}{\partial t} = rP(1 - P/K)$, where the derivative is taken following the fluid particle trajectory. Here, the growth rate, r, is a constant, but the carrying capacity, K, varies with position: $K = K_0 + K_1 e^{-(x^2 + y^2)/R^2}$. The carrying capacity thus has a baseline value of K_0, and a two-dimensional gaussian bump of radius R and magnitude K_1 centered in the model domain. We choose, arbitrarily, values of 0.2 for K_0, and 1 for K_1. The carrying capacity bump represents an area where increased irradiance or nutrient input permits the support of a higher concentration of phytoplankton. Neither nutrients nor light are explicitly included, but the quadratic death rate in the logistic equation reflects the depletion of nutrients and increased scattering and absorption of light that accompany an increase in phytoplankton concentration. Though nutrients in the ocean are advected with the flow and spatial patterns in the light flux change with time, we choose, for simplicity, a time-independent function for the carrying capacity.

The effect of logistic growth depends on the growth rate, r. Again scaling time by $(Vk)^{-1}$, the nondimensional growth parameter is $\rho = r/Vk$, which may be

thought of as a ratio of timescales: $(Vk)^{-1}$ is analogous to an "eddy crossing time," and r^{-1} is the growth timescale. For small growth rates, ($\rho \gamma N \sim 1$ or less), the filamental structure of the stirred field is similar to what it would be for a conservative tracer: compare the left panel of Figure 3.17 with the left panel of Figure 3.21, which results from the same initial conditions and the same stirring, but with $\rho = 0.015$ and $R = 2$. For larger growth rates, growth saturation fundamentally alters tracer structure; the only change in the right panel of Figure 3.21 relative to the left is an increased growth rate: $\rho = 0.25$. With the same choices for dimensional parameter values as before ($k = 10^{-4}\,\mathrm{m}^{-1}$, $V = 0.1\,\mathrm{m/s}$), the slow and fast dimensional growth rates are 0.017 day^{-1} and 0.29 day^{-1}, respectively, and the radius of the region of elevated carrying capacity is 20 km. As fast growth continually 'resets' the tracer field to match the carrying capacity structure, features borne of earlier stirring are erased.

Logistic growth with the smaller growth rate slightly weakens the alignment of small-scale gradients (Fig. 3.22). With the larger growth rate, alignment is drastically reduced at all scales, and at the smallest scales, it is eliminated altogether (Fig. 3.23). Thus, rapid phytoplankton growth provides a second possible mechanism for the suppression of small-scale temperature and fluorescence gradients.

3.6 Summary and Discussion

The PDFs of scale-specific fluctuations in temperature and fluorescence (Section 3.3) are very similar to each other for scales of a few kilometers and larger. With the exception of the 200 dbar tow, on which variability was dominated by internal waves, fluorescence PDFs for length scales near one kilometer differ in shape from the corresponding temperature PDFs. On this scale, the horizontal distribution of temperature on the 50 dbar isobar and the 25.5 kg/m^3 isopycnal was more intermittent than that of fluorescence, while it was less intermittent on the 24.8 kg/m^3 isopycnal. The difference suggests that on ~1 km scales, temperature and fluorescence distributions may be established by distinct mechanisms. At the smallest scales, such comparisons are precluded by instrumental noise in the fluorescence data.

The alignment of gradients in potential temperature and chlorophyll fluorescence on the 25.5 kg/m^3 isopycnal, both in-phase and out-of-phase, indicates that at least at scales of 10-100 km, stirring may well play a dominant role in setting the along-isopycnal distribution of chlorophyll below the euphotic zone. In-phase alignment on the 50-dbar tow suggests that stirring can also control the horizontal chlorophyll distribution at these scales in the euphotic zone and above the mixed layer base. However, alignment at 10-100 km scales is scarcely evident on the 24.8 kg/m^3 isopycnal, demonstrating that stirring is not always the primary influence on along-isopycnal chlorophyll. The correlation between isopycnal depth and chlorophyll fluorescence on this tow suggests that locally enhanced growth rates can be important in determining the chlorophyll distribution.

Stirring does not appear to produce much alignment on scales smaller than 10 km. Small-scale alignment on isobars is the result of vertical advection, and the apparent alignment on the 24.8 kg/m^3 isopycnal is caused by deviations of the instrument package from the isopycnal. Correcting the data for these deviations reduces the strength of the alignment, but as a perfect correction is impossible, some leftover alignment is inevitable.

We have employed a renovating wave model to demonstrate the alignment of gradients in stirred tracers, and to investigate possible reasons for the lack of alignment at scales smaller than the observed cutoff length scale of approximately 10 km. The model suggests that both turbulent mixing and phytoplankton growth could weaken small-scale gradient alignment. In our model with logistic growth and a spatially varying carrying capacity, only growth with a time-scale short in comparison with the duration of the advecting flow is effective in suppressing gradient alignment. A search of N-γ-δ parameter space reveals that the cutoff length scale, L, below which gradient alignment is destroyed by diffusion in the RW model increases with increasing δ, and decreases with increasing N and γ.

The relationship between δ and L can be verified for any value of δ small compared to one, but N and γ cannot independently be varied over a very large dynamic range. Gradient alignment only occurs if the cumulative effect of the RW stirring has been to produce highly strained regions in the fluid. If either N or γ is too small, this condition is not satisfied. On the other hand, if either N or γ is too large, the strain is so extreme that initially distant fluid particles (i.e., particles whose separation is comparable to the RW wavelength) approach closer than the

model grid spacing, the tracer filaments become too narrow to be resolved, and the smoothly varying character of the tracer field is lost.

Consider an infinitesimal material line element of length l at the origin, oriented along the y-axis in Fig. 3.16. In the x' y' coordinate system, this material line element is represented as a vector: $l(\sin\alpha, \cos\alpha)$. After being advected by the first iteration of the RW flow, the material line element has been stretched, and becomes $l(\sin\alpha, \cos\alpha + \gamma\cos\beta\sin\alpha)$. The squared length of the material line element is now $l^2[1 + 2\gamma\cos\beta\sin\alpha\cos\alpha + \gamma^2\cos^2\beta\sin^2\alpha]$. Both α and β are uniformly distributed between 0 and 2π, so the expectation value of the square of the elongation factor E of a small random material line element during a single RW iteration is $\langle E^2 \rangle = 1 + \frac{1}{4}\gamma^2$. Provided that the line element stays short compared to the RW wavelength, we can thus describe the elongation after N iterations as $\sqrt{\langle E^2 \rangle}^N = \left(1 + \frac{1}{4}\gamma^2\right)^{N/2}$, which is a measure of the total strain. If we denote the ratio of the RW wavelength to the gridscale by R, then the strain condition for the occurrence of gradient alignment becomes $1 \ll \left(1 + \frac{1}{4}\gamma^2\right)^{N/2} \ll R$. As a dimensional example, if we retain the parameter choices from Section 3.5 ($k = 10^{-4}\,\text{m}^{-1}$, $V = 0.1\,\text{m/s}$, $\tau = 8\times10^4\,\text{s}$), the lower bound on the time required for gradient alignment to develop is on the order of a month.

Within the region of parameter space where we observe gradient alignment ($1 \ll \left(1 + \frac{1}{4}\gamma^2\right)^{N/2} \ll R$), increasing strain pushes the lower bound L of the gradient alignment length scale toward smaller values, and increasing diffusion does the

opposite. While the growth of L with δ is intuitive, it is perhaps a little surprising that throughout most of parameter space, L is several times larger than δ. Adding diffusion to the RW model eliminates gradient alignment at scales larger than the individual diffusive displacements. To two neighboring fluid particles whose separation is small compared to the RW wavelength, the RW flow looks like a linear shear flow with a periodically changing direction. In this regime, the distance between the two particles grows exponentially in time, which is the expected behavior of nearby particles in real turbulent flows (Batchelor, 1952). One consequence of this is that perturbing a particle's location by introducing a small diffusive displacement can have a comparatively large effect on where the particle ends up several RW iterations later. This 'butterfly effect' helps explain how seemingly small displacements can wipe out tracer filaments and erode gradient alignment at scales larger than the displacements themselves.

There are many choices besides the Morlet wavelet transform for analyzing spatial distributions from data collected along a line. One popular alternative statistic is the so-called scalar difference (e.g. Warhaft, 2000). For a scalar S, (say temperature), the scalar difference is defined as $\Delta S(d)/\langle \Delta S(d)^2 \rangle^{1/2}$. Here, d is the separation between a pair of points, and $\Delta S(d)$ is the difference in S between the two. For any values of d we choose, we can take all pairs of points in the record separated by d, and plot probability density functions of the scalar differences. A PDF with long tails indicates intermittent behavior, while sharply dropping tails imply relative uniformity.

The scalar difference may be expressed as a convolution of the scalar S with a pair of Dirac delta functions: $\Delta S(x,d) = S * [\delta(x - \frac{d}{2}) - \delta(x + \frac{d}{2})]$. Convolution in physical space is equivalent to multiplication in wavenumber space, so the Fourier transform of the convolution function reveals the spatial scales of variability to which the scalar difference statistic is sensitive. The Fourier transform of $\delta(x - \frac{d}{2}) - \delta(x + \frac{d}{2})$ is $2i\sin(kd/2)$, where k is the wavenumber. The magnitude of the Fourier transform reaches a maximum at $k = \pi/d$, corresponding to variability with a semi-wavelength of d. There are also maxima in the magnitude at $k = n\pi/d$ for all odd integers n. If the goal is to understand the degree of intermittency of the field as a function of spatial scale, it is desirable to treat each scale separately, rather than using a method of analysis that folds variability at multiple scales into a single statistic. In most situations, the spectrum of tracers is decidedly red—that is, there is more variability at longer length scales. For this reason, variability at the fundamental length scale, that is, at a semi-wavelength of d, may dominate the scalar difference signal. Nonetheless, we chose here to use a mode of analysis that focuses on each wavenumber band individually. Instead of a pair of delta functions, we use an analyzing function ψ that is compact in both physical space and wavenumber.

Large-scale fluid motions, through accumulated strain, produce structure in tracer fields at much smaller scales. Meanwhile, small-scale turbulent motions promote mixing, which destroys small-scale tracer structure. We have argued that the demonstrated alignment of horizontal chlorophyll and temperature gradients is likely the result of large-scale motions, and suggested turbulent mixing and rapid

phytoplankton growth as possible causes of the breakdown of that alignment at small scales. The role that spatial variability in phytoplankton growth plays in determining the horizontal distribution of chlorophyll within the euphotic zone is an important question. Large and variable vertical chlorophyll gradients in this region make investigation of this issue by analysis of a horizontal tow difficult. During an April 2005 cruise in the northeastern Pacific, we towed SeaSoar along a sawtooth track spanning the deep chlorophyll maximum, completing a cycle every 700 meters over a section 1000 km in length. Future analysis of this dataset and others like it will further our understanding of the combination of factors controlling chlorophyll structure in the ocean.

Appendix (Chapter 3)

Proof that alignment of stirred tracers with uniform initial gradients is inevitable.

Let $\mathbf{u}$ be a two-dimensional incompressible velocity field, so that $\nabla \cdot \mathbf{u} = 0$.

Let a and b be conservative, nondiffusive tracers subject to advection by $\mathbf{u}$. Then a and b satisfy the advection equation:

$$\frac{\partial a}{\partial t} + \mathbf{u} \cdot \nabla a = 0, \text{ and } \frac{\partial b}{\partial t} + \mathbf{u} \cdot \nabla b = 0.$$

This simply states that a and b are conserved following fluid particle trajectories.

We define the Jacobian of a and b as the cross product of ∇a with ∇b:

$$J(a,b) = \frac{\partial a}{\partial x}\frac{\partial b}{\partial y} - \frac{\partial a}{\partial y}\frac{\partial b}{\partial x}.$$

Plugging the Jacobian, written in this form, into the advection equation, it is easily shown that

$$\frac{\partial J(a,b)}{\partial t} + \mathbf{u} \cdot \nabla J(a,b) = 0.$$

Thus, the Jacobian is also conserved following fluid particle trajectories.

The Jacobian can alternately be expressed as

$$J(a,b) = \|\nabla a\|\|\nabla b\|\sin\theta,$$

where θ is the angle between ∇a and ∇b. In the simple case of planar initial concentration fields, ∇a, ∇b, and θ are independent of position at time $t = 0$, so

$J(a,b) = k$, where k is a constant. That is, the Jacobian is constant, independent of position and time. However, as stirring stretches the tracer fields a and b, the large-time behavior of $\|\nabla a\|$ and $\|\nabla b\|$ is to increase without bound (see e.g. Eckart, 1948). Therefore

$$\|\nabla a\| \|\nabla b\| \sin \theta = k$$

requires that

$$\sin \theta \to 0 \text{ as } t \to \infty.$$

Under the influence of stirring, the tracer concentration gradients tend toward alignment, either in phase ($\theta = 0$), or out of phase ($\theta = \pi$).
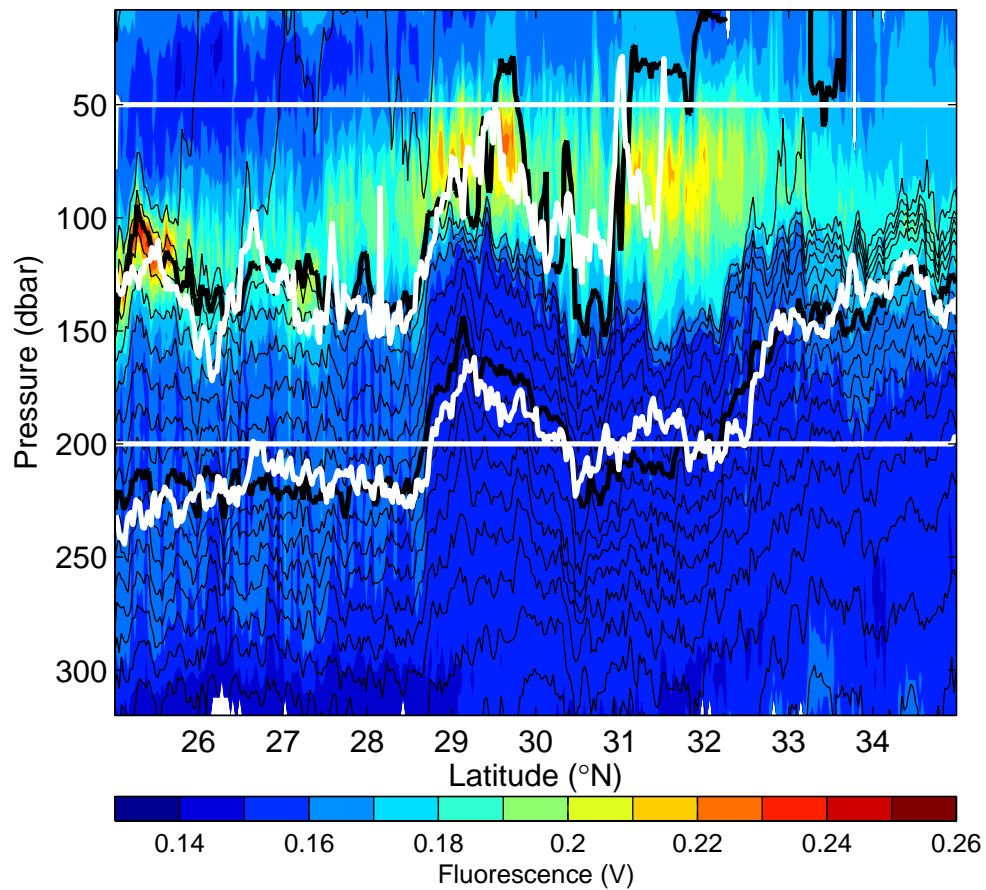
Figure 3.1. Fluorescence section with isobar and isopycnal tows drawn in white. Black lines are 0.1 kg/m^3 density contours. The jagged white lines do not coincide with the black density contours because by the time the isopycnal tows were carried out, the isopycnals had moved. In terms of chlorophyll concentration, the color scale runs roughly from 0 to 2 mg/m^3.
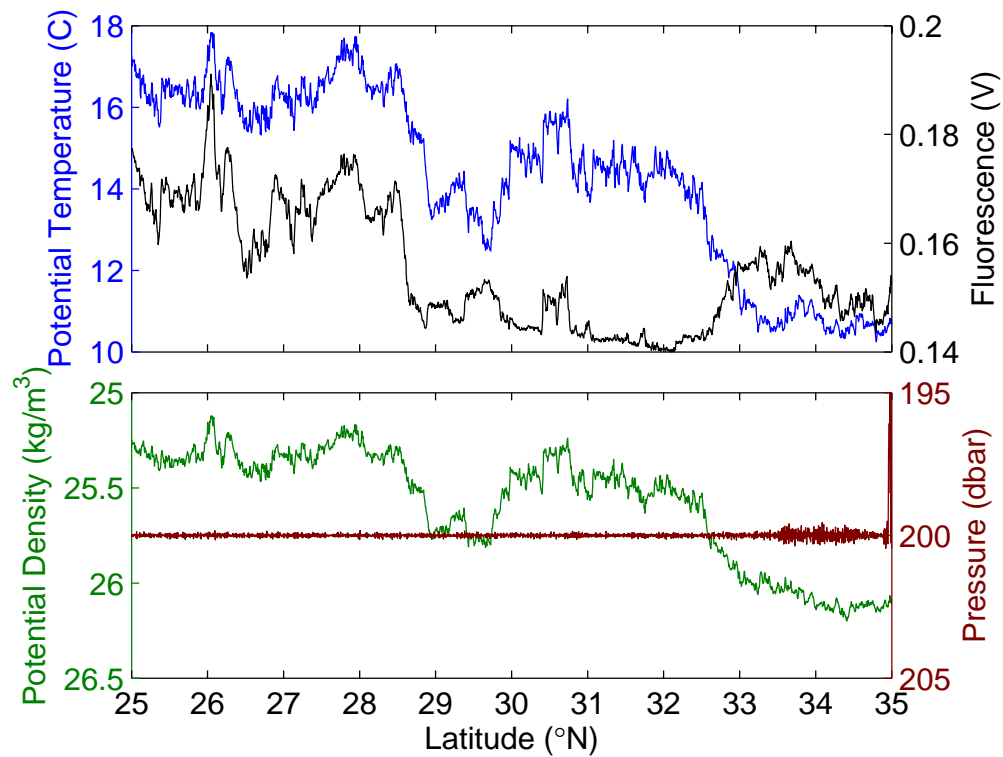
Figure 3.2. Potential temperature (blue), fluorescence (black), potential density (green), and pressure (brown) data from the 200-dbar isobar tow, after application of a 500-meter running mean filter. Note the strong correlation between temperature, fluorescence, and density.
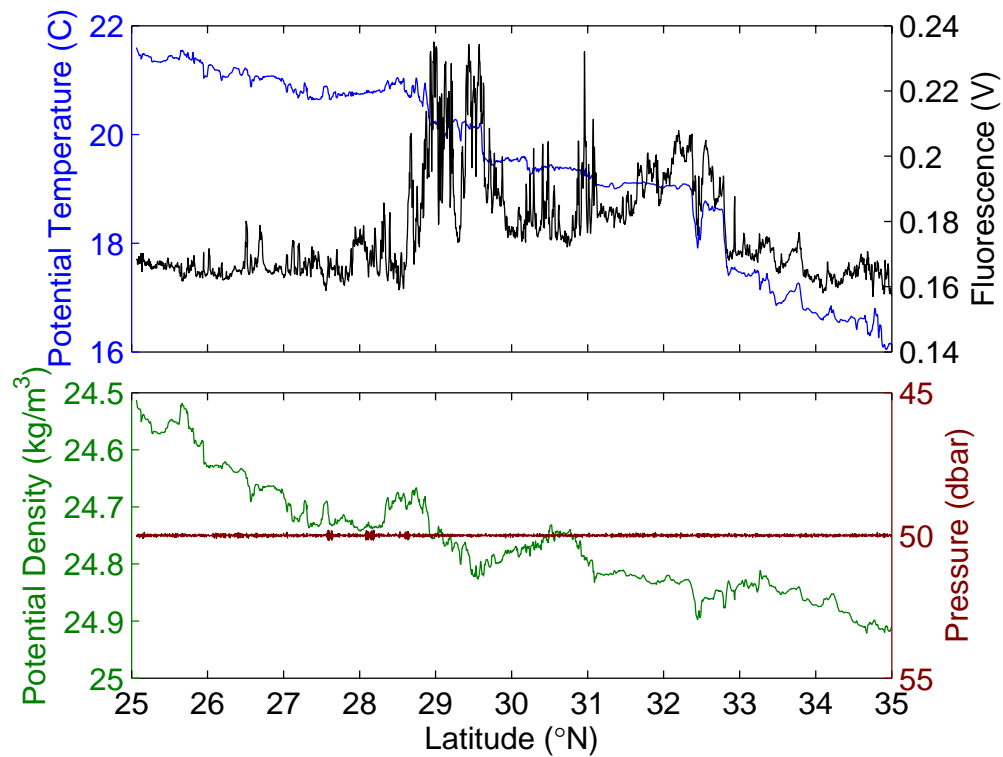
Figure 3.3. Data from the 50-dbar isobar tow, plotted as in Fig. 3.2. Temperature and fluorescence are strongly correlated in the northern portion of the tow.
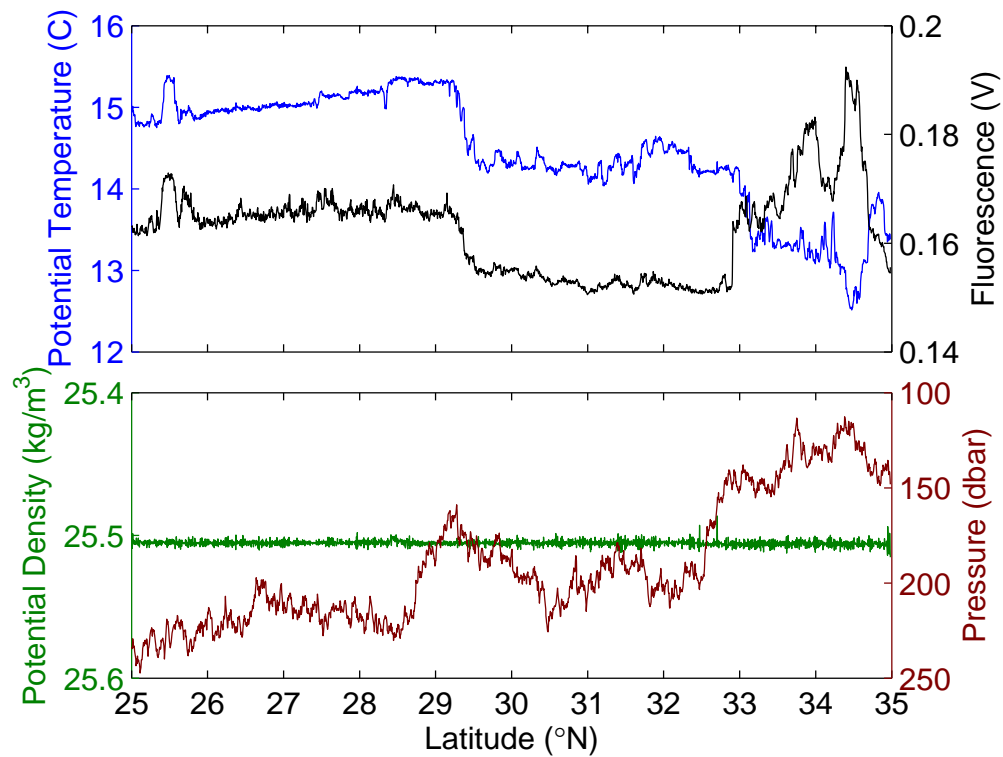
Figure 3.4. Data from the 25.5 kg/m^3 isopycnal tow, plotted as in Fig. 3.2. Near 32° N the temperature-fluorescence relationship switches from in-phase to out-of-phase.
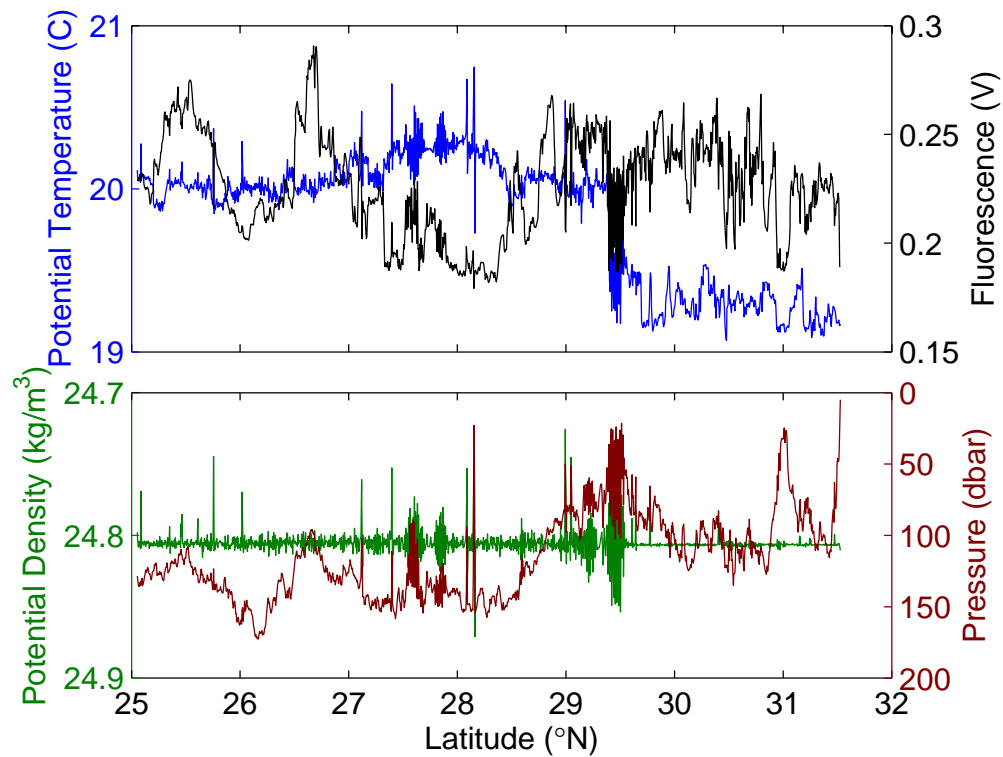
Figure 3.5. Data from the 24.8 kg/m^3 isopycnal tow, plotted as in Fig. 3.2. The correlation between pressure and fluorescence in the southern part of the tow indicates the stimulation of algal growth by the increase in irradiance produced by uplift of the isopycnal.
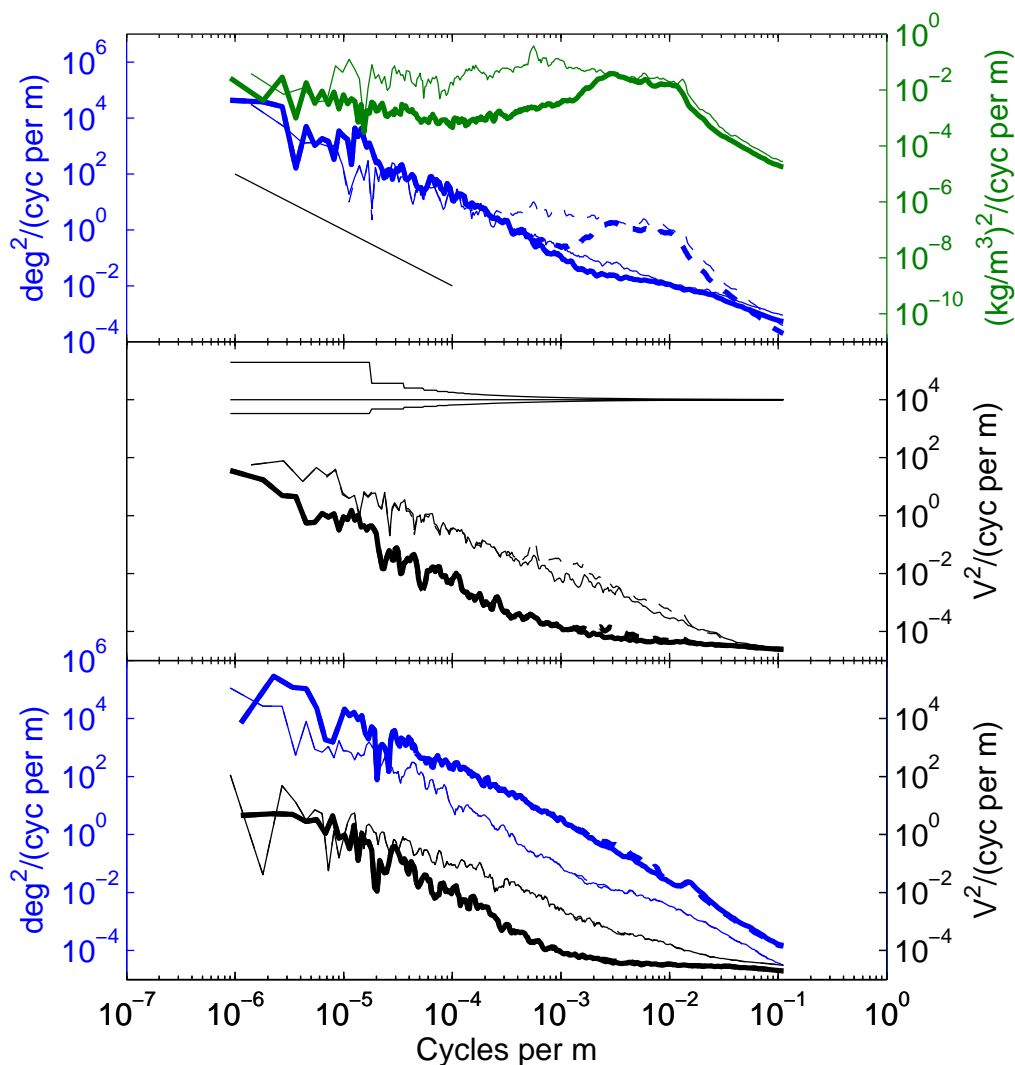
Figure 3.6. Power spectra of potential temperature (blue lines), chlorophyll fluorescence (black lines), and potential density (green lines) from the horizontal tows. Spectra of raw temperature and fluorescence data are dashed, and the corresponding corrected spectra are solid. Light lines refer to the shallow tows (50 dbar and 24.8 kg/m^3) and heavy lines to deep ones (200 dbar and 25.5 kg/m^3). *Upper panel*: Spectra of temperature and potential density measured during the isopycnal tows. The correction eliminates much of the spectral signature of the density variability from the temperature data. The black line has a slope of –2. *Middle panel*: Fluorescence spectra from the isopycnal tows. Also shown are the 5%-95% confidence intervals for all the spectra presented here. *Bottom panel*: Spectra of temperature and fluorescence from the isobar tows. The high-frequency whitening of the fluorescence spectra in the lower two panels is caused by instrumental noise.
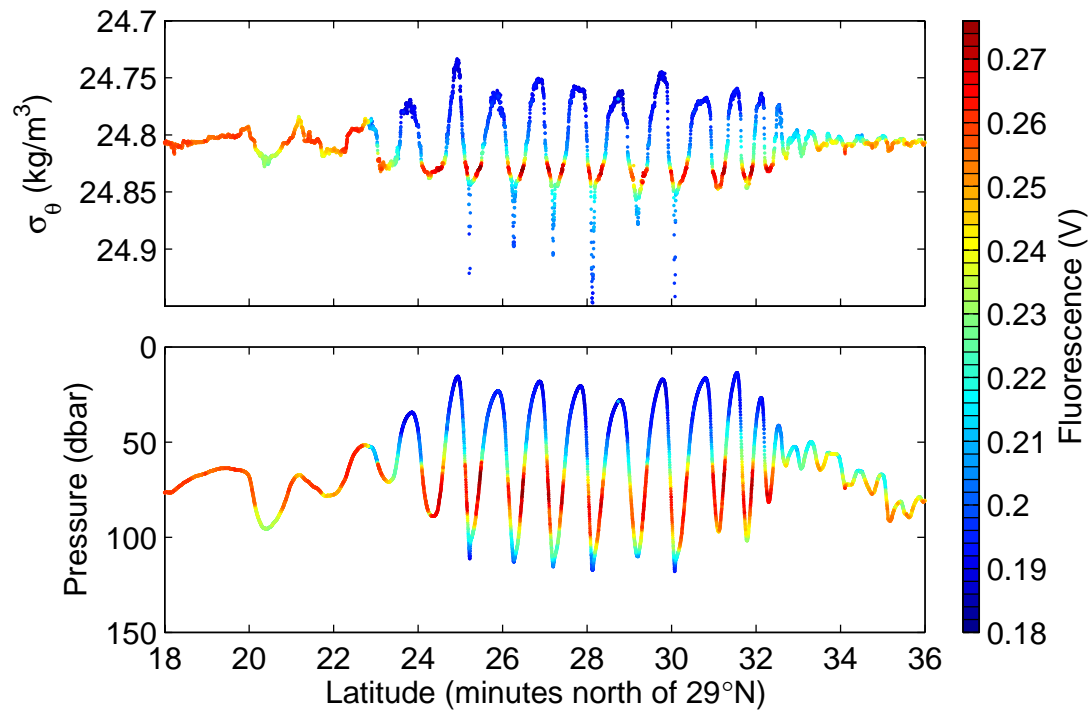
Figure 3.7. *Upper panel*: Potential density measurements, averaged to 1 Hz, from a short section of the 24.8 kg/m^3 isopycnal tow where deviations from the isopycnal were particularly severe. The color of each point indicates chlorophyll fluorescence, showing that the oscillations spanned the deep chlorophyll maximum. *Lower panel*: Same as above, but with pressure as the vertical axis.
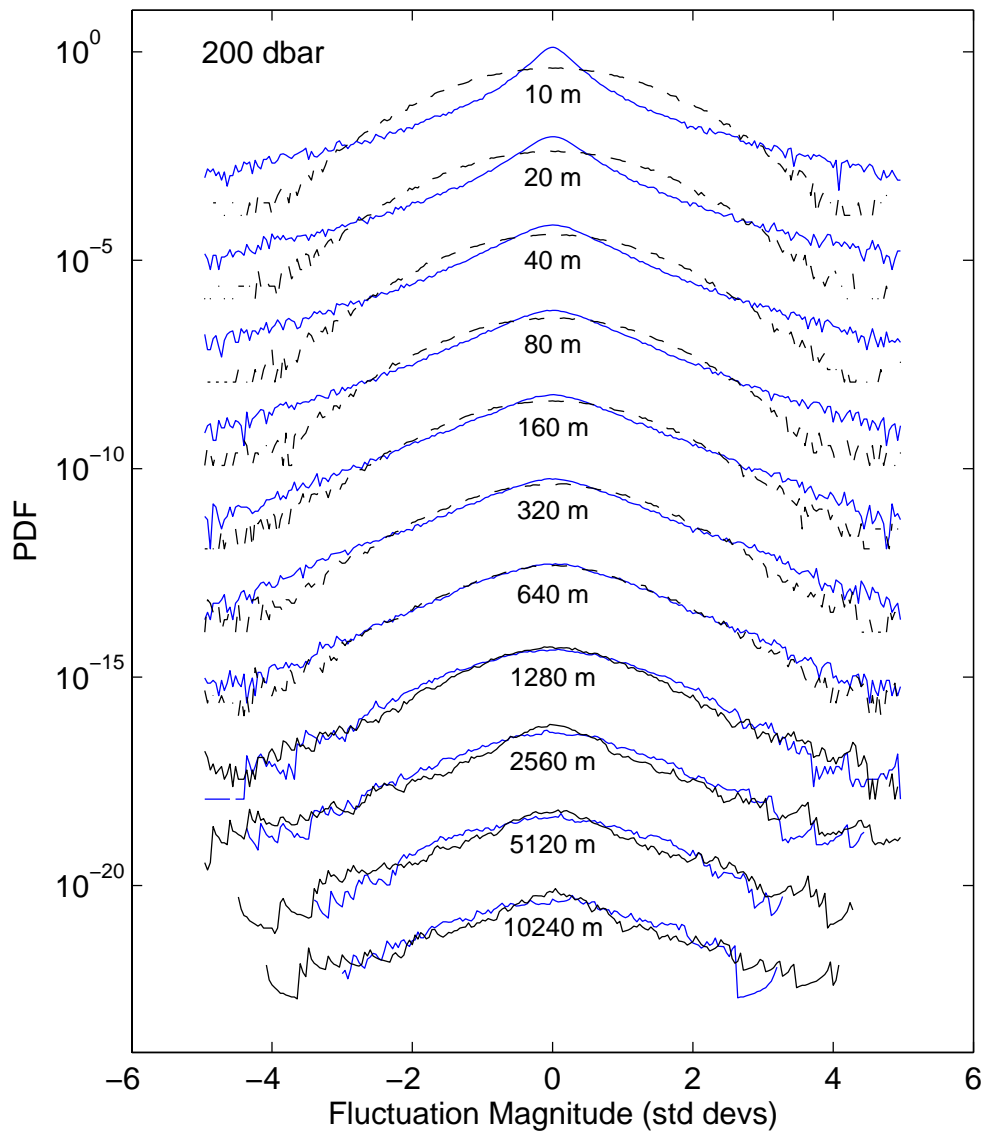
Figure 3.8. PDFs of potential temperature (blue) and fluorescence (black) wavelet coefficients on the 200-dbar isobar tow, showing the distribution of the magnitude of fluctuations in these tracers at each of 11 logarithmically-spaced scales (wavelengths). Each pair of PDFs is labeled with its wavelength, and displaced by two orders of magnitude from the pair above it. Small-scale fluorescence PDFs are dashed to indicate the influence of instrumental noise.
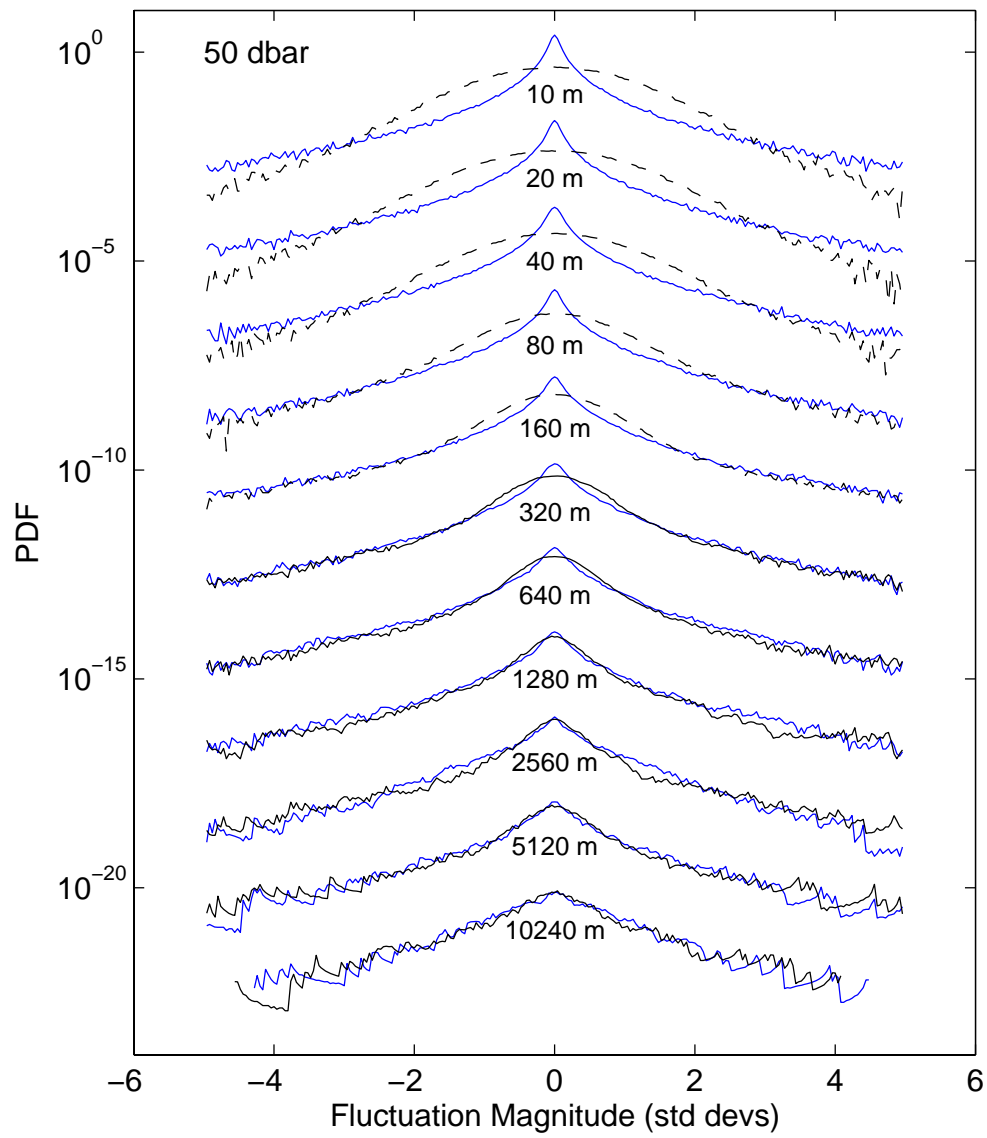
Figure 3.9. PDFs of temperature and fluorescence wavelet coefficients on the 50-dbar isobar tow, plotted as in Fig. 3.8.
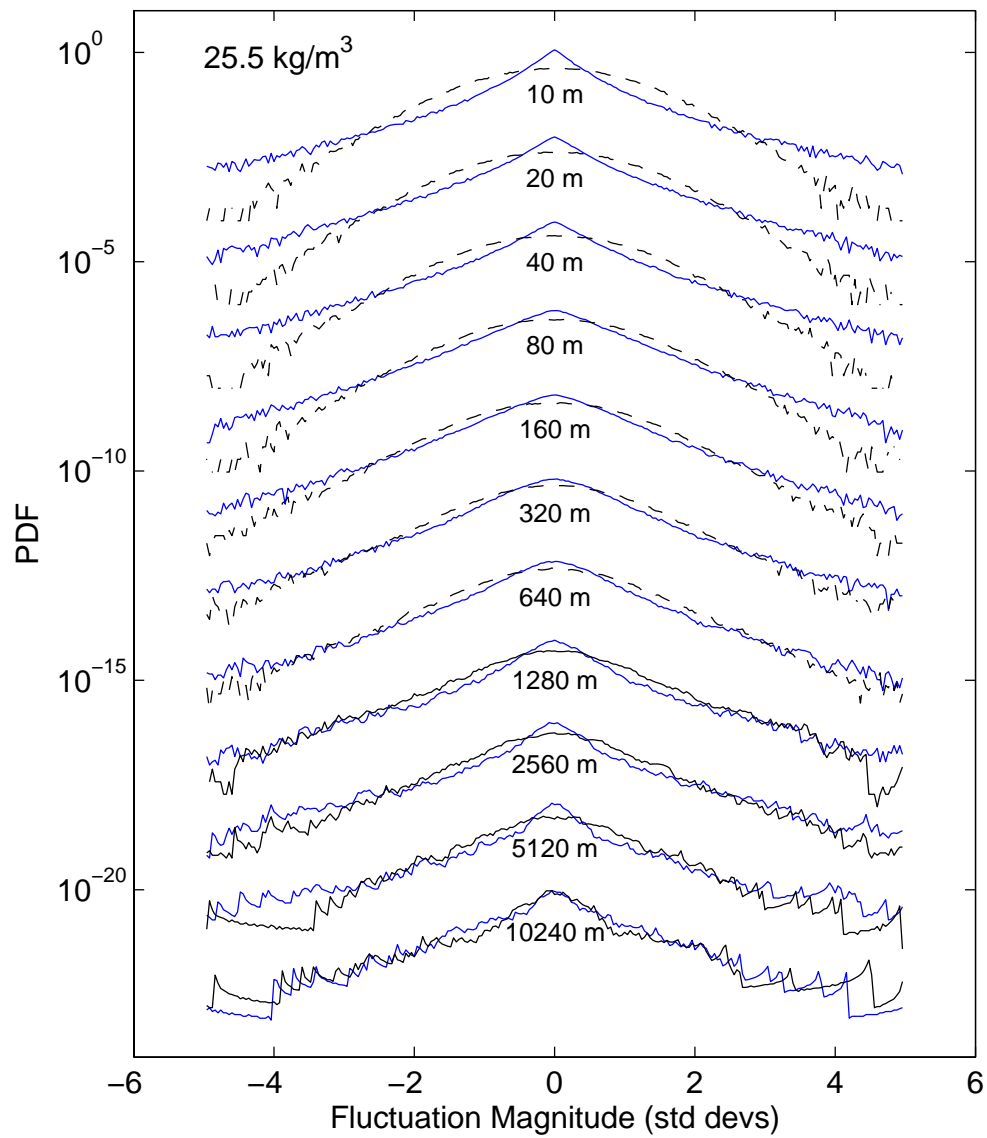
Figure 3.10. PDFs of temperature and fluorescence wavelet coefficients on the 25.5 kg/m^3 isopycnal tow, plotted as in Fig. 3.8.
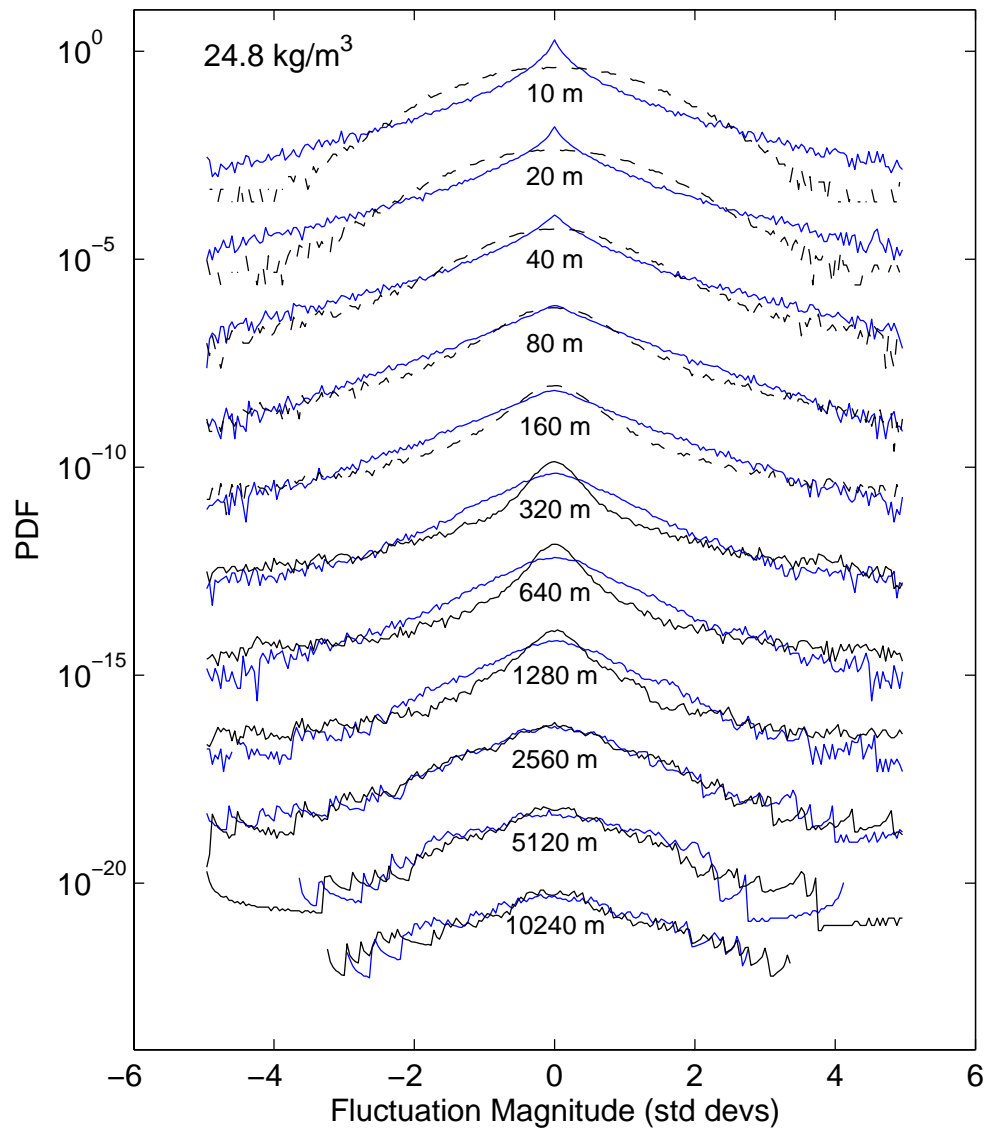
Figure 3.11. PDFs of temperature and fluorescence wavelet coefficients on the 24.8 kg/m^3 isopycnal tow, plotted as in Fig. 3.8.
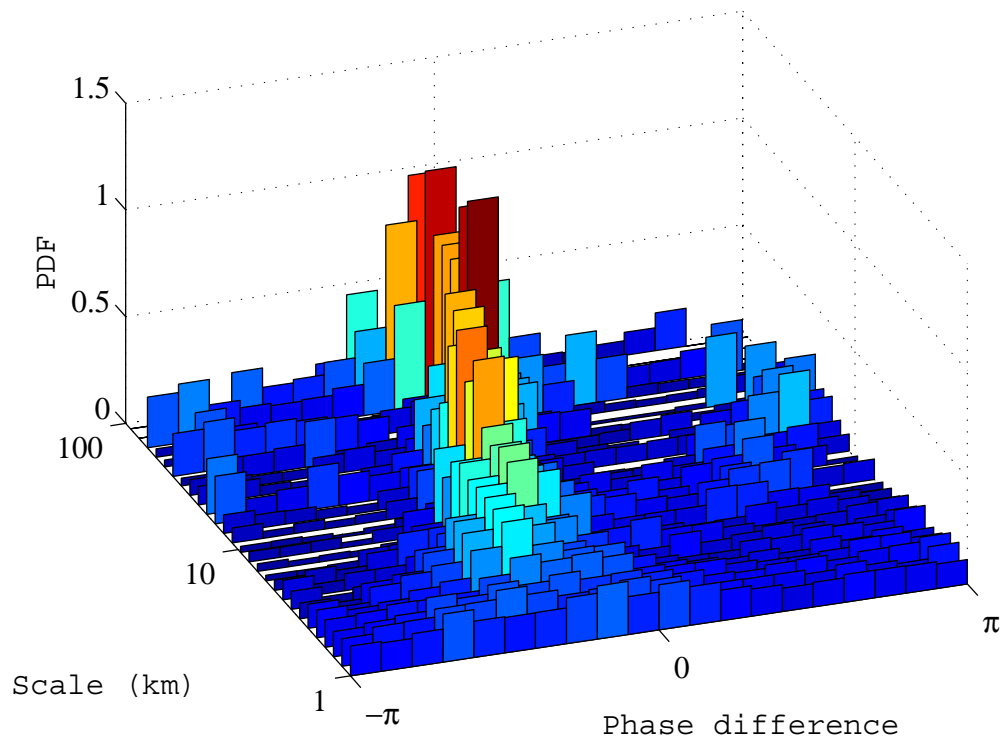
Figure 3.12. PDFs, plotted as bar graphs, of phase difference between temperature and fluorescence wavelet coefficients on the 200-dbar isobar. The color of each bar corresponds to its height, and spatial scale increases from front to back. The peak at a phase difference of zero indicates in-phase alignment of gradients, which is stronger at larger scales.
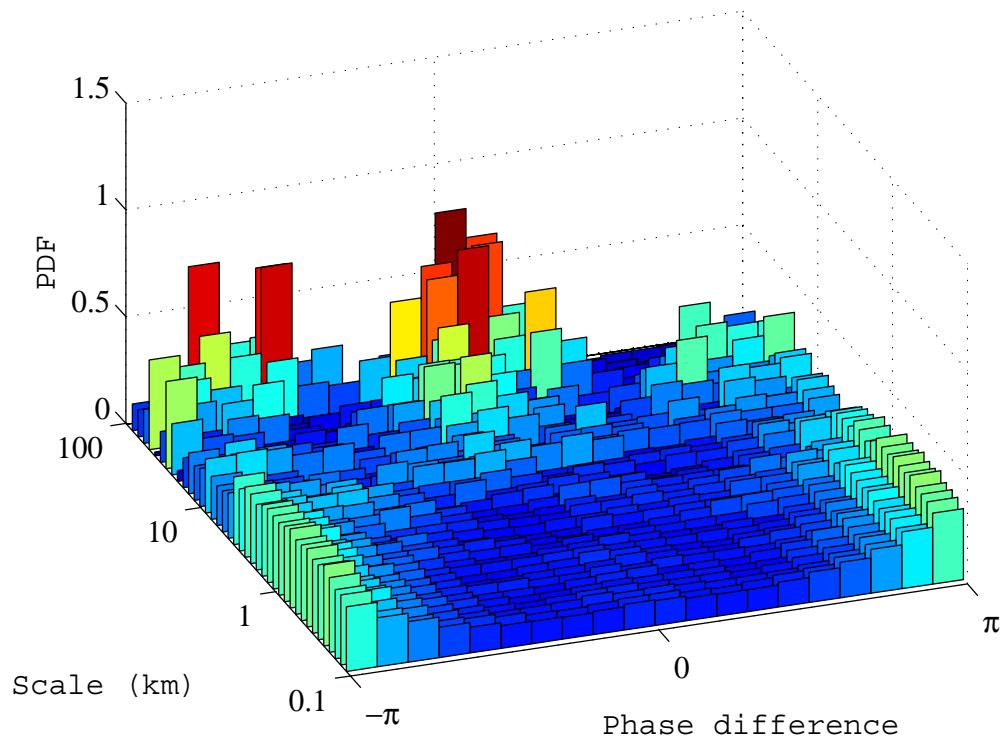
Figure 3.13. As in Fig. 3.12, for wavelet coefficients on the 50-dbar isobar. Gradients are aligned in-phase at large scales and out of phase (peaks at $\pm \pi$) at small scales.
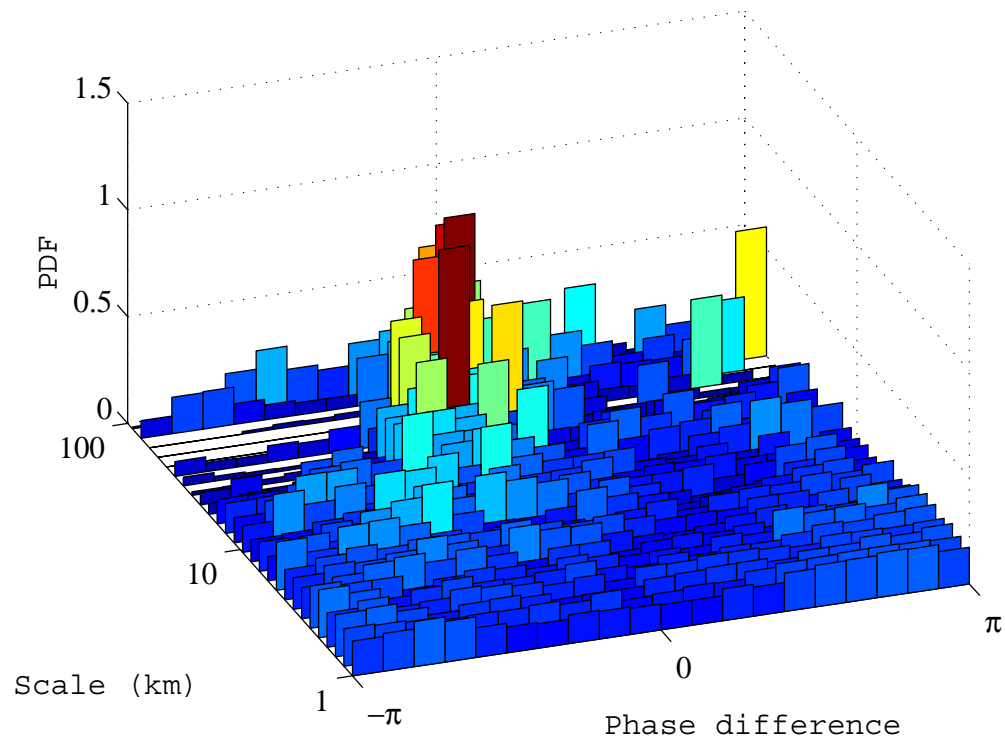
Figure 3.14. As in Fig. 3.12, for wavelet coefficients on the 25.5 kg/m^3 isopycnal. Large-scale alignment is evident both in-phase and (more weakly) out-of-phase.
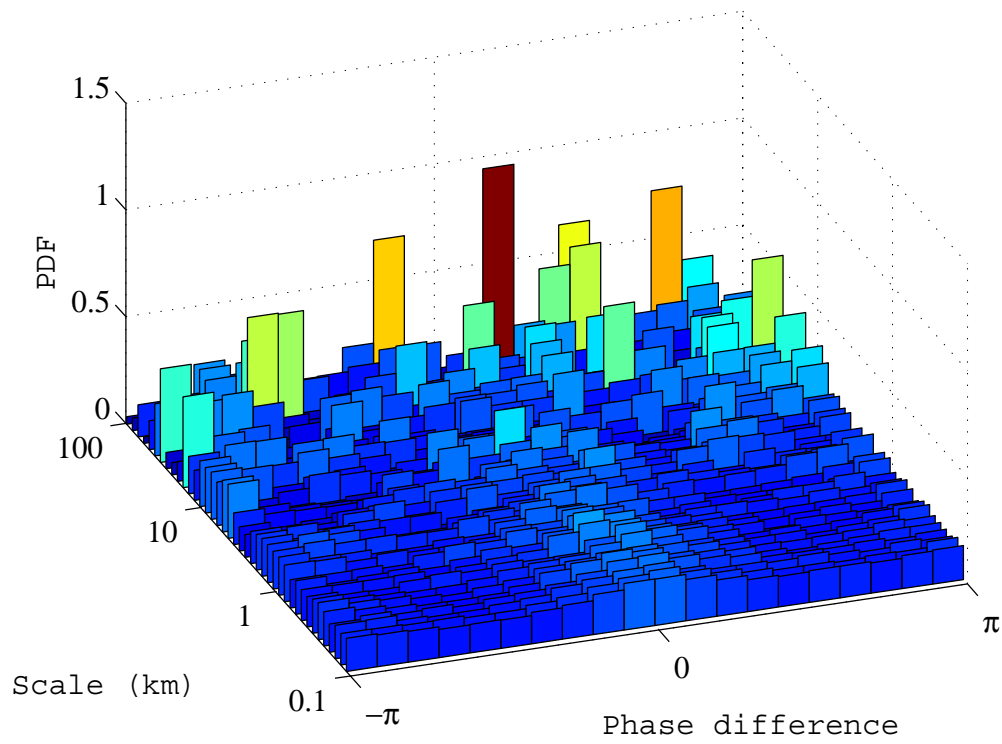
Figure 3.15. As in Fig. 3.12, for wavelet coefficients on the 24.8 kg/m^3 isopycnal. Small-scale alignment is the result of unintentional deviations from the isopycnal.
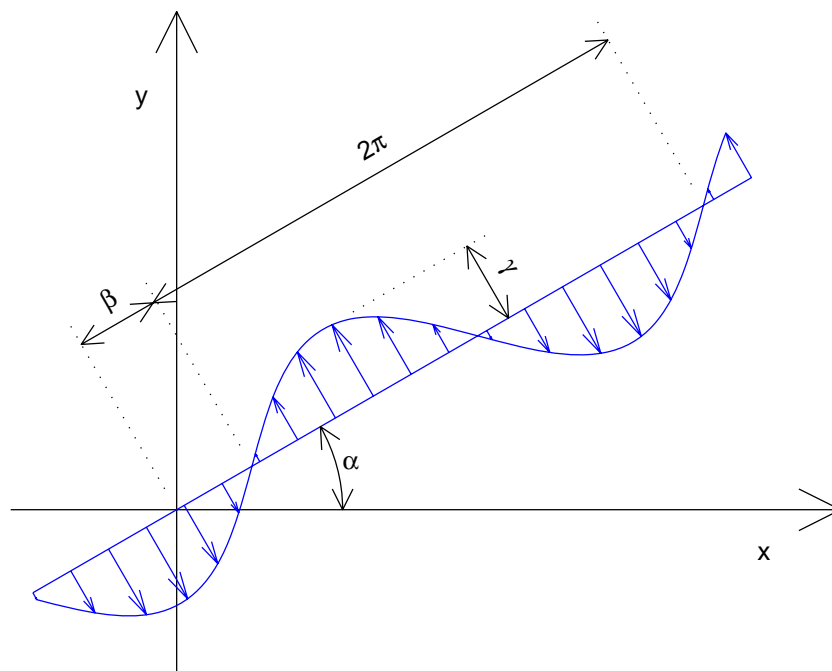
Figure 3.16. Velocity during a single iteration of the RW model flow. α is the angle or orientation of the renovating wave, β is its phase, and γ is the nondimensional amplitude (maximum particle displacement relative to the RW wavelength).
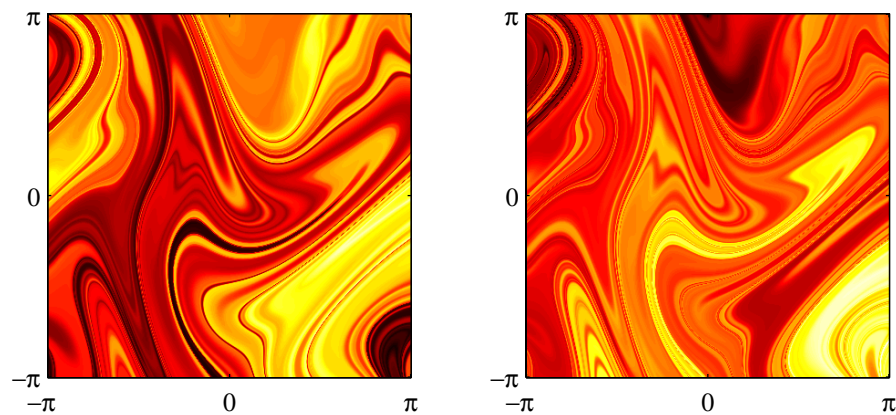
Figure 3.17. Two tracer fields stirred by an identical RW flow. γ is 0.8 and the number of iterations, N, is 70. Initial concentration gradients were uniform and equal in each case, but gradient direction differed by 90 degrees. Corresponding features in each panel are obvious; in some locations, the fields are in phase with each other, while in others they are out of phase.
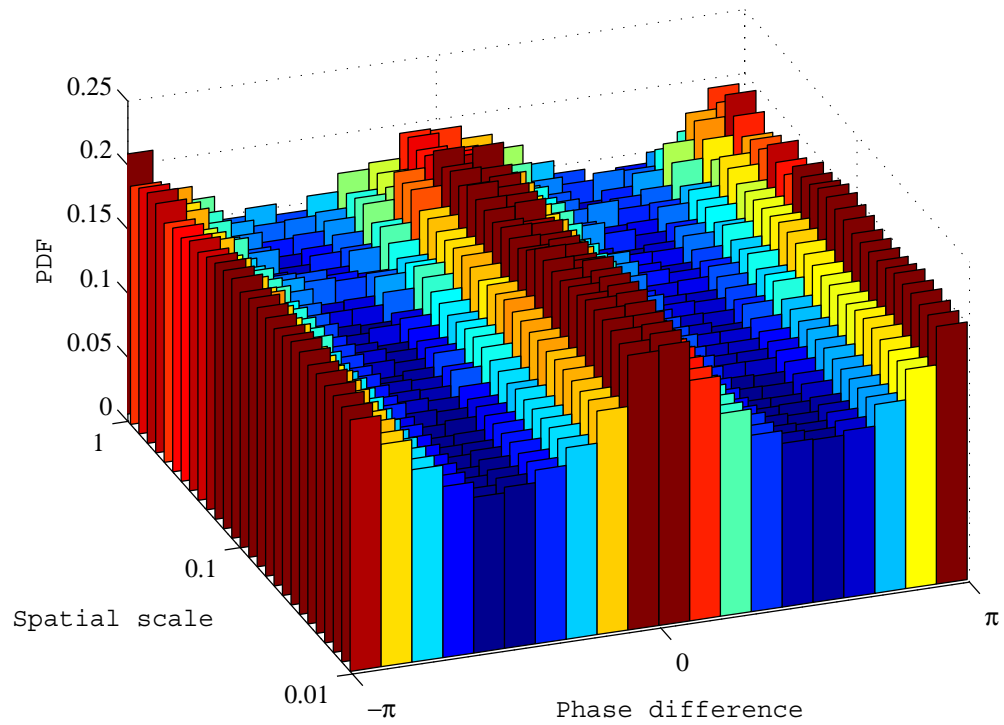
Figure 3.18. PDFs of phase differences, plotted as in Fig. 3.12, between wavelet coefficients for two tracer fields stirred by the same RW flow, showing both in-phase and out-of-phase alignment at all scales. As is Fig. 3.17, γ is 0.8 and N is 70.
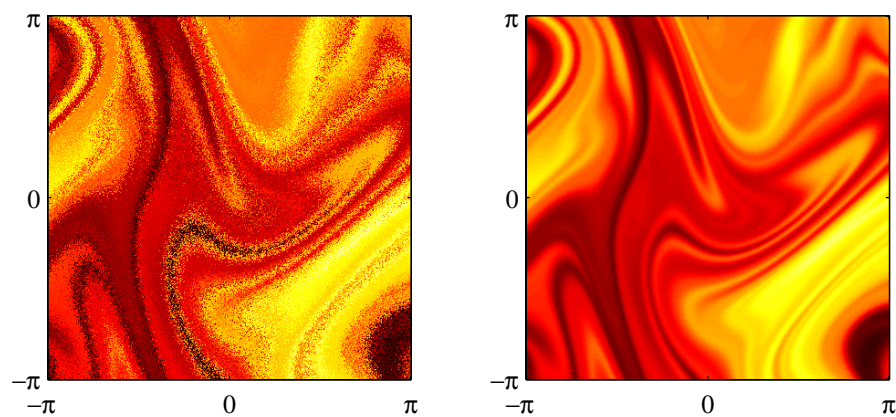
Figure 3.19. *Left panel*: the 'speckled' result of a single realization of the RW model with diffusion. The RW flow is retained from Fig. 3.17, and the tracer initial condition is that of Fig. 3.17, left panel. *Right panel*: final field with diffusion, obtained by averaging 100 realizations like the one in the left panel. γ is 0.8, N is 70, and δ is 0.024.
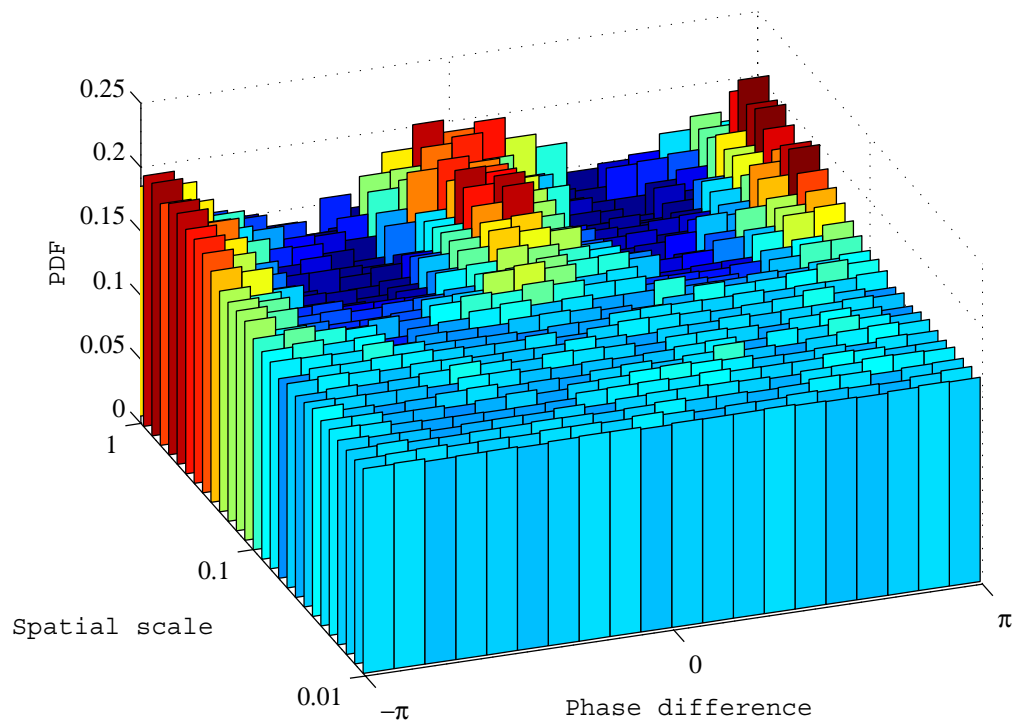
Figure 3.20. As in Fig. 3.18, for wavelet coefficients for two tracers stirred by the same RW flow, with turbulent diffusion. Alignment is suppressed below a spatial scale of 0.1. As in Fig. 3.19, γ is 0.8, N is 70, and δ is 0.024.
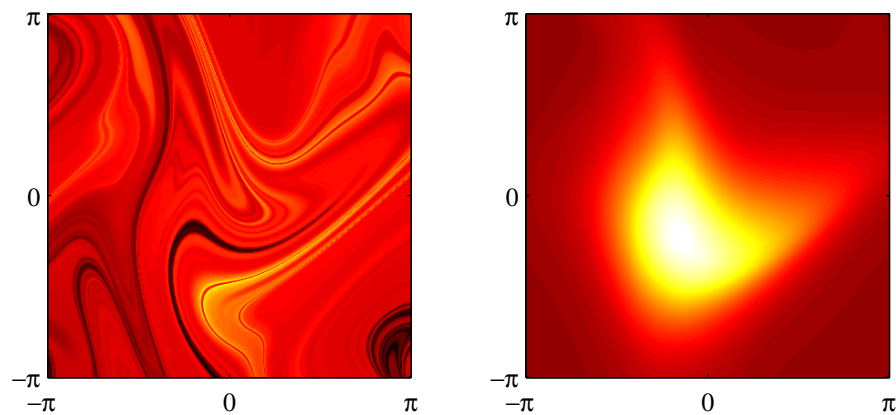
Figure 3.21. Reactive tracers subject to logistic growth. The RW flow is the same as in the earlier figures, and the initial condition is that of Fig. 3.17, left panel. The radius of the carrying capacity bump, R, is 2. Growth rate parameters for the two fields are (*left panel*) $\rho = 0.015$, and (*right panel*) $\rho = 0.25$. There is no diffusion.
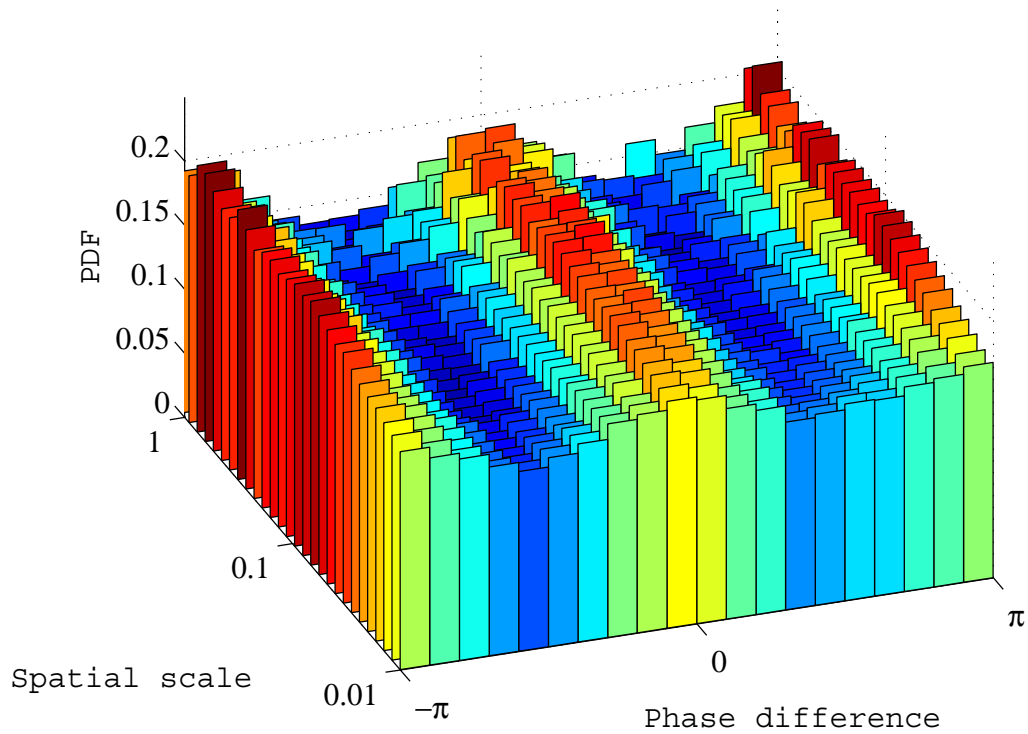
Figure 3.22. As in Fig. 3.18, for wavelet coefficients for two tracers stirred by the same RW flow, one of which is subject to logistic growth, with growth rate parameter $\rho = 0.015$, and a carrying capacity bump radius, R, of 2. The flow parameters and initial conditions are retained from the earlier figures. There is a slight decrease in alignment, especially at small scales.
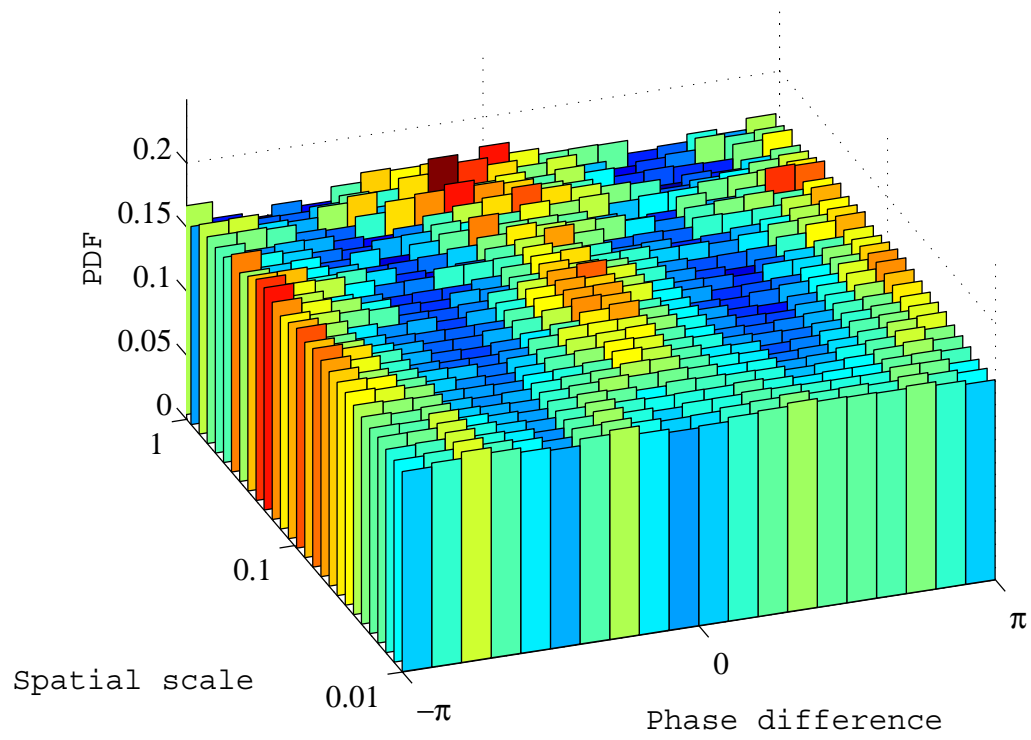
Figure 3.23. As in Fig. 3.22, but with a larger growth rate: $\rho = 0.25$. Alignment is weak, disappearing altogether at small scales.

Chapter 4

Glider Observations Along CalCOFI Line 93

4.1 Introduction

The physics and biology of the California Current have been studied extensively for the past several decades (e.g. Roemmich and McGowan, 1995, Chelton et al., 1982). A valuable dataset in furthering the understanding of the dynamics of this ecosystem is provided by the ongoing observations made by the California Cooperative Oceanic Fisheries Investigations (CalCOFI). The CalCOFI dataset is freely available to the scientific community for use without restriction; it complements the glider observations described here.

Research vessels began gathering data on physical and chemical properties of the ocean at CalCOFI stations in 1949. These stations are arranged in parallel lines, a few hundred kilometers in length, roughly perpendicular to the California coast. Many of the stations south of Point Conception have been occupied about 4 times per year since 1980, providing a picture of the seasonal to decadal variability of the hydrography and biology of the California Current System within the Southern California Bight.

Offshore, CalCOFI stations are spaced roughly 75 km apart; closer to the coast the spacing is half that (Fig 4.1). The long CalCOFI time series provides a context for interpreting data with higher spatial resolution from the same location. This report describes the use of an autonomous underwater glider to collect such high-resolution observations of temperature, salinity, and chlorophyll fluorescence, and presents the data and some findings resulting from it.

The glider measurements augment the CalCOFI dataset with information on small-scale physical and biological processes. Gliders are a recent development in oceanographic instrumentation technology, and the present study is among the first to undertake repeated missions by an autonomous vehicle along a transect of several-hundred-kilometer scale.

The observations were carried out using "Spray," an autonomous underwater glider (see Sherman et al., 2001). Vertical vehicle motion is buoyancy-controlled: oil is transferred between an external bladder and a reservoir inside the pressure case; pumping the oil into the bladder increases vehicle buoyancy, causing upward motion, and letting it back inside the hull decreases buoyancy, causing the vehicle to sink. Wings provide lift, allowing a glide angle through the water of approximately 20 degrees from the horizontal, and so producing horizontal motion. By repeatedly diving and resurfacing, the glider moves forward along a sawtooth trajectory, with a speed through the water of approximately 30 cm/s. The glider senses its orientation with a compass and a tilt sensor, and steers a course by changing its pitch and roll angles, which is done by shifting the position of internal ballast (battery packs). While at the surface at the end of each dive, mission commands are received and

data sent back to shore via the Iridium satellite network, and location is determined by GPS.

At the time of this writing, three Spray missions have been carried out along CalCOFI Line 93, intersecting the California coast near San Diego. The project is still underway, with more deployments planned in the future. The nominal profile depth was 500 meters, with occasional dives to 800 meters; average time per dive cycle was three hours. Temperature and salinity were measured with a pumped SeaBird CTD, and chlorophyll fluorescence with a Seapoint fluorometer. These data were recorded on the ascending leg of each dive only, with a sampling interval of 8 seconds.

The resulting sections have a horizontal resolution of roughly 3 km, and a vertical resolution of about 1 m. It is important to note that these sections do not represent a synoptic view. Each of the six sections (outgoing and return legs of the three missions) took about a month to complete. While many of the small-scale features observed may be thought of as "snapshots," temporal changes contribute significantly to the observed variability on larger scales, and each 700-km section represents a mixture of spatial and temporal variability.

Pressure, pitch, and heading were recorded on both ascending and descending legs, making it possible to compute distance and direction traveled horizontally through the water during a dive. From the difference between this dead reckoning and the actual displacement as determined from the GPS fixes before and after the dive, we can determine the current velocity, vertically averaged over the depth of the dive. Surface velocity estimates are available as well, because two GPS

fixes are obtained during each 3 to 5 minute period at the surface, one before data and command transmission, and one after. These estimates are noisy, however, due to the short time between fixes and the unknown effect of wind on the exposed portion of the vehicle.

The first mission lasted from April to June 2005, the second from December 2005 to February 2006, and the third from March to May 2006. During all deployments, Spray followed Line 93 quite closely (Fig. 4.1 shows the glider tracks from the three deployments and the locations of Line 93 CalCOFI stations plotted over a bathymetry map). The depth-averaged current velocities were generally less than half of the 30 cm/sec speed of the glider through the water, and were sufficiently correlated from dive to dive that automatic set correction was an effective strategy for maintaining a consistent course over ground.

4.2 Correcting Fluorescence Measurements

Fluorometers have been used to measure chlorophyll concentration in situ for decades (e.g. Lorenzen, 1966). One difficulty with this method is nonphotochemical quenching of fluorescence (e.g. Kiefer, 1973): when exposed to intense light, the fluorescence yield per cell is reduced. This effect manifests itself in the glider data as a spurious diurnal cycle in the near-surface chlorophyll concentration—during the day, chlorophyll fluorescence is suppressed in the brightly-lit surface water (Fig. 4.2, upper panel). Fluorescence is the only optical property we measured, so estimating the degree of quenching is a delicate problem.

In order to remove the effect of quenching from the fluorescence data, a few assumptions are required. First, we assume that, aside from the effect of quenching, fluorometer output is linearly proportional to chlorophyll concentration; this assumption is supported by laboratory calibrations. Second, we assume that the degree of quenching per cell depends only on irradiance, and not, for example, on other factors such as bulk chlorophyll concentration or species composition. Although the quenching response is not instantaneous, it is short compared to a day (e.g. Krause and Weis, 1991), and we assume a time lag of zero between light exposure and quenching response. This last approximation is supported by our observations of diurnal variations in the surface fluorescence, which are in phase with the daylight cycle (black line in Fig. 4.2). Setting aside additional sources of error such as chlorophyll "packaging" or self-shading and calibration uncertainty, these assumptions suggest a simple relationship between F, the chlorophyll concentration computed from the measured fluorescence, and true chlorophyll concentration, C:

$$F(\mathbf{x},t) = q(\phi(\mathbf{x},t))C(\mathbf{x},t).$$

Here, q is a multiplicative quenching function which depends only on irradiance, ϕ.

F is known at positions $\mathbf{x}$ and times t along the glider's path. $\phi(\mathbf{x},t)$ is not known, but we estimate the downward irradiance at the surface from the angle of the sun above the horizon, which is known as a function of $\mathbf{x}$ and t, and the transmission coefficient of the air-sea interface. Cloudiness and sea state are not well known, so their influence on the light field is neglected.

The rate of decay of light intensity with depth is not known explicitly, but we infer it from the observed decay of the covariance of the fluorescence signal with the estimated surface irradiance. Near the surface, most of the fluorescence variance is explained by the light cycle, but the relationship weakens with depth. The record is broken into four-day overlapping chunks, and the covariance of surface irradiance with measured fluorescence is computed for each 2-meter depth bin in the upper 50 meters of each chunk (below this depth, light intensity is low enough that nonphotochemical quenching is negligible). A light attenuation length for each chunk is determined by fitting an exponential function to these depth-dependent light-fluorescence covariance estimates. This attenuation length varies from chunk to chunk; in particular, the attenuation length is shorter over the continental shelf than in the deep ocean. For simplicity, we neglect the vertical variation of the attenuation length, treating it as constant with depth.

Having measured F and estimated ϕ, we still need to determine q. This function is unknown; we assume it has the form $q = \dfrac{k}{k + \phi(\mathbf{x}, t)}$, where k is a constant. This form is chosen as it is perhaps the simplest with the following properties: for $\phi = 0$ (darkness), $q = 1$, and there is no quenching: $F = C$; as light intensity increases, q decreases, approaching zero at a variable rate determined by k.

The best guess for the value of k is determined by requiring that the depth-weighted covariance of C and ϕ is zero. For each 2-meter depth bin and each guessed value of k, the covariance of C and ϕ is computed, and then multiplied by a weighting factor which decays with depth. The value of k is adjusted so that the

sum of the weighted covariances vanishes. The depth-dependent weighting of the beauty criterion used to estimate k emphasizes correction of fluorescence quenching near the surface, where it is strongest. While k is constant within each deployment, the estimate for k is independent from one deployment to the next. With ϕ normalized as a fraction of the downward irradiance just above the sea surface with the sun directly overhead, the value obtained for k is near 0.3 across all three deployments.

Dividing F by q, we obtain C, the estimated true chlorophyll concentration. Figure 4.2 compares a section of raw fluorescence data (top panel) from a segment near the beginning of the spring 2006 deployment with the corresponding quenching-corrected chlorophyll concentration (middle panel). The strong influence of the light cycle (black line) on fluorescence is largely eliminated by the correction procedure. The size of the correction is shown in the bottom panel. The results presented hereafter all make use of the corrected fluorescence data.

The first glider deployment ended when, after completing just over half of the return transect, a mechanical problem forced glider recovery. During this first deployment, the fluorometer was mounted facing outward from a hole in the instrument bay cowling, with flushing of the sensing volume accomplished by the movement of the glider through the water. In this mode of operation, the fluorometer is susceptible to biofouling. Such fouling compromises the fluorescence measurements from the shoreward leg of the first deployment, particularly from the latter half of this leg (see Fig. 4.5). The effect of the fouling was to cause the baseline voltage output of the fluorometer to increase at a steady,

exponential rate. We make a first-order correction for the effects of biofouling by subtracting the minimum fluorometer voltage output for each profile from all the measurements in that profile.

During the second and third deployments, the fluorometer was operated in a pumped mode, with a copper cap enclosing the sensing volume to inhibit algal growth. Seawater, pumped first through the CTD, then passed through a short tube to the intake of the fluorometer. These modifications eliminated biofouling during the latter deployments.

4.3   Comparison of Glider and CalCOFI Cruise Observations

4.3.1   Chlorophyll

The second of the three glider missions was carried out during the winter; the other two took place during the spring. Decades of CalCOFI measurements confirm that chlorophyll concentrations are typically higher, and that the deep chlorophyll maximum (DCM) is deeper and more pronounced, in springtime than in winter. Near-surface chlorophyll concentrations are also usually higher over the continental shelf then in the deeper water offshore. Figure 4.3 shows sections of chlorophyll, from the surface to 200 meters' depth, from all the CalCOFI cruise data collected along Line 93 during the months of January and February from 1980 until 2005. The corresponding sections from the months of April and May are presented in Fig. 4.4.

The lower right-hand panel in each of these figures is a section formed from the mean across all years (the average of all the other panels in the figure). The shoreward shoaling of the isopycnals (white lines in the figures) associated with the equatorward flow of the California Current, is, on the average, slightly more pronounced in the springtime than the winter. Not surprisingly, the mixed layer tends to be deeper in the winter, particularly offshore.

These same typical features of the large-scale chlorophyll and density structure are evident in the glider observations: Figures 4.5 – 4.7 are chlorophyll sections from the three deployments, with isopycnals overplotted as black lines. The sections are formed from data averaged into 2-meter depth bins, and the location of each dive is denoted by a hash mark at the top of the figure. The red stick plots near the bottom of each section indicate vertically averaged current velocities for each dive. See the Introduction to this chapter for a description of the derivation of these velocities.

In addition to the large-scale structure revealed by the CalCOFI cruises, the glider sections capture smaller-scale features of the chlorophyll field. During each deployment, the location of the DCM tended to coincide with that of a particular isopycnal; the potential density at the DCM was approximately 1024.7 kg/m^3 in the winter (Fig. 4.6), and 1024.9 kg/m^3 in the spring (Figs. 4.5 and 4.7). These values are not constant: as can be seen from the CalCOFI sections (Figs. 4.3 and 4.4) the density at the DCM varies from year to year. The relationship between the depth of the DCM and that of nearby isopycnals is robust not only on the ~100-km scales resolved by CalCOFI cruises, but also on scales down to the 3-km resolution of the

glider measurements; small-scale coherence of the DCM and isopycnals is obvious, for example, in the internal wave disturbance observed to the west of longitude -123° on the return transect of the last glider deployment (Fig. 4.7, bottom panel).

Upward displacement of isopycnals tends to produce an increase in chlorophyll concentration, as nutrient-rich water moves to a more brightly lit depth. One clear example of this occurring may be found near longitude -122° on the return transect of the second glider deployment (Fig. 6, bottom panel). A distinct local bloom is sandwiched between the 1024.6 kg/m^3 isopycnal and the uplifted 1024.4 kg/m^3 isopycnal.

4.3.2 Salinity

Winter and spring CalCOFI sections of salinity from Line 93—Figs. 4.8 and 4.9 show salinity and isopycnals in the upper 500 meters—reveal that salinity increases with depth. The halocline tends to be shallower near the coast than offshore, typically lying between 100 and 200 meters' depth. Beneath the halocline, salinity increases toward the coast. The resulting slope of the isohalines is largest near the coast, and is generally larger in the spring than the winter.

As is the case with the chlorophyll distribution, this large-scale structure is reproduced in the glider salinity observations (Figs. 4.10 – 4.12). On smaller scales, the glider measurements reveal that sharp, density-compensated temperature/salinity fronts occur frequently, not only in the mixed layer, but deeper as well. The front near -122° longitude from the first glider deployment (Fig. 4.10) is an example. The width of the front is only a few km, and it is evident on both the outward and return

transects. In the mixed layer and the pycnocline the inshore side of the front is fresher, while below the pycnocline the inshore side is saltier.

Of the numerous other examples of sudden changes in salinity, perhaps the most striking is the high-salinity tongue between –120° and –119° longitude on the return transect of the winter deployment (Fig. 4.11, bottom panel). The edges of this warm salty intrusion are too sharp to be resolved by the 3-km spacing of the glider profiles, and at the top, a change of half a PSU occurs over a vertical span of less than 10 meters. Though the salinity feature gives the appearance of having pushed up from the salty water below, its effect on density is almost perfectly compensated by temperature (note the undisturbed isopycnals crossing the feature in Fig. 4.11), suggesting that it results rather from horizontal motions. The water forming the feature is high in chlorophyll: Figure 4.13 shows chlorophyll fluorescence in the region (color), with salinity contours plotted as black lines over the top. The chlorophyll color scale is logarithmic, to emphasize the small chlorophyll concentrations at depth, rather than the much larger ones in the DCM layer above. The salinity fronts that define the edges of the feature coincide precisely with sudden changes in chlorophyll. This pattern likely arose when warm, salty, high-chlorophyll water, initially distant, was carried by prevailing currents into close proximity with cooler, fresher water that was lower in chlorophyll; it is worth noting that the inshore edge of the intrusion occurs coincident with a strong southward jet in vertically averaged current velocity (Fig. 4.11). The resulting strong gradients in salinity, temperature, and chlorophyll fluorescence are aligned with each other, a behavior discussed at length in Chapter 3 of this dissertation.

4.4   Deep Chlorophyll Maximum Response to Vertical Displacement

As noted in Section 4.3.1, uplifted isopycnals tend to produce elevated chlorophyll concentrations.   As nutrient-rich water moves toward the surface, the increase in light stimulates phytoplankton growth.   In order to investigate the relationship between the chlorophyll concentration and isopycnal displacement statistically, a measure of isopycnal displacement is required.

A related quantity is the potential density anomaly, which we define as:

$$\sigma_t'(x,z) = \sigma(x,z) - \overline{\sigma_t(x,z)}.$$

Here, $\sigma(x,z)$ is the measured potential density at longitude x and depth z, and $\overline{\sigma_t(x,z)}$ is the mean density at that longitude, depth, and time of year (t).   Like isopycnal displacement, density anomaly describes vertical excursion, but rather than the change in depth of a given density surface, it is the change in density at a given depth.   A positive density anomaly indicates upward displacement (water is denser than expected for the given depth), and a negative density anomaly indicates downward displacement.

The mean density fields as functions longitude and depth,   and $\overline{\sigma_{spring}(x,z)}$, are estimated from ~20 years of CalCOFI data, and are shown as the white lines in the lower right-hand panels of Figs. 4.3 and 4.4 respectively.   The relatively coarse resolution afforded by the spacing of CalCOFI stations and sampling depths easily captures the mean density field, with isopycnals sloping

smoothly upward toward the coast. Between stations and sampling depths, $\overline{\sigma_t(x,z)}$ is computed by 2-dimensional linear interpolation. For the first and third glider deployments, density anomaly is computed from $\overline{\sigma_{spring}(x,z)}$, and for the second deployment, from   .

Figure 4.14 is a scatter plot of density anomaly at the DCM versus density there. For every dive on all three missions, except for those from the return transect of the first deployment, which are avoided due to fluorometer biofouling, the depth of the DCM is determined, and a point plotted indicating the potential density and density anomaly at that depth. Each of the 1211 profiles is represented by a point, and each point is colored to indicate the chlorophyll concentration at the DCM. The relationship between density anomaly and chlorophyll concentration is clear; points nearer the top of the plot are redder: higher density anomalies (upward displacement) at the DCM go along with higher chlorophyll concentrations there.

It is obvious from Figs. 4.5-4.7 that the depth of the DCM largely tracks the depth changes of nearby isopycnals (see Section 4.3.1). However, fluctuations in the depth of the DCM are generally not quite as large as isopycnal fluctuations. Figure 4.14 reveals a correlation between density and density anomaly at the DCM: when the density anomaly at the DCM is greater, the density there tends to be greater as well. When local isopycnals are displaced upward, the DCM moves a little deeper, to a higher-density surface, and when they are displaced downward, the DCM moves shallower. To first order, the depth of the DCM does mirror that of

nearby density surfaces, but there is a bias toward smaller changes in the depth of the DCM.

This behavior may be explained as the response of phytoplankton comprising the DCM to changes in irradiance. As water moves upward, carrying the DCM with it, the DCM responds to the brighter light by moving downward across isopycnals, into more nutrient-rich water. Similarly, the response of the DCM to downward motion, into a darker environment, is to move upward into less dense, more brightly lit water.

The correspondence between chlorophyll concentration at the DCM and density anomaly, and between density and density anomaly at the DCM, are only demonstrated in Fig. 4.14 for all three glider mission taken together. However, the relationships are robust; they hold independently for each of the missions independently as well.

4.5 Summary

Glider observations along CalCOFI Line 93 have suggested certain features which are likely typical of the small-scale physical properties and chlorophyll distribution in the region. Sharp, density-compensated temperature-salinity fronts are common, with changes of 0.1-0.5 PSU occurring over the span of just a few kilometers. Such fronts occur in the mixed layer and pycnocline, but most striking are the fronts in the weakly stratified layer beneath. Sudden changes in chlorophyll concentrations occur at some of these fronts.

Vertical motions influence the depth of the DCM, and the chlorophyll concentration there. Upward motion, which carries nutrients closer to the surface, tends to induce phytoplankton growth, and this is shown to be the case at the DCM, where upward displacement of isopycnals is associated with enhanced chlorophyll concentration. Observations suggest that after the DCM is raised or lowered by vertical motion, it tends to shift back toward its original depth: fluctuations in the DCM depth largely track fluctuations in the depth of isopycnals at the same depth, but the former tend to be slightly smaller than the latter.
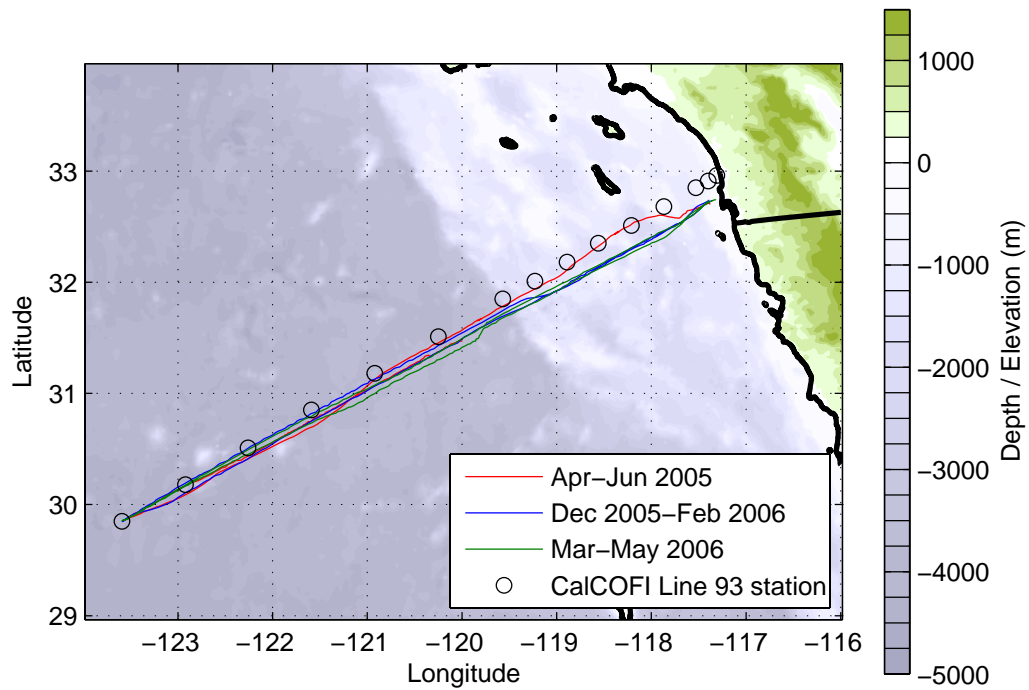
Figure 4.1. Tracks from the three glider deployments, and CalCOFI Line 93 station locations. The first deployment (red) ended after completion of half of the return transect. The track from the second deployment is plotted in blue, and that from the third in green.
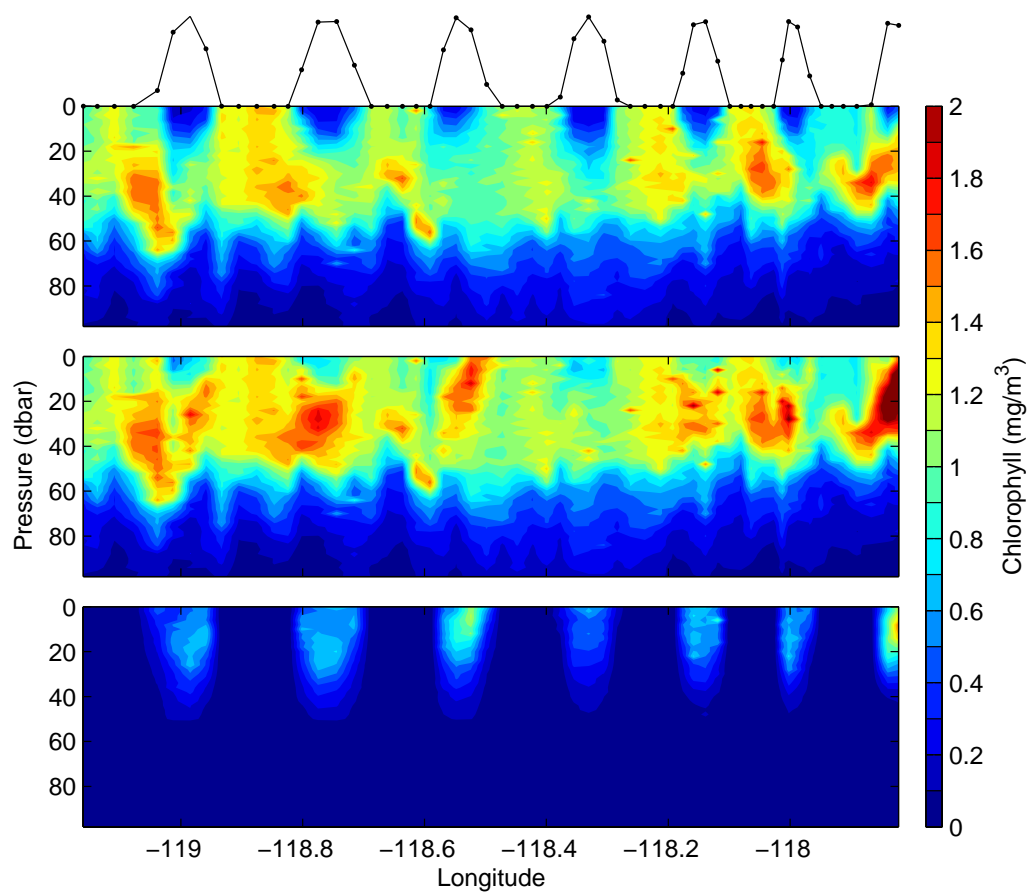
Figure 4.2. A week of chlorophyll fluorescence data from the outward leg of the spring 2006 glider deployment. *Top panel:* raw fluorescence measurments converted to chlorophyll concentration. *Middle panel:* the same section after correction for nonphotochemical quenching. *Bottom panel:* the correction. The black line at the top shows relative light intensity, based on the position of the sun. Black dots indicate the location of each dive.
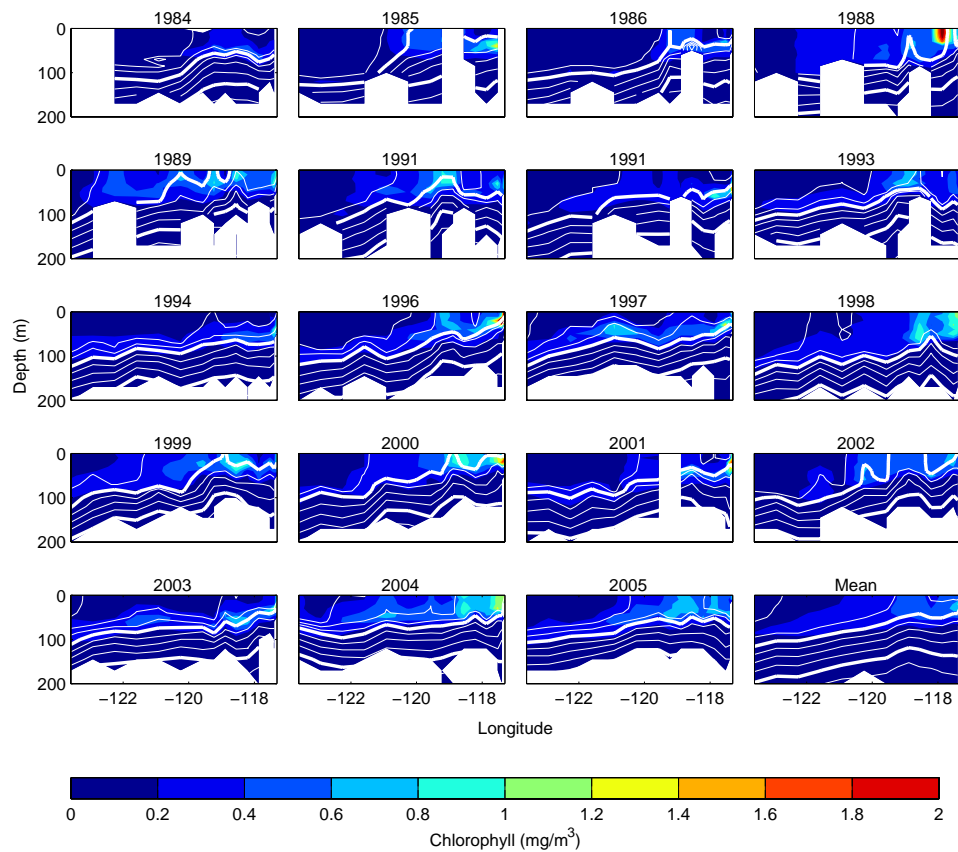
Figure 4.3. Winter CalCOFI chlorophyll sections from Line 93. These sections represent all the data collected during the months of January and February, between 1980 and 2005. White lines are 0.25 kg/m^3 contours of potential density. Contours denoting the 1025 and 1026 kg/m^3 isopycnals are thicker. Sections are labeled by year; two cruises took place in winter 1991, one each in January and February. The section in the lower right-hand panel is formed from the average of all the others.
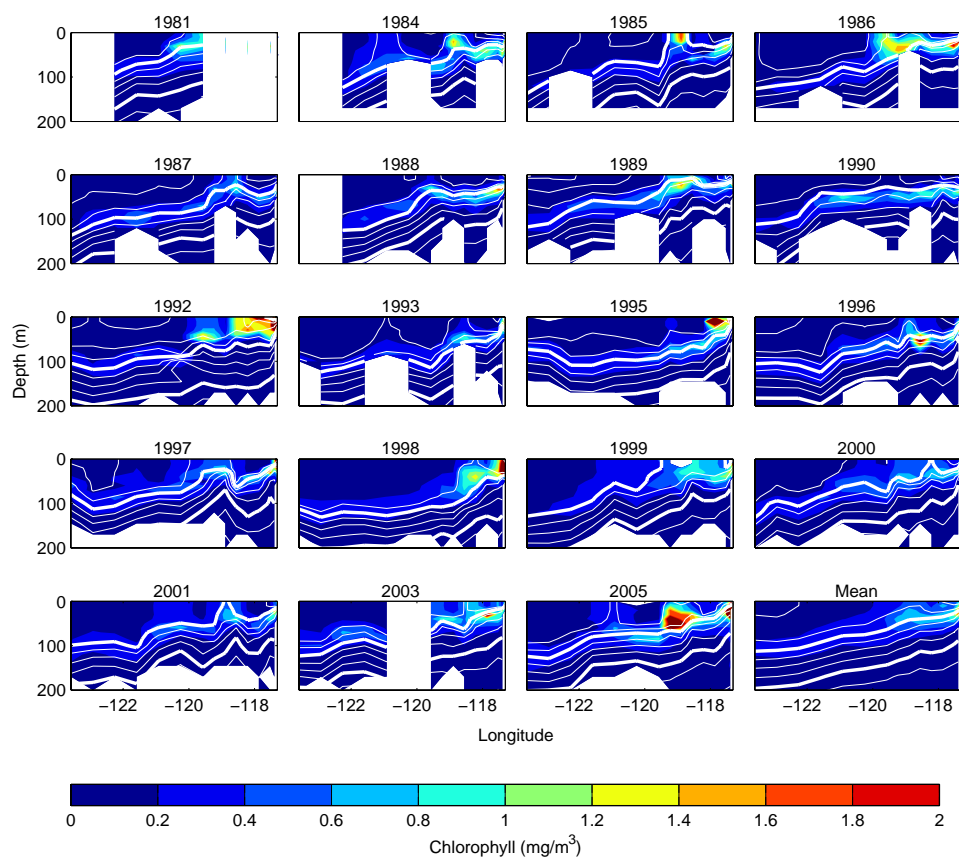
Figure 4.4. As in Fig. 4.3, but for CalCOFI observations collected along Line 93 during the spring (April and May).
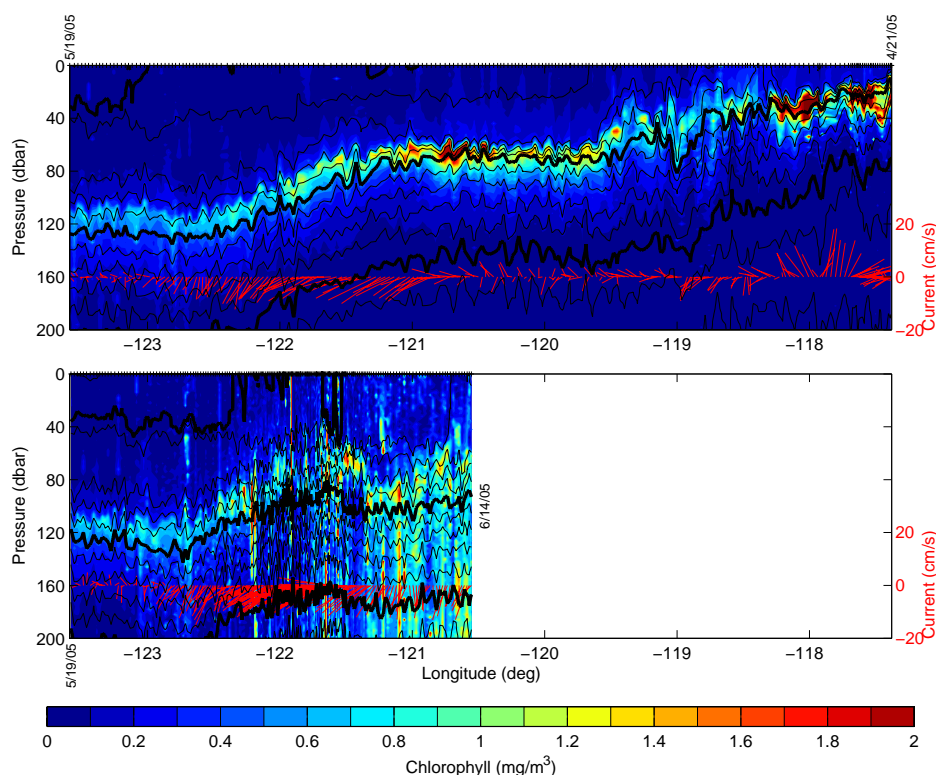
Figure 4.5. Chlorophyll sections (upper 200 meters only) from the first glider deployment. Black lines are contours of potential density, spaced every 0.2 kg/m^3, with the 1024, 1025, and 1026-kg/m^3 isopycnals denoted by thicker lines. These sections may be compared with the springtime CalCOFI observations (Fig. 4.3). The glider began near San Diego and proceeded to the end of CalCOFI Line 93 (right to left in the upper panel of the figure), and then reversed course, repeating the transect (left to right in the lower panel). The mission ended on June 19 near –120° longitude, due to a mechanical failure, but the last 5 days of fluorescence data are not shown, as severe biofouling (already obvious in the portion of the return transect shown in the lower panel above) obscured all useful information about chlorophyll during that time. The location of each dive is denoted by a black hash mark at the top of each panel, and the ends of each section are labeled by date. The red stick plots near the bottom of each panel show inferred current velocity (see text). In these plots, the horizontal and vertical directions represent along- and across-track velocity components, respectively. An upward pointing stick indicates a current flowing into the page, a downward stick one flowing out of the page.
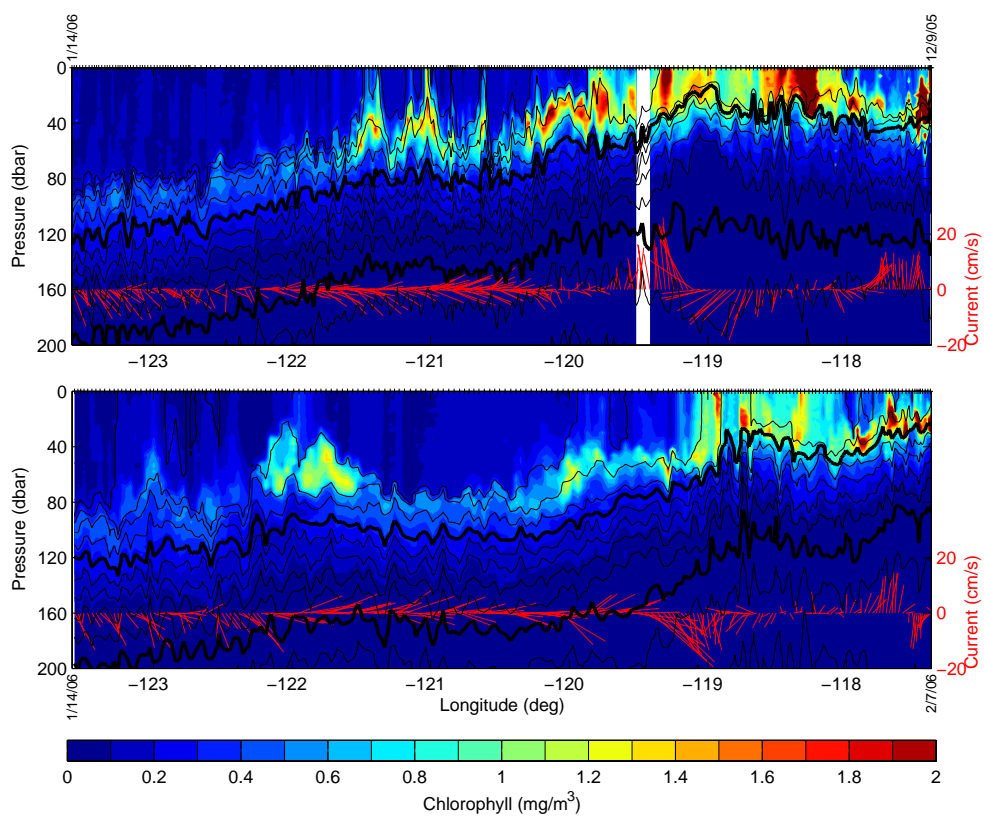
Figure 4.6. As in Fig. 4.5, for the second glider deployment. This was a wintertime deployment, and the sections can be compared to the CalCOFI observations in Fig. 4.4. For three dives on the outward transect (upper panel) the fluorometer was inadvertently turned off.
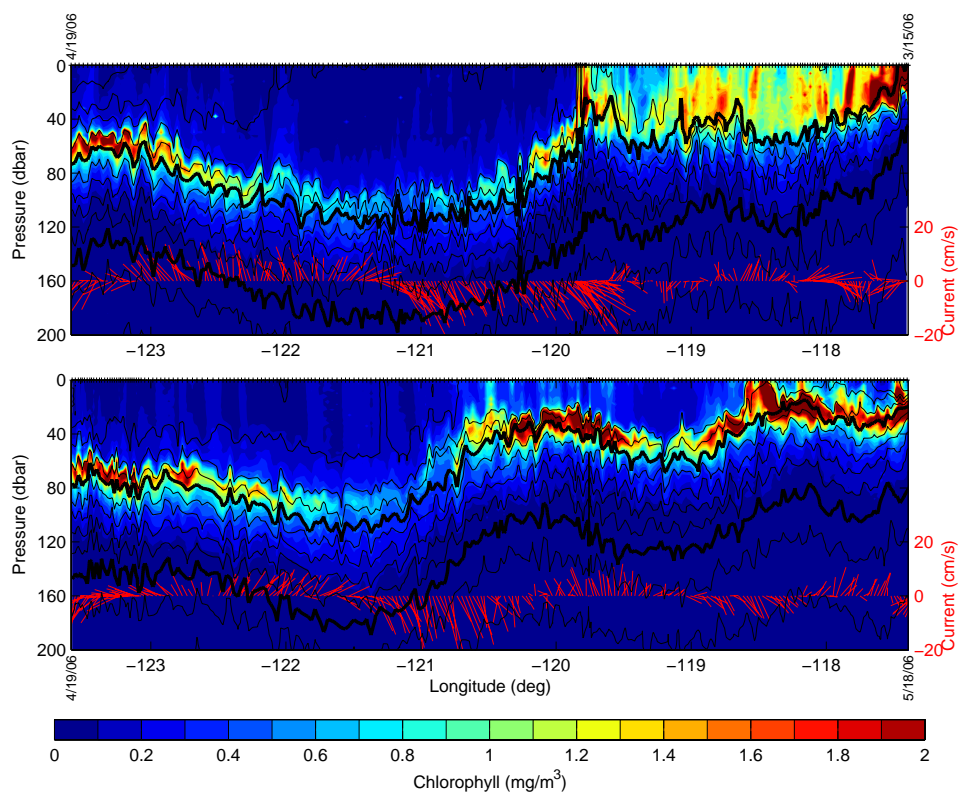
Figure 4.7. As in Fig. 4.5, for the third glider deployment. Compare to Fig. 4.3.
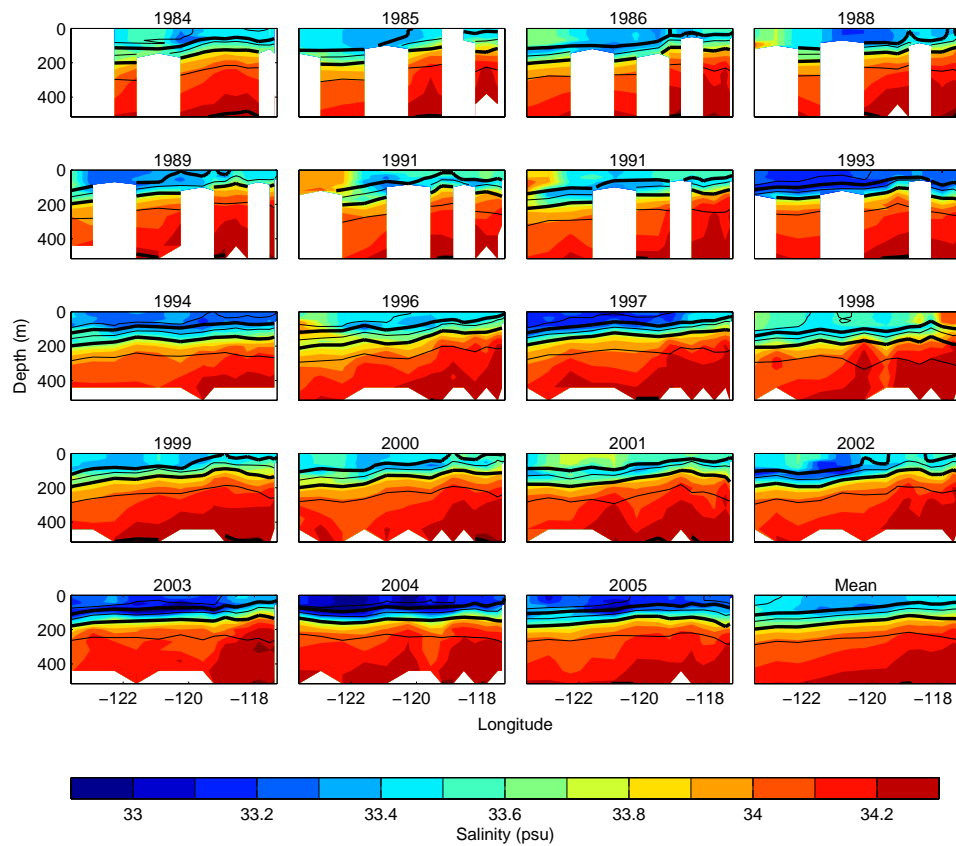
Figure 4.8. As in Fig. 4.3, but for winter CalCOFI salinity sections, rather than chlorophyll. Instead of only 200, the upper 500 meters are shown, and the black lines are contours of potential density spaced every 0.5 kg/m^3, with heavier lines for 1025 and 1026 kg/m^3.
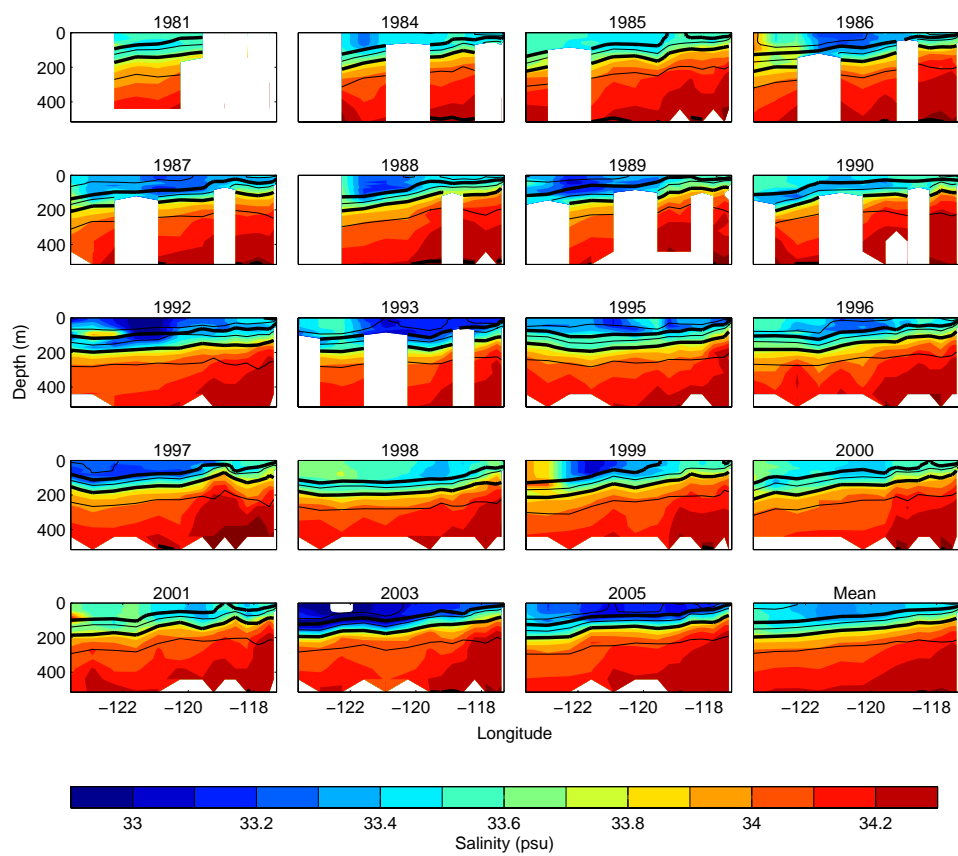
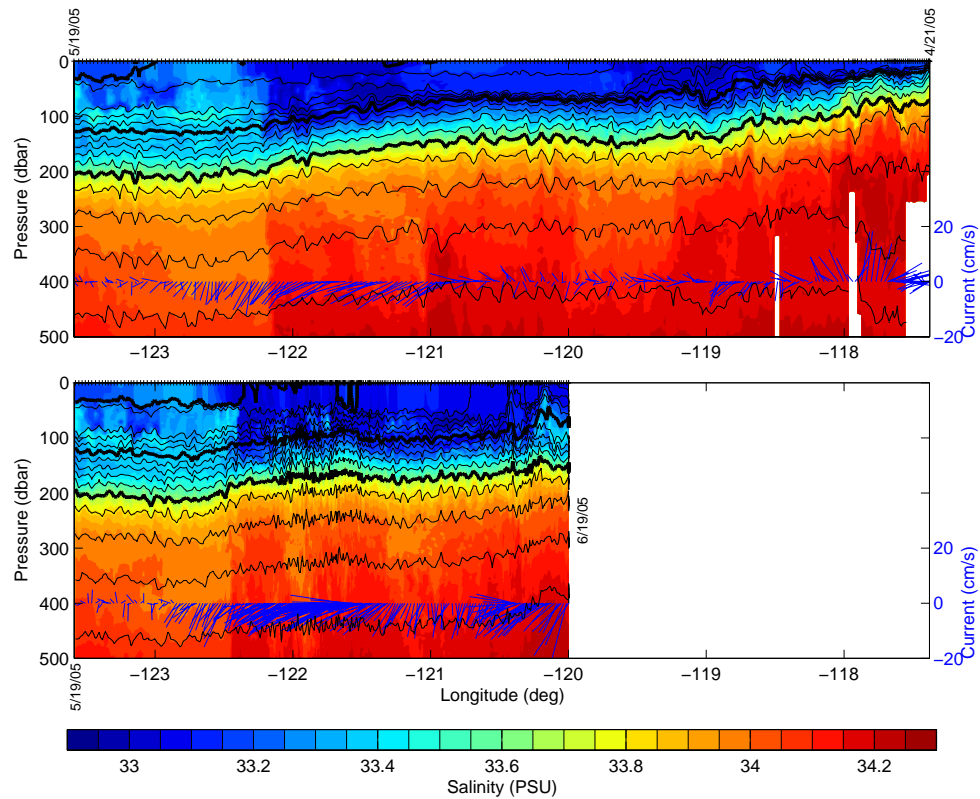**Figure 4.9.** As in Fig. 4.8, for springtime CalCOFI sections (April and May).

Figure 4.10. Salinity sections from the first glider deployment. Layout is identical to Fig. 4.5, except that the full 500-meter section is shown, rather than only the upper 200 meters. This was a springtime deployment, and the sections may be compared to Fig. 4.9.
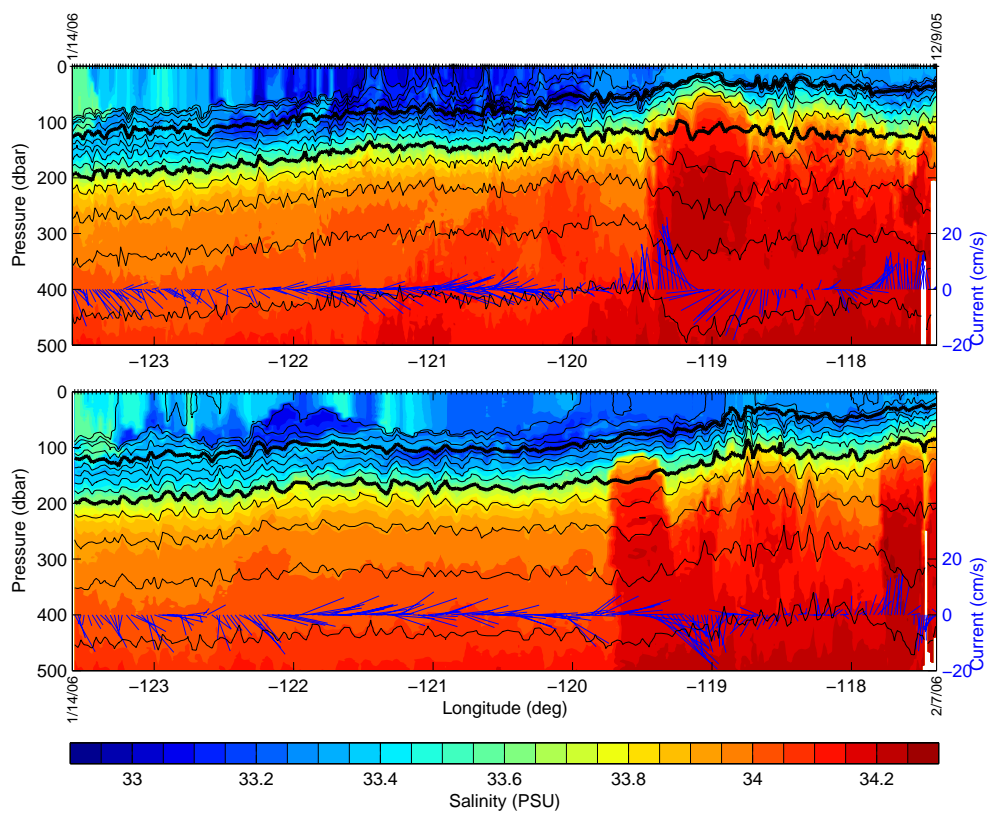
Figure 4.11. As in Fig. 4.10 for the second glider deployment. Compare to Fig. 4.8 (winter CalCOFI observations).
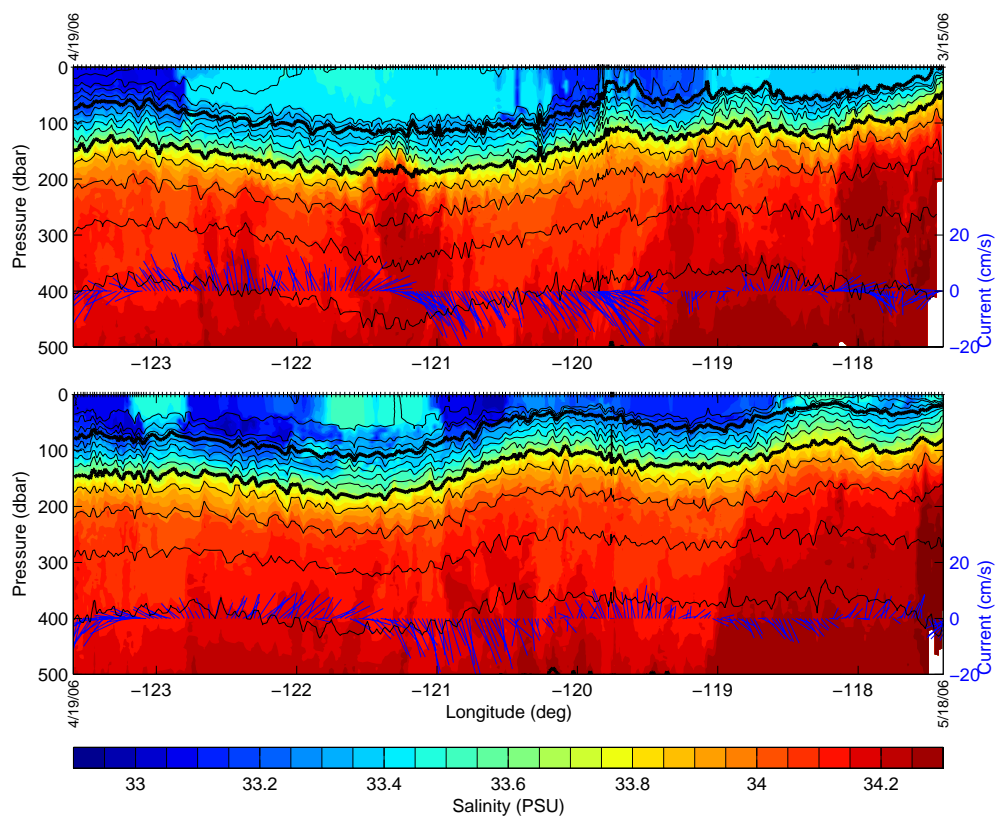
Figure 4.12. As in Fig. 4.10 for the third glider deployment. Compare to Fig. 4.9.
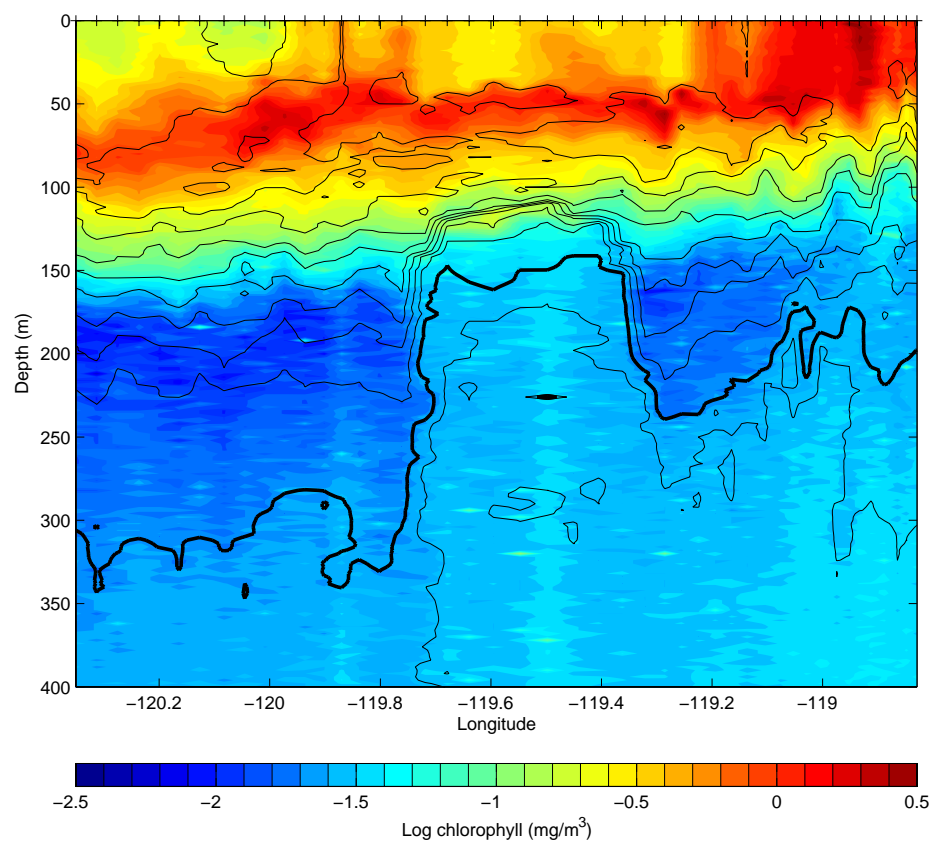
Figure 4.13. Salinity contours plotted over chlorophyll fluorescence for a density-compensated salinity intrusion from the return transect of the second glider deployment. Salinity contour spacing is 0.1 PSU, with a thicker line for the 34 PSU contour. Chlorophyll is displayed on a logarithmic scale to emphasize the small chlorophyll concentrations below the DCM layer.
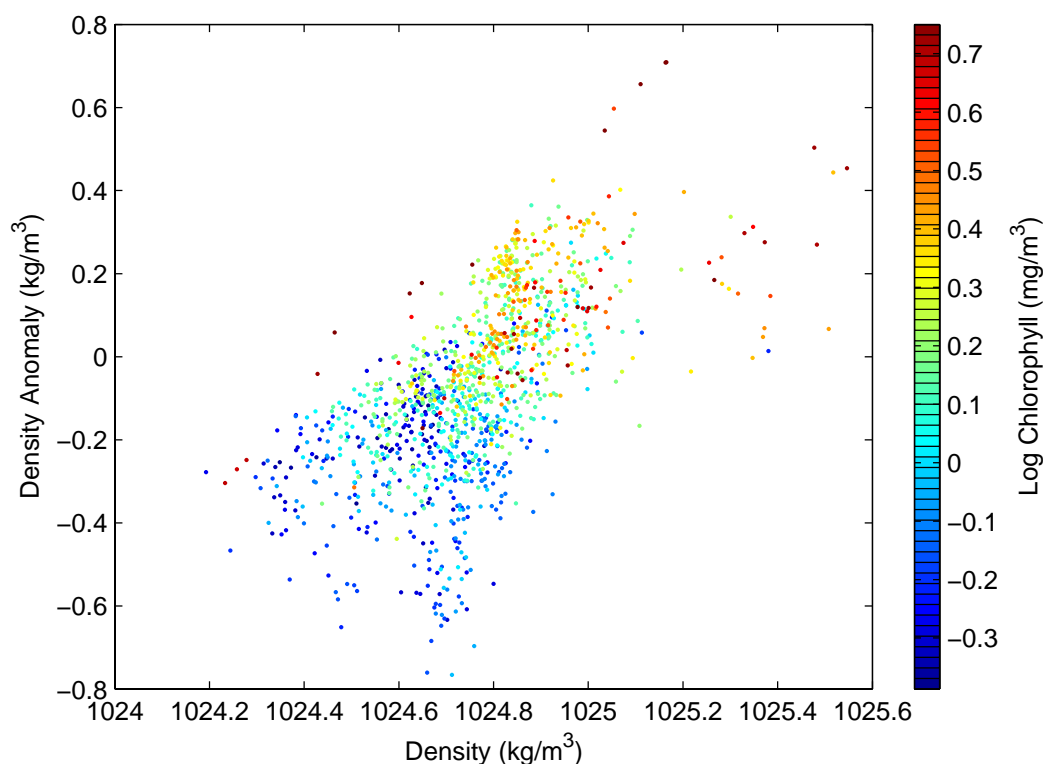
Figure 4.14. For each of the dives in all three glider deployments, density anomaly at the DCM is plotted versus potential density there as a point whose color is scaled by the chlorophyll concentration at the DCM. The color scale is logarithmic to de-emphasize the few profiles with very high chlorophyll concentrations. Density anomaly is defined as the difference between the measured density at the location of the DCM and the density expected at that location and depth on the basis of historical CalCOFI data. When isopycnals are displaced upward, density anomaly is positive; when downward, negative. The correlation between density and density anomaly indicates that when the DCM is displaced upward (downward) by vertical motion, it moves deeper (shallower), into denser (lighter) water. The larger chlorophyll concentrations toward the top of the plot indicate that positive density anomalies (isopycnals displaced upward) are associated with higher chlorophyll concentrations.

References

Abraham, E.R., 1998. The generation of plankton patchiness by turbulent stirring. Nature 391, 577-580.

Batchelor, G.K., 1952. The effect of homogenous turbulence on material lines and surfaces. *Proceedings of the Royal Society of London*, A, 213, 349-366.

Bishop, J.K.B., 1999. Transmissometer measurement of POC. Deep-Sea Research I 46, 353–369.

Bricaud, A., Morel, A., Prieur, L., 1983. Optical efficiency factors of some phytoplankters. Limnology and Oceanography 28, 816–832.

Briscoe, M.G., 1977. Gaussianity of internal waves. Journal of Geophysical Research, 82, C15, 2117-2126.

Chelton, D.B., Bernal, P.A., McGowan, J.A., 1982. Large-scale interanual physical and biological interaction in the California Current. Journal of Marine Research, 40, 4, 1095-1125.

Childress, S., Gilbert, A.D., 1995. Stretch, Twist, Fold: The Fast Dynamo. Springer-Verlag Lecture Notes in Physics: Monographs, 37.

Criminale, W.*O*., Winter, D.F., 1974. The stability of steady-state depth distributions of marine phytoplankton. The American Naturalist 108 (963), 679–687.

Cullen, J.J., 1982. The deep chlorophyll maximum: comparing vertical profiles of chlorophyll a. Canadian Journal of Fisheries and Aquatic Sciences 39, 791–803.

Cullen, J.J., Lewis, M.R., 1988. The kinetics of algal photoadaptation in the context of vertical mixing. Journal of Plankton Research 10 (5), 1039-1063.

Cushing, D.H., 1961. Patchiness. *ICES, Symposium on Zooplankton Production*, 14, 15.

Daubechies, I., 1992. Ten Lectures on Wavelets. *CBMS-NSF Regional Conference Series in Applied Mathematics (Society for Industrial and Applied Mathematics, Philadelphia, 1992).*

Denman, K.L., 1976. Covariability of chlorophyll and temperature in the sea. Deep-Sea Research 23, 539-550.

Denman, K.L., Okubo, A., Platt, T., 1977. The chlorophyll fluctuation spectrum in the sea. Limnology and Oceanography 22, 1033–1038.

Denman, K.L., Platt, T., 1976. The variance spectrum of phytoplankton in a turbulent ocean. Journal of Marine Research 34, 593-601.

Eckart, C., 1948. An analysis of the stirring and mixing processes in incompressible fluids. Journal of Marine Research, 7, 265-275.

Edwards, C.A., Powell, T.A., Batchelder, H.*P*., 2000. The stability of an NPZ model subject to realistic levels of vertical mixing. Journal of Marine Research 58, 37–60.

Falkowski, P., Kiefer, D.A., 1985. Chlorophyll *a* fluorescence in phytoplankton: relationship to photosynthesis and biomass. Journal of Plankton Research 7 (5), 715-731.

Fasham, M.J.R., Ducklow, H.W., McKelvie, S.M., 1990. A nitrogen-based model of plankton dynamics in the oceanic mixed layer. Journal of Marine Research 48, 591–639.

Fennel, K., Boss, E., 2003. Subsurface maxima of phytoplankton and chlorophyll: steady state solutions from a simple model. Limnology and Oceanography 48 (4), 1521–1534.

Ferrari, R., Rudnick, D.L., 2000. Thermohaline variability in the upper ocean. Journal of Geophysical Research, 105, 16,857-16,883.

Franks, P.J.S., Wroblewski, J.S., Flierl, G.R., 1986. Behavior of a simple plankton model with food-level acclimation by herbivores. Marine Biology 91, 121–129.

Hardy, A.C., 1936. Observations on the uneven distribution of oceanic plankton. Discovery Reports 11, 511-538.

Iselin, C.O., 1939. The influence of vertical and lateral turbulence on the characteristics of the waters at mid-depths. Trans. of the Amer. Geophys. Union, 1939, 414-417.

Jamart, B.M., Winter, D.F., Banse, K., Anderson, G.C., Lam, R.K., 1977. A theoretical study of phytoplankton growth and nutrient distribution in the Pacific Ocean off the northwestern US coast. Deep-Sea Research 24, 753–773.

Jenkins, W.J., Goldman, J.C., 1985. Seasonal oxygen cycling and primary production in the Sargasso Sea. Journal of Marine Research 43, 465–491.

Kiefer, D.A., 1973. Fluorescence properties of natural phytoplankton populations. Marine Biology, 22, 3, 263-269.

Kitchen, J.C., Zaneveld, J.R.V., 1990. On the noncorrelation of the vertical structure of light scattering and chlorophyll a in Case I waters. Journal of Geophysical Research 95 (C11), 20,237–20,246.

Krause, G.H., Weis, E., 1991. Chlorophyll fluorescence and photosynthesis: The basics. Annual Review of Plant Physiology and Plant Molecular Biology, 42, 313-349.

Ledwell, J.R., Watson, A.J., Law, C.S., 1993. Evidence for slow mixing across the pycnocline from an open-ocean tracer-release experiment, Nature, 364, 701-703.

Ledwell, J.R., Watson, A.J., Law, C.S., 1998. Mixing of a Tracer in the Pycnocline, Journal of Geophysical Research, 103(C10), 21499-21530.

Lima, I.D., Olson, D.B., Doney, S.C., 2002. Intrinsic dynamics and stability properties of size-structured pelagic ecosystem models. Journal of Plankton Research 24 (6), 533–556.

Lorenzen, C.J., 1966. A method for the continuous measurement of in vivo chlorophyll concentration. Deep-Sea Research 13, 223–227.

MacIntyre, H.L., Kana, T.M., Anning, T., Geider, R.J., 2002. Photoacclimation of photosynthesis irradiance response curves and photosynthetic pigments in microalgae and cyanobacteria. Journal of Phycology 38, 17-38.

Mann, K.H., Lazier, J.R. *N*., 1996. Dynamics of Marine Ecosystems. Blackwell Science, Oxford.

Martin, A.P., 2003. Phytoplankton patchiness: the role of lateral stirring and mixing. Progress in Oceanography 57, 125-174.

Olson, R.J., 1981. Differential photoinhibition of marine nitrifying bacteria: a possible mechanism for the formation of the primary nitrite maximum. Journal of Marine Research 39 (2), 227–238.

Pak, H., Kiefer, D.A., Kitchen, J.C., 1988. Meridional variations in the concentration of chlorophyll and microparticles in the North Pacific Ocean. Deep-Sea Research 35, 7, 1151-1171.

Pierrehumbert, R. T., 1994. Tracer Microstructure in the Large-eddy Dominated Regime. Chaos, Solitons & Fractals 4, 6, 1091-1110.

Redfield, A.C., Ketchum, B.H., Richards, F.A., 1982. The influence of organisms on the composition of seawater. In: Hill, M. *N*. (Ed.), The Sea, Vol. 2. Wiley, New York, pp. 26–77.

Riley, G.A., Stommel, H., Bumpus, D.F., 1949. Quantitative ecology of the plankton of the western North Atlantic. Bulletin of the Bingham Oceanographic Collection 12 (3), 1–169.

Roemmich, D., McGowan, J., 1995. Climatic Warming and the Decline of Zooplankton in the California Current. Science 267, 5202, 1324-1326.

Rudnick, D.L., Ferrari, R., 1999. Compensation of Horizontal Temperature and Salinity Gradients in the Ocean Mixed Layer. Science, 283, 526-529.

Rudnick, D.L., Luyten, J.R., 1996. Intensive surveys of the Azores Front 1. Tracers and dynamics. Journal of Geophysical Research, 101, C1, 923-939.

Sherman, J., Davis, R.E., Owens, W.B., Valdes, J., 2001. The autonomous underwater glider "Spray". IEEE Journal of Oceanic Engineering, 26, 4, 437-446.

Shulenberger, E., Reid, J.L., 1981. The Pacific shallow oxygen maximum, deep chlorophyll maximum, and primary productivity, reconsidered. Deep-Sea Research, 28A, 9, 901-919.

Smethie Jr., W.M., Fine, R.A., 2001. Rates of North Atlantic Deep Water formation calculated from chlorofluorocarbon inventories. Deep-Sea Research I, 48, 189-215.

Steele, J.H., 1974. The Structure of Marine Ecosystems. Harvard University Press, Cambridge.

Steele, J.H., Yentsch, C.S., 1960. The vertical distribution of chlorophyll. Journal of the Marine Biological Association of the United Kingdom 39, 217–226.

Varela, R.A., Cruzado, A., Tintoré, J., Ladona, E.G., 1992. Modelling the deep-chlorophyll maximum: a coupled physical–biological approach. Journal of Marine Research 50, 441–463.

Varela, R.A., Cruzado, A., Tintoré, J., 1994. A simulation analysis of various biological and physical factors influencing the deep-chlorophyll maximum structure in oligotrophic areas. Journal of Marine Systems 5, 143–157.

Venrick, E.L., 1993. Phytoplankton seasonality in the central North Pacific: the endless summer reconsidered. Limnology and Oceanography 38, 1135–1149.

Venrick, E.L., McGowan, J.A., Mantyla, A.W., 1973. Deep maxima of photosynthetic chlorophyll in the Pacific Ocean. Fishery Bulletin (US) 71, 41–52.

Warhaft, Z., 2000. Passive Scalars in Turbulent Flows. Annual Reviews of Fluid Mechanics 32, 203-240.

Winn, C.D., Campbell, L., Christian, J.R., Letelier, R.M., Hebel, D.V., Dore, J.E., Fujieki, L., Karl, D.M., 1995. Seasonal variability in the phytoplankton community of the North Pacific Subtropical Gyre. Global Biogeochemical Cycles 9 (4), 605–620.

Yentsch, C.S., Yentsch, C.M., 1979. Fluorescence spectral signatures: the characterization of phytoplankton populations by the use of excitation and emission spectra. Journal of Marine Research 37, 471–483.

Young, W.R., Roberts, A.J., Stuhne, G., 2001. Reproductive pair correlations and the clustering of organisms. Nature 412, 328-331.